

Development, Verification, and Sensitivity Study of a Lumped Parameter Model for  
Automotive Shock Absorbers

THESIS

Presented in Partial Fulfillment of the Requirements for the Degree Master of Science in  
the Graduate School of The Ohio State University

By

Anthony A. King

Graduate Program in Mechanical Engineering

The Ohio State University

2012

Master's Examination Committee

Professor Marcelo Dapino, Advisor

Professor Dennis Guenther

Copyright by  
Anthony A. King  
2012

## **Abstract**

This research was performed to create a lumped parameter physical model for automotive suspension dampers. The model is valid for twin tube dampers with three chambers, a rebound, a compression, and a reserve chamber, that are connected by a set of valves that include two check valves, one for flow in each direction, and a bleed orifice. The rebound and compression chambers are connected by a moving piston valve and the compression and reserve chambers are connected by a fixed valve. The reserve chamber contains both air and fluid, while the rebound and compression chambers contain only fluid.

The model uses the governing physics that occur in the damper to determine the response of the damper. The main physical relationships are Newton's second law, the orifice flows in the system, conservation of flow between chambers, and fluid compressibility. These relationships include experimentally-determined parameters such as valve characteristics, and measured parameters such as component dimensions.

The model employs physical relationships to predict the force vs. displacement and force vs. velocity response of a damper over a large range of frequencies. The predicted response exhibits the same nonlinear response as the experimental damper tests.

The model was investigated to determine the effect of many parameters within the damper. The investigation of the parameters reveals that the damper response is most dependent on the physical dimensions of the damper rod and piston and the valve characteristics. Through the variation of these parameters, optimal damper responses for various conditions can be determined.

## Acknowledgments

I would like to thank Dr. Marcelo Dapino for being my advisor. He helped me find this topic and perform this study. Thank you for all the advice on classes and research. I would also like to thank Dr. Dennis Guenther for being on my committee.

I would also like to thank Dr. John Yu at Honda R&D Americas, Inc. His guidance and advice on this work helped it reach a successful result for both academia and industry. I would also like to thank Brian Johnson of Honda R&D Americas, Inc. and Brian Schoeny of American Showa Inc. for their assistance with the testing performed for this study.

I would also like to thank Ben Thornton for all his assistance in collaborating on this study. Much of this work would not have been as thorough without your dedication and hard work.

I would also like to thank my parents, Randy and Barb, and my brother, Marcus, for all the encouragement they have given me over the years. Without your help, I would not have become the person I am today.

## Vita

May 2006 .....	Tiffin Calvert High School
2010 .....	B.S. Mechanical Engineering, The Ohio State University
2011 to present .....	Graduate Research Associate, Department of Mechanical Engineering, The Ohio State University

## Fields of Study

Major Field: Mechanical Engineering

# Table of Contents

Abstract . . . . .	ii
Acknowledgements . . . . .	iii
Vita . . . . .	iv
List of Tables . . . . .	vi
List of Figures . . . . .	vii
List of Variables . . . . .	xi
<b>1 Introduction</b>	<b>1</b>
1.1 Motivation . . . . .	1
1.2 Literature Review . . . . .	1
1.2.1 Parametric Models . . . . .	1
1.2.2 Empirical Models . . . . .	3
1.2.3 Component Analysis Methods . . . . .	3
<b>2 Damper Model</b>	<b>5</b>
2.1 Governing Physics . . . . .	5
2.2 Newton's Second Law . . . . .	6
2.3 Flow Continuity . . . . .	8
2.4 Orifice Flows . . . . .	10
2.5 Fluid Compressibility . . . . .	14
<b>3 Experimental Parameter Investigation</b>	<b>17</b>
3.1 Gas Bulk Modulus . . . . .	17
3.2 Oil Bulk Modulus . . . . .	20
3.3 Shim Stiffness . . . . .	22
3.3.1 Initial Shim Stiffness Work . . . . .	23
3.3.2 Shim Stack Stiffness Work . . . . .	25
3.3.3 Experimental Shim Stiffness Work . . . . .	29
3.4 Effective Mass . . . . .	31
3.5 Coulomb Friction . . . . .	31
<b>4 Model Implementation</b>	<b>34</b>
4.1 Simulink Equations . . . . .	34
4.2 Dimensionless Ratio Equations . . . . .	37
4.3 Simulink Model Setup . . . . .	42
4.3.1 Damper Rod Equation . . . . .	42
4.3.2 Damper Body Equation . . . . .	42
4.3.3 Bulk Modulus Equations . . . . .	44
4.3.4 Rebound Chamber Equations . . . . .	44
4.3.5 Compression Chamber Equations . . . . .	46
4.3.6 Reserve Chamber Equations . . . . .	49

<b>5</b>	<b>Model Validation</b>	<b>51</b>
5.1	Damper Experiments . . . . .	51
5.2	Model and Experimental Results . . . . .	54
<b>6</b>	<b>Damper Model Sensitivity Study</b>	<b>59</b>
6.1	Parameter Refinement . . . . .	59
6.2	Sensitivity Study Results . . . . .	61
6.3	Sensitivity Low Speed Extension Results . . . . .	64
6.3.1	Piston Area Sensitivity . . . . .	64
6.3.2	Damper Rod Area Sensitivity . . . . .	65
6.3.3	Piston Bleed Orifice Area Sensitivity . . . . .	66
6.3.4	Fluid Density Sensitivity . . . . .	68
6.3.5	Shim Stiffness for Flow q22 Sensitivity . . . . .	68
6.3.6	Friction Force Amplitude Sensitivity . . . . .	70
6.3.7	Bleed Orifice Discharge Coefficient Sensitivity . . . . .	71
6.3.8	Other Important Parameters . . . . .	72
6.4	Sensitivity High Speed Extension Results . . . . .	75
6.4.1	Repeated Parameters With Significant Effects . . . . .	75
6.4.2	Other Parameters . . . . .	75
6.5	Sensitivity Low Speed Compression Results . . . . .	76
6.5.1	Repeated Parameters With Significant Effects . . . . .	77
6.5.2	Fixed Valve Bleed Orifice Area Sensitivity . . . . .	77
6.5.3	Shim Stiffness for Flow q12 Sensitivity . . . . .	78
6.5.4	Other Parameters . . . . .	80
6.6	Sensitivity High Speed Compression Results . . . . .	81
6.6.1	Repeated Parameters With Significant Effects . . . . .	81
6.6.2	Shim Stiffness for Flow q32 Sensitivity . . . . .	81
6.6.3	Other Parameters . . . . .	83
6.7	Sensitivity Study Conclusions . . . . .	83
<b>7</b>	<b>Conclusions</b>	<b>85</b>

# List of Tables

3.1	Gas bulk modulus comparison to theory. . . . .	20
4.1	Dimensionless conversion parameters. . . . .	37
4.2	Dimensionless ratios for model variables. . . . .	38
4.3	Dimensionless equations for the damper rod subsystem. . . . .	39
4.4	Dimensionless equations for the damper body subsystem. . . . .	39
4.5	Dimensionless equations for the bulk modulus subsystem. . . . .	39
4.6	Dimensionless equations for the rebound chamber subsystem. . . . .	40
4.7	Dimensionless equations for the compression chamber subsystem. . . . .	40
4.8	Dimensionless equations for the reserve chamber subsystem. . . . .	41
5.1	RMS error for the model validation. . . . .	55
6.1	Parameters varied for the sensitivity study. . . . .	60
6.2	Top ten parameters for low speed extension sensitivity. . . . .	64
6.3	Top ten parameters for high speed extension sensitivity. . . . .	75
6.4	Top ten parameters for low speed compression sensitivity. . . . .	77
6.5	Top ten parameters for high speed compression sensitivity. . . . .	81



# List of Figures

2.1	Twin tube damper schematic. . . . .	6
2.2	Damper model schematic. . . . .	7
2.3	Damper rod loading schematic. . . . .	8
2.4	Damper body loading schematic. . . . .	9
3.1	Experimental setup for the gas bulk modulus test. . . . .	18
3.2	Gas bulk modulus test results. . . . .	19
3.3	Gas bulk modulus results from test data. . . . .	19
3.4	Oil bulk modulus initial test results. . . . .	21
3.5	Oil bulk modulus test measurements. . . . .	22
3.6	Oil bulk modulus test results. . . . .	22
3.7	Diagram of a single shim subjected to ring load. . . . .	23
3.8	Single shim FEA setup. . . . .	24
3.9	General flat plate FBD from Roark [1]. . . . .	24
3.10	Single shim FBD from Roark [1]. . . . .	24
3.11	Single shim FBD from Roark. . . . .	25
3.12	Initial FEA for the shim stack. . . . .	26
3.13	Shim stack analytical approach as found in [1]. . . . .	26
3.14	Analytical shim stack method with contact forces. . . . .	27
3.15	Results from analytical shim stack method with contact forces. . . . .	27
3.16	Analytical shim stack method with contact pressure. . . . .	28
3.17	Effective contact pressure radius creation. . . . .	28
3.18	Results from analytical shim stack method with contact pressures. . . . .	28
3.19	Results from a shim stiffness experiment. . . . .	29
3.20	Results from each of the three shim stiffness experiment types. . . . .	30
3.21	Low speed test to show coulomb friction. . . . .	32
3.22	Coulomb friction force vs. displacement results. . . . .	33
4.1	Simulink model top level. . . . .	42
4.2	Simulink model damper rod equation. . . . .	43
4.3	Simulink model damper body equation. . . . .	43
4.4	Simulink model bulk modulus equations. . . . .	45
4.5	Simulink model rebound chamber pressure equation. . . . .	45
4.6	Simulink model compression chamber pressure equation. . . . .	45
4.7	Simulink model reserve chamber pressure equation. . . . .	46
4.8	Simulink model rebound chamber equations. . . . .	47
4.9	Simulink model piston bleed valve equation. . . . .	47
4.10	Simulink model equation for the piston check valve for flow $q_{12}$ . . . . .	47
4.11	Simulink model equation for the piston check valve for flow $q_{22}$ . . . . .	48
4.12	Simulink model compression chamber equations. . . . .	48
4.13	Simulink model fixed valve bleed orifice equation. . . . .	49

4.14	Simulink model equation for the fixed valve check valve for flow $q_{32}$ .	49
4.15	Simulink model equation for the fixed valve check valve for flow $q_{42}$ .	49
4.16	Simulink model reserve chamber equations.	50
5.1	Damper dynamometer.	52
5.2	Example force vs. velocity plot.	53
5.3	Example force vs. displacement plot.	53
5.4	Peak force vs. peak velocity plot for the model validation.	54
5.5	Damper response at peak velocity 1.	55
5.6	Damper response at peak velocity 2.	56
5.7	Damper response at peak velocity 3.	56
5.8	Damper response at peak velocity 4.	56
5.9	Damper response at peak velocity 5.	57
5.10	Damper response at peak velocity 6.	57
5.11	Damper response at peak velocity 7.	57
5.12	Damper response at peak velocity 8.	58
5.13	Peak force vs. peak velocity plot for the model validation.	58
6.1	Sensitivity results for low speed extension.	62
6.2	Sensitivity results for high speed extension.	62
6.3	Sensitivity results for low speed compression.	63
6.4	Sensitivity results for high speed compression.	63
6.5	Force vs. velocity results for the model sensitivity to $A_p$ .	65
6.6	Peak force results for the model sensitivity to $A_p$ .	66
6.7	Force vs. velocity results for the model sensitivity to $A_r$ .	66
6.8	Peak force results for the model sensitivity to $A_r$ .	67
6.9	Force vs. velocity results for the model sensitivity to $A_{11}$ .	67
6.10	Peak force results for the model sensitivity to $A_{11}$ .	68
6.11	Force vs. velocity results for the model sensitivity to $\rho$ .	69
6.12	Peak force results for the model sensitivity to $\rho$ .	69
6.13	Force vs. velocity results for the model sensitivity to $K_2$ .	70
6.14	Peak force results for the model sensitivity to $K_2$ .	71
6.15	Force vs. velocity results for the model sensitivity to $F_r$ .	71
6.16	Peak force results for the model sensitivity to $F_r$ .	72
6.17	Force vs. velocity results for the model sensitivity to $C_{d11}$ .	73
6.18	Peak force results for the model sensitivity to $C_{d11}$ .	73
6.19	Peak force results for the model sensitivity to $C_{d12}$ .	74
6.20	Peak force results for the model sensitivity to $\beta_{31}$ .	74
6.21	Peak force results for the model sensitivity to $L_1$ .	74
6.22	Peak force results for the model sensitivity to $K_4$ .	76
6.23	Peak force results for the model sensitivity to $A_{31}$ .	76
6.24	Force vs. velocity results for the model sensitivity to $A_{31}$ .	78
6.25	Peak force results for the model sensitivity to $A_{31}$ .	78

6.26	Force vs. velocity results for the model sensitivity to $K_1$ . . . . .	79
6.27	Peak force results for the model sensitivity to $K_1$ . . . . .	80
6.28	Peak force results for the model sensitivity to $K_3$ . . . . .	80
6.29	Force vs. velocity results for the model sensitivity to $K_3$ . . . . .	82
6.30	Peak force results for the model sensitivity to $K_3$ . . . . .	83

## LIST OF VARIABLES

Variable	Description
$A_{11}$	Flow area of piston bleed orifice
$A_{31}$	Flow area of fixed valve bleed orifice
$A_{f12}$	Flow area for piston compression shims
$A_{f22}$	Flow area for piston rebound shims
$A_{f32}$	Flow area for fixed valve compression shims
$A_{f42}$	Flow area for fixed valve rebound shims
$A_p$	Cross sectional area of the damper piston
$A_r$	Cross sectional area of the damper rod
$\beta_1$	Bulk modulus of oil in the rebound chamber, chamber 1
$\beta_2$	Bulk modulus of oil in the compression chamber, chamber 2
$\beta_{31}$	Bulk modulus of oil in the reserve chamber, chamber 3
$\beta_{32}$	Bulk modulus of gas in the reserve chamber, chamber 3
$C_{d11}$	Discharge coefficient for piston bleed orifice
$C_{d12}$	Discharge coefficient for piston compression shims
$C_{d22}$	Discharge coefficient for piston rebound shims
$C_{d31}$	Discharge coefficient for fixed valve bleed orifice
$C_{d32}$	Discharge coefficient for fixed valve compression shims
$C_{d42}$	Discharge coefficient for fixed valve rebound shims
$dt$	Time step for the model
$D_{v12}$	Diameter of the orifices about the centerline for flow $q_{12}$
$D_{v22}$	Diameter of the orifices about the centerline for flow $q_{22}$
$D_{v32}$	Diameter of the orifices about the centerline for flow $q_{32}$
$D_{v42}$	Diameter of the orifices about the centerline for flow $q_{42}$
$F_1$	Force at the damper rod from the model
$F_2$	Force at the damper body from the model
$F_{12}$	Force on the piston compression shims
$F_{22}$	Force on the piston rebound shims
$F_{32}$	Force on the fixed valve compression shims
$F_{42}$	Force on the fixed valve rebound shims
$F_{ro}$	Damper friction
$K_1$	Shim stiffness for the check valve governing flow $q_{12}$
$K_2$	Shim stiffness for the check valve governing flow $q_{22}$
$K_3$	Shim stiffness for the check valve governing flow $q_{32}$
$K_4$	Shim stiffness for the check valve governing flow $q_{42}$
$m_b$	Effective mass of the damper body
$m_r$	Effective mass of the damper rod and piston

Variable	Description
$n_{11}$	Number of orifices for flow $q_{11}$
$n_{12}$	Number of orifices for flow $q_{12}$
$n_{22}$	Number of orifices for flow $q_{22}$
$n_{31}$	Number of orifices for flow $q_{31}$
$n_{32}$	Number of orifices for flow $q_{32}$
$n_{42}$	Number of orifices for flow $q_{42}$
$P_1$	Pressure in the rebound chamber from the model
$P_2$	Pressure in the compression chamber from the model
$P_3$	Pressure in the reserve chamber from the model
$P_{3o}$	Initial pressure in the reserve chamber
$P_o$	Initial pressure in the damper
$q_{11}$	Flow through the piston bleed orifice
$q_{12}$	Flow through the piston compression valve
$q_{22}$	Flow through the piston rebound valve
$q_{31}$	Flow through the fixed valve bleed orifice
$q_{32}$	Flow through the fixed valve compression valve
$q_{42}$	Flow through the fixed valve rebound valve
$q_{\beta_1}$	Compression of the oil in the rebound chamber
$q_{\beta_2}$	Compression of the oil in the compression chamber
$q_{\beta_{31}}$	Compression of the oil in the reserve chamber
$q_{\beta_{32}}$	Compression of the gas in the reserve chamber
$\rho$	Density of oil
$V_{1o}$	Initial volume of the rebound chamber
$V_{2o}$	Initial volume of the compression chamber
$V_3$	Initial volume of the reserve chamber
$V_{31}$	Modeled volume of oil in the reserve chamber
$V_{32}$	Modeled volume of gas in the reserve chamber
$V_{32o}$	Initial volume of gas in the reserve chamber
$x_1$	Modeled displacement of shims for $K_1$
$x_2$	Modeled displacement of shims for $K_2$
$x_3$	Modeled displacement of shims for $K_3$
$x_4$	Modeled displacement of shims for $K_4$

# Chapter 1: Introduction

## 1.1 Motivation

Automotive suspensions are difficult to model due to complex fluid-structure dynamics and nonlinearities. The main purpose of the suspension is to connect the frame to the tires. The main components are the spring and dampers, which in many vehicles are combined in parallel, along with other components, to form a strut. The spring is used to support static loading, mainly the weight of the automobile. The spring compresses when the tire hits a bump to limit the displacement passed on the vehicle frame. The damper is used to dissipate energy under dynamic inputs.

Unlike springs, which are simple and straightforward to model, dampers are complex components with nonlinearities caused by fluid compressibility and orifice flows. There are two methods for modeling: a physical model that is based on the governing physics in a system and an empirical model that directly fits equations to experimental results. Empirical models rarely use the same fit parameters for a large range of test conditions. The physical model uses the governing physics in the system as a base for the model equations. The physical model is much more likely to be valid for a large range of tests, so this type of model will be used in this research.

A model of an automotive suspension damper will allow for design engineers to predict the response of different damper setups. This allows the response to be estimated before the setup is experimentally tested. Currently the dampers are tested in the cars and then adjusted to achieve desired response. A model with adequate correlation would significantly decrease the testing required to achieve the best setup.

## 1.2 Literature Review

### 1.2.1 Parameteric Models

There have been many studies focused on creating a model for automotive suspension dampers. They used slightly different dampers or physical relations. Lang [2] and Segel and Lang [3] presented one of the earliest and most comprehensive damper characterization studies. Lang presented a model for a twin tube damper listing all relevant flows and including expressions to quantify the flows. Along with the flows, Lang included a combined fluid and cylinder compressibility term, which allowed the model to exhibit the hysteresis response in the force vs. velocity,  $FV$ , curves. The combined compressibility was based on previous work and not experimentally determined. A flow experiment was used to determine the flow rate based on an applied pressure differential. The flow experiment was used to determine the dynamic discharge coefficients and force coefficients. The dynamic discharge coefficients were assumed to be constant at 0.7 since the effects of acceleration number, Reynolds number,  $d/D$  ratio and  $l/d$  ratio were very small. Only low Reynolds number flow does not match this assumption, but this is only a small portion of the response. Also, treating the

discharge coefficient as a function of Reynolds number would have significantly increased the complexity of the analog computer circuit.

Lang only had an analog computer which severely limited the computing power for the model. Lang compared the model to experiments for validation. Analysis of the computed results show [3]: flows due to fluid compressibility and the formation and collapse of vapor are very significant, the delay in pressure increase at the beginning of the compression cycle is due to the vapor phase, and the hysteresis loop in the FV curve is due to the compressibility of the fluid and the presence of a gas or vapor phase during parts of the cycle.

Dyum et al. [4] created an empirical damper model with assumptions about the internal damper physics. The study focused on the effects of the gas in the damper and fluid compressibility. The model used actual damper test data to fit the model, so it has less value as a predictive tool and more value in parameter identification.

Dyum [5] created models for monotube and twin tube damper designs. The model consists of two parts: one based on the compressibility of fluid to determine the chamber pressures and the other based on pressure differences to determine the valve flows. The valve flows include a bleed orifice, a blow-off valve, and a leakage past the piston. Dyum calculated the fit of the model with the root mean square, RMS, difference between the modeled and measured response. Dyum used quasi-static tests to estimate friction, the initial gas pressure, and the initial gas volume. Dyum used a flow bench test to evaluate the flow equations. The quasi-static test and geometric measurements are all that is needed to use the model for a different damper. Dyum estimated the fluid compressibility from damper experiments. The model was able to achieve sufficient correlation for a BMW twin tube damper.

Talbott [6] and Talbott and Starkey [7] created a physical model of a NASCAR type racing damper. The model is valid for monotube dampers and is parametric, not empirical like the models presented in Section 1.2.2. Talbott modeled the check valve shims using analytical equations presented in Roark [1]. They modeled the shim stack with a contact force between the shims, located at the outer diameter of the smaller of the two shims in contact. Talbott modeled the external pressure loading on the shim stack from the edge of the shim to an inner radius optimized to improve model correlation. A parameter investigation was performed, which determined that the bleed orifices control low speed response and the shim stack stiffness controls high speed response. This model did not include fluid compressibility. The results show that the rebound chamber pressure controls the output force. This is due to the floating piston in monotube dampers, which can move due to gas compression to limit the maximum compression chamber pressure.

Rhoades [8] created a damper model for a monotube damper. Finite Element Analysis (FEA) was used to determine the shim stiffness for the piston check valve. A sensitivity study was performed to see the effects of the main parameters for the flow. The bleed orifice settings are the dominant variable to the damper response. The model ignores fluid compressibility, so hysteresis is not quantified. The model gives adequate correlation with the FV and force vs. displacement, FD, plots.

Lee [9] created a model of a monotube damper. The model contains bleed orifice and shim check valve flow. The shim deflection was determined through FEA and the results

were generalized for the geometric shim ratios. This study included cavitation and thermal effects. Lee accounted for cavitation in the model by setting a minimum pressure limit at the vapor pressure of the fluid. The thermal study shows that if the temperature is significantly increased, the damper force will be decreased.

Mollica and Youcef-Toumi [10] created a physical model of a monotube damper. The model includes fluid inertia, laminar orifice flow, air entrained in hydraulic fluid, and cavitation. Results show that hysteresis is due to effective tube and fluid compliance, gas compliance, piston orifice flow resistance, friction in the floating piston, and compliance caused by check valve preloads. Due to the pressurized nitrogen and floating piston, the monotube damper is less sensitive to cavitation than twin tube dampers.

Alonso and Comas [11] created an analytical model of a twin tube damper that includes valve orifice flow, fluid and chamber compressibility, fluid cavitation, and mass conservation. The model uses damper geometry, such as diameters and lengths, and physical properties of the components, such as fluid density and wall elasticity. The model assumes the cavitation occurs instantaneously so it can be ignored.

### 1.2.2 Empirical Models

Liu and Zhang [12] created a model of a full shock absorber setup, which includes a suspension spring, a twin tube damper, and rubber mounts. All components were assumed to have a linear stiffness and damping where required, except for the damper. They modeled the damper with two types of nonlinear damper models: piecewise bilinear and hysteretic. The model with the hysteretic damper properties showed the best correlation to bench tests. This study presented a purely empirical method for creating the model of a twin tube damper.

Surace et al. [13] presented a simple damper model that fits constants to a set of general force equations. They used the set of piecewise force equations for the nonlinear damper response with respect to velocity. A second model was presented with increased complexity by including fluid compressibility and a better model of the pressure and volume changes within the damper. They compared the parameters in the more complex model to real values, but some are still empirical fits. The model achieves close correlation with experiments.

Reybrouck [14] created a parametric model of a monotube damper that contains bleed orifices, blow-off valves, and leakage past the piston. The model combined the force due to each flow to determine the output force. The model was empirical where constants are fit to experimental data.

### 1.2.3 Component Analysis Methods

There are multiple ways to determine components of the system, such as valve flow characteristics and fluid properties. Herr et al. [15] created a Computational Fluid Dynamics (CFD) model for the flow components within the damper. They combined the flow information with a hydraulic damper model created in EASY5 software package.

Shams et al. [16] created a damper model that used both CFD and FEA. CFD was used to determine the flow through the shim check valves at given displacements. They used FEA



to determine the deflection-force relationship of the shims. These results were combined to determine the force applied to the valves at different piston velocities.

Till and Wendel [17] performed a CFD study on an existing flow valve. The valve was not like a damper valve, but their technique could be used on a damper valve. They ran simulations and determined the main losses in the system and minimized the losses by adjusting the valve in the simulation. This could be used on a damper valve to adjust the losses across the valves to optimize damper response.

Yu et al. [18] performed an analysis on pressure dependence of the bulk modulus of a hydraulic fluid. They determined the bulk modulus based on speed of sound measurements at different fluid pressures to look at the variation. This analysis provides the inspiration for the pressure dependent bulk modulus used in Section 3.1.

Lee and Sun [19] performed an analysis on the effective bulk modulus of the fluid in the damper. They created a more sophisticated model of the wall compliance to be included with the fluid compliance.

## Chapter 2: Damper Model

The damper model uses a stock automotive twin tube damper design. Figure 2.1 shows a schematic of the damper's chambers and the fluid contained in them. This damper configuration consists of 3 chambers: rebound (Ch. 1), compression (Ch. 2), and reserve (Ch. 3). The compression chamber is the volume that acts when the damper is put into compression, such as when a car runs over a bump. The rebound chamber is the volume that acts when the damper is put in tension, such as when the shock absorber extends after being compressed from a bump.

The twin tube damper attaches to the suspension with a mounting point at the bottom of the damper body and another mounting point at the top of the damper rod. The damper rod passes through the rebound chamber and is attached to the damper piston. The piston contains orifices for the flows that control the pressures in the damper.

The chambers are connected by a set of flow orifices. There are three flow paths from the rebound chamber to the compression chamber and three more from the compression chamber to the reserve chamber. The flow paths consist of two check valves, one for flow in each direction, and a bleed orifice that is always open. The check valves are controlled by metal shims that deflect when the pressure difference is positive in the direction that the check valve allows flow. The orifices that control the flow between the rebound and compression chamber are built into the piston. The orifices for the flows between the compression and reserve chamber are in a fixed valve body between the two chambers. The fixed valve body cannot move like the piston.

### 2.1 Governing Physics

Figure 2.2 shows a lumped parameter model of Figure 2.1, including the variable names and their directions. The derivation of the equations is the next step in the model after identifying the important physical parameters. The analytical equations that govern the operation of the damper fall into four main types: Newton's second law, conservation of flow, orifice flow, and fluid compressibility.

This study does not include temperature dependence for two main reasons: the damper temperature did not change during the validation tests and the gas volume in the reserve chamber would be able to compress to account for any expansion in the oil due to a temperature increase. If the temperature were included in the model, the effects would be modeled by the fluid properties being temperature dependent. The fluid density and bulk modulus would change with the temperature. The rest of the damper is made of metal, so the temperature effects are negligible.

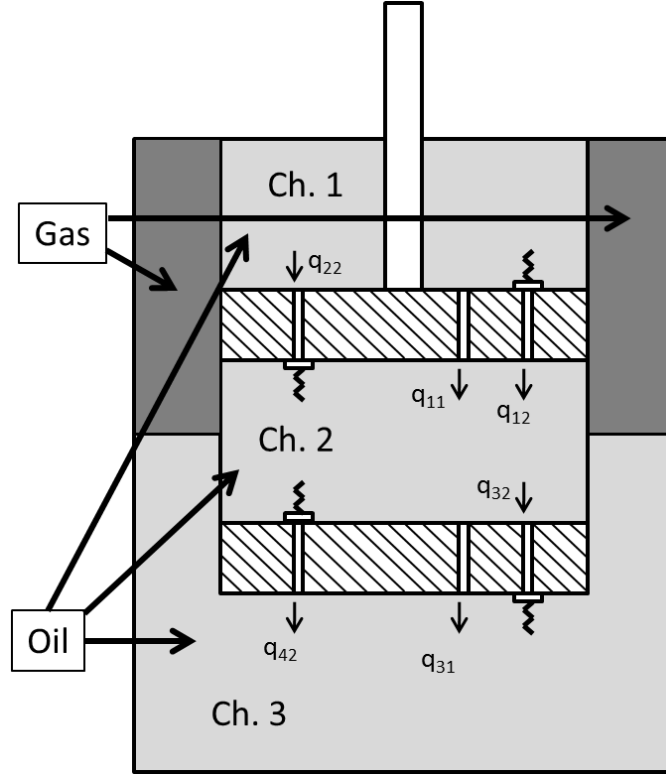


Figure 2.1: Twin tube damper schematic.

## 2.2 Newton's Second Law

The Newton's second law relations focus on the inertia of the components in the system. Newton's second law is given as,

$$\Sigma F = ma = m\ddot{x}, \quad (2.1)$$

where  $m$  is the mass of the body,  $a$  and  $\ddot{x}$  are expressions for the acceleration of the body, and  $\Sigma F$  is the summation of the external forces on the body. This relation holds true as long as all of the external forces on the mass are well defined.

There are two main masses included in the twin tube damper setup: the damper rod and piston and the damper body. These are defined as effective masses in the system due to the fluid contained in the damper. This fluid moves through the piston and the orifice flow creates disturbances in the full fluid volume. The inertial effects of the flows and disturbances cannot be simply taken into account. Therefore, the mass of the fluid is distributed partially with the mass of the damper rod and some with the mass of the damper body.

The forces on the damper are shown in Figure 2.2. The external forces in the system are the force on the damper rod,  $F_1$ , and the force on the damper body,  $F_2$ . The other forces in the system are the forces due to the pressure in the chambers,  $P_1$  and  $P_2$ , and the friction in the system,  $F_r$ .


$$m_r \ddot{x} = F_1 + P_2 A_p - P_1 (A_p - A_r) - F_r \operatorname{sgn}(\dot{z}), \quad (2.2)$$
$$z = x - y, \quad (2.3)$$

$$\dot{z} = \dot{x} - \dot{y}, \quad (2.4)$$

$F_1$  is the external force applied on the damper rod. The force due to  $P_1$  is based on the piston area less the damper rod area. The area for  $P_1$  is the portion of the piston that is directly subjected to  $P_1$ . The force due to the pressure in the compression chamber,  $P_2$ , is based on just  $A_p$ , since the rod does not extend through the compression chamber.

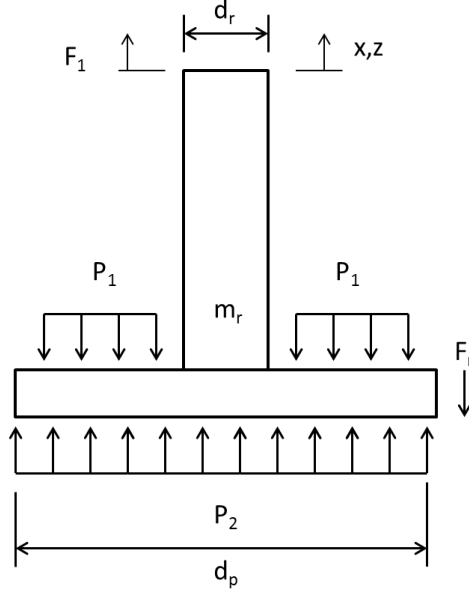


Figure 2.3: Damper rod loading schematic.

The forces on the damper body are shown in Figure 2.4. The summation of forces is given as,

$$m_b \ddot{y} = F_2 - P_2 A_p + P_1 (A_p - A_r) + F_r \text{sgn}(\dot{z}), \quad (2.5)$$

where  $m_b$  is the effective mass of the damper body,  $\ddot{y}$  is the acceleration of the damper body, and  $F_2$  is the external force applied to the damper body from the mounting.

The two Newton's second law equations include the same pressure and friction terms, in equal and opposite directions. The external forces and inertia terms are different since they are two distinct bodies coupled by the friction and pressure terms.

## 2.3 Flow Continuity

Each of the chambers in the damper has flows that go into and out of the chamber, as shown in Figure 2.2. All flows are defined in the same direction for simplicity. Due to the reference direction, some flows will always have be in the negative direction and others can be negative or positive. The signs will be covered in Section 2.4.

The flows for the rebound chamber are shown in Figure 2.2. The flow continuity equation for the rebound chamber, chamber 1, is given as,

$$\dot{z}(A_p - A_r) = q_{11} + q_{12} + q_{22} + q_{\beta_1}, \quad (2.6)$$

where  $\dot{z}$  is the relative velocity between the piston and damper body,  $A_p$  is the piston area,  $A_r$  is the damper rod area,  $q_{11}$  is the bleed orifice flow,  $q_{12}$  is the flow from the compression

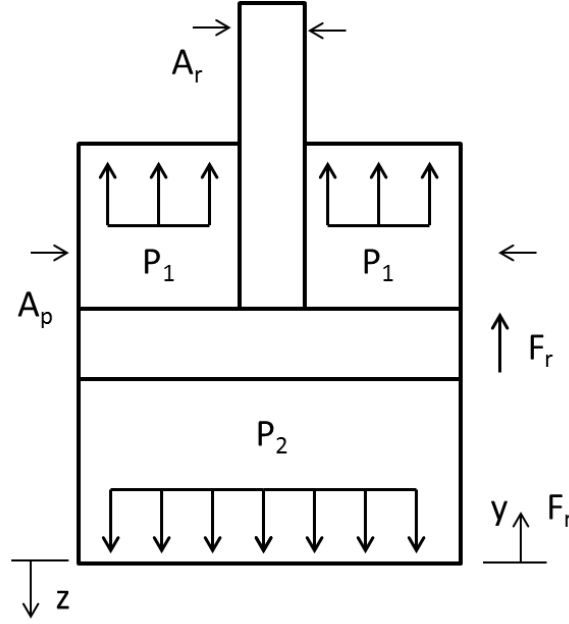


Figure 2.4: Damper body loading schematic.

chamber to the rebound chamber through the check valve that controls the flow in this direction,  $q_{22}$  is the flow from the rebound chamber to the compression chamber through a check valve, and  $q_{\beta_1}$  is the flow due to the compressibility of the fluid in chamber 1. Flows  $q_{11}$ ,  $q_{12}$ , and  $q_{22}$  are explained in Section 2.4;  $q_{\beta_1}$  is covered in Section 2.5.

The flow due to a positive relative piston motion causes a compression or decrease in volume of the fluid in chamber 1. This decrease in volume must be accounted for by the other flows in the system. In the right hand side of the flow continuity equation, a positive flow is one out of chamber 1, while a negative flow is one into chamber 1. As shown in Figure 2.2, the positive direction for the three orifice flows is from chamber 1 to chamber 2. Therefore they are out of chamber 1 and positive in the above equation since they account for the flow into the system due to the piston motion.

The fluid compressibility flow needs to be correctly defined in the flow continuity equation and in the equation for the compressibility. The assumption here is that when the pressure in chamber 1 increases, the volume of the fluid decreases. Therefore it is defined as a flow out of chamber 1 in the flow continuity equation. The expression for the fluid compressibility is derived and defined in Section 2.5.

The flows into and out of the compression chamber are shown in Figure 2.2. The flow continuity equation for the compression chamber, chamber 2, is given as,

$$\dot{z}A_p = q_{11} + q_{12} + q_{22} - q_{31} - q_{32} - q_{42} - q_{\beta_2}, \quad (2.7)$$

where  $q_{31}$  is the bleed orifice flow,  $q_{32}$  is the flow from the compression chamber to the reserve chamber through the check valve that controls the flow in this direction,  $q_{42}$  is the flow from

the reserve chamber to the compression chamber through a check valve, and  $q_{\beta_2}$  is the flow due to the compressibility of the fluid in chamber 2. Flows  $q_{31}$ ,  $q_{32}$ , and  $q_{42}$  are explained in Section 2.4;  $q_{\beta_2}$  is covered in Section 2.5.

The flow due to a positive relative displacement causes expansion or increase in volume of the fluid in chamber 2. This increase in volume is accounted for by the flows in the system. For the right hand side of (2.7), a flow into chamber 2 has a positive sign, while a flow out of chamber 2 has a negative sign. Orifice flows  $q_{11}$ ,  $q_{12}$ , and  $q_{22}$  are positive in (2.7), since the positive direction for these flows is into of chamber 2. Orifice flows  $q_{31}$ ,  $q_{32}$ , and  $q_{42}$  are negative in (2.7), since the positive direction for these flows is out of chamber 2. The flow due to the fluid compressibility in chamber 2,  $q_{\beta_2}$ , is negative in (2.7), since the positive direction of  $q_{\beta_2}$  is a compression of the fluid in chamber 2.

The flows into and out of the reserve chamber are shown in Figure 2.2. The flow continuity equation for the reserve chamber, chamber 3, can be written as,

$$0 = q_{31} + q_{32} + q_{42} - q_{\beta_{31}} - q_{\beta_{32}}, \quad (2.8)$$

where  $q_{\beta_{31}}$  is the compressibility of the oil in chamber 3 and  $q_{\beta_{32}}$  is the compressibility of the gas in chamber 3. These flows are defined in Section 2.5.

Since the fixed valve is rigidly attached to the damper body, there is no change in the total volume of chamber 3 due to motion. This means that the flows into or out of the do not have a direct sign reference, unlike chambers 1 and 2 that can be defined based on the flow from the piston motion. So the flows in (2.8) are defined as positive for flows into chamber 3 and negative for flows out of chamber 3. The orifice flows  $q_{31}$ ,  $q_{32}$ , and  $q_{42}$  are positive since the positive direction for the flows is into chamber 3. The oil compressibility,  $q_{\beta_{31}}$ , and gas compressibility,  $q_{\beta_{32}}$ , are both negative, since a positive compression is equivalent to a flow out of chamber 3.

## 2.4 Orifice Flows

The orifice flows are governed by the equation for the flow through a sharp edged orifice, given as,

$$q = C_d A \sqrt{\left(\frac{2\Delta P}{\rho}\right)}, \quad (2.9)$$

where  $q$  is the flow through the orifice,  $C_d$  is the discharge coefficient of the orifice,  $A$  is the flow area of the orifice,  $\Delta P$  is the pressure differential across the orifice, and  $\rho$  is the density of the fluid flowing through the orifice. This equation is used to define the different orifice flows in the damper. The main differences between the orifices that are captured in the equation are the flow area and direction of flow. There are 2 types of orifices in the damper: bleed orifices and check valve orifices. The main difference between the 2 types of orifices is that the bleed valve allows flow in both directions and the check valve only allows flow in one direction through the orifice.

There is a bleed orifice in the piston and the fixed valve. The bleed valve orifice is always open, but has a significantly smaller area than the check valve orifice. Since the bleed valve is always fully open, it governs the low pressure difference flows. Each bleed orifice in the damper consists of a set of orifices, so the number of orifices is needed in the equation.

The flow through the bleed orifice in the piston,  $q_{11}$ , is written in the form,

$$q_{11} = C_{d11} A_{11} n_{11} \text{sgn}(P_1 - P_2) \sqrt{\frac{2|P_1 - P_2|}{\rho}}, \quad (2.10)$$

where  $C_{d11}$  is the discharge coefficient for the flow through the piston bleed orifice,  $A_{11}$  is the flow area for a single orifice in the piston bleed orifice,  $n_{11}$  is the number of individual orifices for flow  $q_{11}$ , and  $P_1$  and  $P_2$  are the pressures in the rebound and compression chambers respectively.

The bleed orifice flow can occur in both directions depending on the pressure difference. The pressure difference,  $\Delta P$ , in (2.9) cannot change the direction of the flow due to the square root, which actually prevents the equation from being solved for a negative  $\Delta P$ . The absolute value and sign function are used to obtain the correct results for flow in either direction. The sign function allows the flow to be positive if  $P_1 > P_2$  and negative if  $P_1 < P_2$ . The absolute value allows for the square root to yield a real number for both  $P_1 > P_2$  and  $P_1 < P_2$ .

The bleed orifice flow in the fixed valve,  $q_{31}$ , can be described in the same way as  $q_{11}$ . The expression for  $q_{31}$  is,

$$q_{31} = C_{d31} A_{31} n_{31} \text{sgn}(P_2 - P_3) \sqrt{\frac{2|P_2 - P_3|}{\rho}}, \quad (2.11)$$

where  $C_{d31}$  is the discharge coefficient for the flow through the fixed valve bleed orifice,  $A_{31}$  is the flow area for a single orifice in the fixed valve bleed orifice,  $n_{31}$  is the number of individual orifices for flow  $q_{31}$ , and  $P_2$  and  $P_3$  are the pressures in the compression and reserve chambers respectively.

The flows through the check valves are more complex due to the variable area controlled by the shim deflection. The check valve does not need the sign function like the bleed orifice, since it only allows flow in one direction. Therefore the expression is either positive or negative based on the direction of flow relative to the direction defined in the free body diagram. The absolute value is still needed to give a real number as the result of the square root. In lieu of the sign function, the check valve flows need to be defined as piecewise function with the flow equal to 0 for one pressure differential and equal to an expression similar to (2.9) for the oppositely signed pressure differential.

The flow through the piston check valve that allows flow from chamber 2 to chamber 1 is defined as,

$$q_{12} = 0 \quad P_1 \geq P_2 \quad (2.12)$$

$$q_{12} = -C_{d12} A_{12} \sqrt{\frac{2|P_1 - P_2|}{\rho}} \quad P_1 < P_2, \quad (2.13)$$



where  $C_{d12}$  is the discharge coefficient of the flow through the check valve for the flow from the compression chamber to the rebound chamber, and  $A_{12}$  is the flow area for the check valve.

The flow area for the check valve varies with respect to the displacement of the shim stack,  $x_1$ , as shown in the expression for  $A_{12}$ . The flow area for flow  $q_{12}$  is written in the form,

$$A_{12} = \pi D_{v12} x_1, \quad (2.14)$$

where  $D_{v12}$  is the diameter of the orifices about the damper centerline and  $x_1$  is the displacement of the shim stack. This relation is the surface area of the curved surface of a cylinder with a circumference of  $\pi D_{v12}$  and a height of  $x_1$ .

The displacement of the shim stack varies with respect to the pressure difference, as shown in the expression for  $x_1$ . The displacement of the shim stack due to a pressure differential is defined by,

$$x_1 = \frac{F_{12}}{K_1} = \frac{|P_1 - P_2| A_{f12} n_{12}}{K_1}, \quad (2.15)$$

where  $F_{12}$  is the force applied to the shims due to the pressure difference,  $K_1$  is the stiffness of the shims in the check valve that controls flow  $q_{12}$  measured at a radius of  $D_{v12}/2$ ,  $A_{f12}$  is the area of a single orifice for flow  $q_{12}$ , and  $n_{12}$  is the number of individual orifices for flow  $q_{12}$ . The method for determining the stiffness,  $K_1$ , is described in Section 3.3.

Combining (2.12)-(2.15) gives the full expression for  $q_{12}$ ,

$$q_{12} = 0 \quad P_1 \geq P_2 \quad (2.16)$$

$$q_{12} = -C_{d12} \pi D_{v12} \frac{|P_1 - P_2| A_{f12} n_{12}}{K_1} \sqrt{\frac{2 |P_1 - P_2|}{\rho}} \quad P_1 < P_2. \quad (2.17)$$

This expression includes a negative sign in the front since the flow through this check valve can only occur in the negative direction as defined in Figure 2.2. As previously mentioned, the piecewise function is used to set the flow for this check valve equal to 0 when  $P_1 \geq P_2$ , since the check valve is fully closed. For  $P_1 < P_2$  the flow  $q_{12}$  occurs as defined in the orifice flow expression.

The other check valve flows are derived and defined the same way that  $q_{12}$  was defined in (2.12)-(2.16). Equation (2.16) simply needs to be converted with the correct dimensions, stiffnesses, and signs for each of the other 3 check valve flows.

The check valve flow from the rebound chamber to the compression chamber,  $q_{22}$ , is given by the expression,

$$q_{22} = 0 \quad P_1 \leq P_2 \quad (2.18)$$

$$q_{22} = C_{d22} \pi D_{v22} \frac{|P_1 - P_2| A_{f22} n_{22}}{K_2} \sqrt{\frac{2 |P_1 - P_2|}{\rho}} \quad P_1 > P_2, \quad (2.19)$$

where  $C_{d22}$  is the discharge coefficient for flow  $q_{22}$ ,  $D_{v22}$  is the diameter of the orifices for flow  $q_{22}$  about the centerline of the damper,  $A_{f22}$  is the flow area of a single orifice for flow

$q_{22}$ ,  $n_{22}$  is the number of individual orifices for flow  $q_{22}$ , and  $K_2$  is the shim stiffness of the shim stack for flow  $q_{22}$  measured at a radius of  $D_{v22}/2$ .

The flow from the compression chamber to the rebound chamber is set to 0 by the piecewise function when  $P_1 \leq P_2$ . The flow should be 0, since this pressure difference would create a flow from the compression to the rebound chamber and this flow direction is blocked for the  $q_{22}$  orifice. The flow exists when  $P_1 > P_2$  since this pressure differential creates a flow from the rebound chamber to the compression chamber to balance the pressure. This flow is positive due to the actual direction of flow being in the positive direction defined for  $q_{22}$  in Figure 2.2.

The fixed valve check valve flows follow the same expression as the piston check valve flows. The expression for the flow from the compression chamber to the reserve chamber,  $q_{32}$ , is written in the form,

$$q_{32} = 0 \quad P_2 \leq P_3 \quad (2.20)$$

$$q_{32} = C_{d32} \pi D_{v32} \frac{|P_2 - P_3| A_{f32} n_{32}}{K_3} \sqrt{\frac{2 |P_2 - P_3|}{\rho}} \quad P_2 > P_3, \quad (2.21)$$

where  $C_{d32}$  is the discharge coefficient for flow  $q_{32}$ ,  $D_{v32}$  is the diameter of the orifices for flow  $q_{32}$  about the centerline of the damper,  $A_{f32}$  is the flow area of a single orifice for flow  $q_{32}$ ,  $n_{32}$  is the number of individual orifices for flow  $q_{32}$ , and  $K_3$  is the shim stiffness of the shim stack for flow  $q_{32}$  measured at a radius of  $D_{v32}/2$ .

The flow from the reserve chamber to the compression chamber is set to 0 by the piecewise function when  $P_2 \leq P_3$ . This pressure difference would create a flow from the reserve chamber to the compression chamber with an open orifice, but this check valve is blocked in this direction forcing the flow to 0. The flow exists when  $P_2 > P_3$ , since this pressure differential creates a flow from the compression chamber to the reserve chamber to balance the pressure. This flow is positive due to the actual direction of flow caused by  $P_2 > P_3$  being in the positive direction defined for  $q_{32}$  in Figure 2.2.

The expression for the flow from the reserve chamber to the compression chamber,  $q_{42}$ , is defined as,

$$q_{42} = 0 \quad P_2 \geq P_3 \quad (2.22)$$

$$q_{42} = -C_{d42} \pi D_{v42} \frac{|P_2 - P_3| A_{f42} n_{42}}{K_4} \sqrt{\frac{2 |P_2 - P_3|}{\rho}} \quad P_2 < P_3, \quad (2.23)$$

where  $C_{d42}$  is the discharge coefficient for flow  $q_{42}$ ,  $D_{v42}$  is the diameter of the orifices for flow  $q_{42}$  about the centerline of the damper,  $A_{f42}$  is the flow area of a single orifice for flow  $q_{42}$ ,  $n_{42}$  is the number of individual orifices for flow  $q_{42}$ , and  $K_4$  is the shim stiffness of the shim stack for flow  $q_{42}$  measured at a radius of  $D_{v42}/2$ .

The flow from the compression chamber to the reserve chamber is set to 0 by the piecewise function when  $P_2 \geq P_3$ . This pressure difference would create a flow from the compression chamber to the reserve chamber with an open orifice, but the check valve is blocked in this

direction forcing the flow to 0. The flow exists when  $P_2 < P_3$  since this pressure differential creates a flow from the reserve chamber to the compression chamber to balance the pressure. This flow is negative due to the actual direction of flow caused by  $P_2 < P_3$  being in the negative direction defined for  $q_{42}$  in Figure 2.2.

## 2.5 Fluid Compressibility

The fluid compressibility in the damper is modeled by the bulk modulus equation, which is shown to be,

$$\beta = -V_o \frac{\Delta P}{\Delta V}, \quad (2.24)$$

where  $\beta$  is the bulk modulus of the fluid,  $\Delta P$  is the change in pressure in a fluid container,  $\Delta V$  is the change in volume of a fluid container, and  $V_o$  is the initial volume of the container at the initial pressure. Both  $\Delta P$  and  $\Delta V$  are taken from the same equilibrium point, which defines the initial pressure and initial volume.

This equation needs to be converted for use with flows, instead of discrete changes in volume. Taking the derivative of (2.24) results in,

$$\frac{d}{dt} (\beta) = \frac{d}{dt} \left( -V_o \frac{\Delta P}{\Delta V} \right) \quad (2.25)$$

$$\beta = -V_o \frac{\Delta P}{dt} \frac{1}{\frac{\Delta V}{dt}} = -\frac{V_o \dot{P}}{q_\beta} \quad (2.26)$$

$$q_\beta = \frac{V_o \dot{P}}{\beta}, \quad (2.27)$$

where  $q_\beta$  is the flow due to fluid compressibility, and  $\dot{P}$  is the time rate of change of the pressure in the container. The negative sign is dropped in the last form of the equation due to the sign convention used in Section 2.3. This sign convention made a flow out of the system positive, which occurs when there is a positive increase in pressure.

Equation (2.27) is the expression used to define the compressibility of the fluid, either gas or oil, in each chamber of the damper. There are four equations directly based on this expression: the equations for  $q_{\beta_1}$ ,  $q_{\beta_2}$ ,  $q_{\beta_{31}}$ , and  $q_{\beta_{32}}$ .

The compressibility of the oil in the rebound chamber,  $q_{\beta_1}$ , is given as,

$$q_{\beta_1} = \frac{V_1 \dot{P}_1}{\beta_1}, \quad (2.28)$$

where  $\beta_1$  is the bulk modulus of the fluid in the rebound chamber,  $\dot{P}_1$  is the time rate of change of the pressure in the rebound chamber, and  $V_1$  is the volume of the fluid in the rebound chamber, which is defined by,

$$V_1 = (L_1 - z)(A_p - A_r), \quad (2.29)$$

where  $L_1$  is the initial length of the rebound chamber.

The compressibility of the oil in the compression chamber,  $q_{\beta_2}$ , is given as,

$$q_{\beta_2} = \frac{V_2 \dot{P}_2}{\beta_2}, \quad (2.30)$$

where  $\beta_2$  is the bulk modulus of the fluid in the compression chamber,  $\dot{P}_2$  is the time rate of change of the pressure in the compression chamber, and  $V_2$  is the volume of the fluid in the compression chamber, which is given as,

$$V_2 = (L_2 + z)A_p, \quad (2.31)$$

where  $L_2$  is the initial length of the compression chamber.

The compressibility of the oil in the reserve chamber,  $q_{\beta_{31}}$ , is given as,

$$q_{\beta_{31}} = \frac{V_{31} \dot{P}_3}{\beta_{31}}, \quad (2.32)$$

where  $\beta_{31}$  is the bulk modulus of the fluid in the reserve chamber,  $V_{31}$  is the volume of the fluid in the reserve chamber, and  $\dot{P}_3$  is the time rate of change of the pressure in the reserve chamber.

The compressibility of the gas in the reserve chamber,  $q_{\beta_{32}}$ , is given as,

$$q_{\beta_{32}} = \frac{V_{32} \dot{P}_3}{\beta_{32}}, \quad (2.33)$$

where  $\beta_{32}$  is the bulk modulus of the gas in the reserve chamber,  $V_{32}$  is the volume of the fluid in the reserve chamber, and  $\dot{P}_3$  is the time rate of change of the pressure in the reserve chamber.

The reserve chamber contains both oil and gas, with no physical component separating the two fluids. The only thing keeping the fluids separated is gravity pulling down on the heavier oil. Two expressions are derived to govern the instantaneous volume of oil and gas in the reserve chamber. The first is based on conservation of volume which is,

$$V_3 = V_{31} + V_{32}, \quad (2.34)$$

where  $V_3$  is the total volume of the reserve chamber.

The other expression is based on the expression for the bulk modulus of a fluid, given in (2.24). Plugging the expressions for the pressure and volume change of gas in the reserve chamber into (2.24) results in,

$$\beta_{32} = \frac{-(P_3 - P_{3o}) * V_{32o}}{V_{32} - V_{32o}}, \quad (2.35)$$

$$V_{32} - V_{32o} = \frac{-(P_3 - P_{3o}) * V_{32o}}{\beta_{32}}, \quad (2.36)$$

$$V_{32} = V_{32o} \left( 1 - \frac{(P_3 - P_{3o})}{\beta_{32}} \right). \quad (2.37)$$

Equations (2.34) and (2.37) complete the main equations of the damper model. The equations derived above give a set of 18 equations with 18 unknowns that can be solved to determine the damper response.

# Chapter 3: Experimental Parameter Investigation

The equations in Chapter 2 left some parameters to be defined later. The main parameters are the gas bulk modulus, oil bulk modulus, shim stiffnesses, effective mass of the damper body, and coulomb friction. These parameters were experimentally determined.

## 3.1 Gas Bulk Modulus

The gas bulk modulus is used to determine the compressibility of gas in the reserve chamber of the damper. Equation (2.24) shows the equation for the bulk modulus of a fluid. To determine the bulk modulus of a fluid, two sets of data points are needed: change in pressure of the fluid in a sealed container and change in volume of the container. An experiment to obtain this data needs to have a well-controlled method for varying the volume, while being able to measure the pressure. Another options is for the experiment to control and vary the pressure, while measuring the volume. The former option is the simplest, since it is easier to measure a change in pressure than a change in volume.

A simple pressure transducer can be used to measure the change in pressure in the volume. The only limitation to this setup is that the container needs to have a pressure port built-in or can have a pressure port added for use of the pressure transducer. A pneumatic cylinder with an inlet or outlet port can be used, as long as the cylinder also has a rod that can be used to compress the fluid in the cylinder. In this experiment, the rod was moved by an external source to create the change in volume. The only way for the container to account for this change in volume is for the fluid to compress or expand. The main focus of this study is on the compressibility, so the volume was decreased, causing a pressure increase.

Since this study is focused on dampers, the bulk modulus experiment is performed on a damper dynamometer. The damper dynamometer is traditionally used for dynamic tests, but also for step functions. The setup and sensors of the damper dynamometer are described in Section 5.1. The actuator on the dynamometer can move a set distance and hold that displacement. The experimental test setup for calculating the gas bulk modulus used a pneumatic cylinder. The cylinder had a pressure port and a charge port for filling and charging the system to an initial pressure. The cylinder was mounted in the dynamometer with the threaded connections in the actuator and load cell of the dynamometer, which is the same way a damper is mounted. The other change to the cylinder was that the piston is no longer blocked, like a traditional pneumatic cylinder piston. The unblocked piston allows flow between the two chambers, thus increasing the working volume to the whole cylinder, instead of just the volume on one side of the piston. The change in volume was due to the insertion of the rod since the piston is not blocked. This makes the change in volume dependent on the rod area instead of the piston area.

Increasing the working volume and decreasing the volume change allows for finer pressure steps. A schematic of the initial pneumatic cylinder and the setup for the gas bulk modulus test is shown in Figure 3.1. The setup clearly shows the difference between the rod and

piston areas and the working volumes for the two cases. The finer pressure steps allow for more data points to be used to calculate bulk modulus.

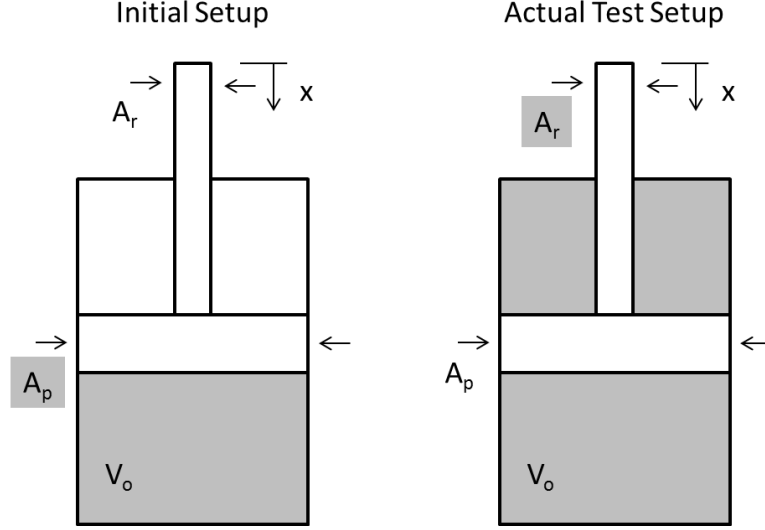


Figure 3.1: Experimental setup for the gas bulk modulus test.

The results from the test are shown in Figure 3.2, which shows that the pressure change is linearly dependent on the change in volume. Using (2.24), the data shown in Figure 3.2 was used to calculate the bulk modulus of the gas. The resulting bulk modulus for each displacement and the mean value are shown in Figure 3.3. The result for each step is less than 2% from the mean value. Therefore a constant gas bulk modulus can be used in the model.

The results here were compared to theoretical values of the bulk modulus of a gas. Doebelin [20] contains two cases for the theoretical bulk modulus: an isothermal case for slow pressure changes and an adiabatic case for rapid pressure changes. The isothermal case is given as,

$$\beta_{gi} = P_o, \quad (3.1)$$

where  $\beta_{gi}$  is the isothermal bulk modulus of a gas and  $P_o$  is the operating pressure of the gas. The adiabatic case yields a similar result, which can be written as,

$$\beta_{ga} = 1.4 * P_o, \quad (3.2)$$

where  $\beta_{ga}$  is the adiabatic bulk modulus of a gas and  $P_o$  is the operating pressure of the gas.

The results of the three cases are shown in Table 3.1. The percent error in Table 3.1 is defined as,

$$Difference(\%) = \frac{|\beta_{th} - \beta_{ex}|}{\beta_{th}} * 100\% \quad (3.3)$$

where  $\beta_{th}$  is the theoretical value of the bulk modulus and  $\beta_{ex}$  is the experimental result for the gas bulk modulus. This table shows that the isothermal case matches very closely to the

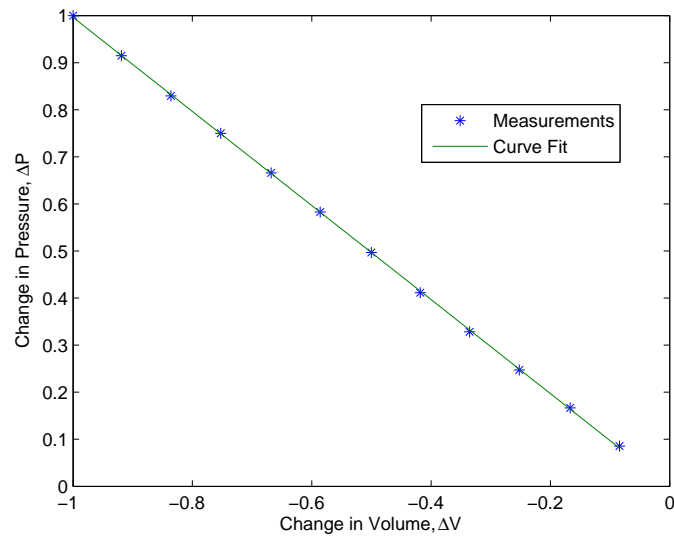


Figure 3.2: Gas bulk modulus test results.

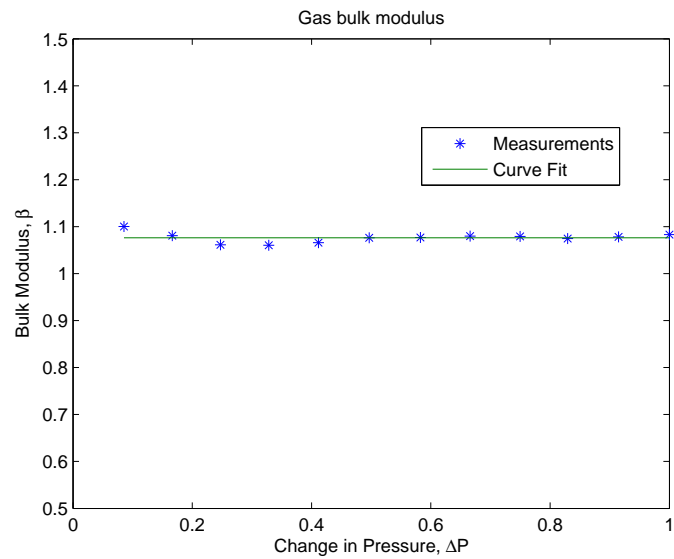


Figure 3.3: Gas bulk modulus results from test data.

experimental results. This is due to the slow rate at which the pressure was changed in the experiment to prevent dynamic effects. The correlation with the theoretical results shows that the experiment was effective and the result can be used in the model.



Table 3.1: Gas bulk modulus comparison to theory.

Method	Expression	Percent Difference (%)
Experimental	$1.08 * P_o$	N/A
Theoretical Isothermal	$1 * P_o$	7.1
Theoretical Adiabatic	$1.4 * P_o$	30

## 3.2 Oil Bulk Modulus

The oil bulk modulus is used to determine the compressibility of the oil in the damper. Section 3.1 outlined the method for experimentally determining the bulk modulus of the gas in the damper. This same method was applied to the fluid in the damper, which is a hydraulic oil. The main difference between the oil and gas test is that the oil is significantly more dense and would reach much larger pressures than the gas when compressed. There are 2 options to avoid issues: use the same test as the gas with a more robust container or to use a test with lower displacements and the same container. The actual fluid bulk modulus test was performed with the same container as the gas bulk modulus test with lower displacements. The lower displacements prevented the pressure from rising above the maximum pressure of the seals on the container.

The test consisted of a ramp to a displacement and then the displacement was held for enough time for the pressure to reach equilibrium after the ramp. The results in Figure 3.4 show that the system was losing pressure and not reaching equilibrium when the displacement was held constant. The most obvious reason for this to occur is a leak in the container. This was ruled out since no oil was visible on the outside of the container. Another option is that the gas was not fully bled from the container before the test, which would create mixing between the fluid and gas. Since the fluid and gas were compressed, the gas was more likely to emulsify into the fluid. As the gas emulsified with the fluid, the combined bulk modulus decreased since it is an even mixture, thus causing the pressure to decrease.

Emulsification occurs in a typical damper during operation. Since the damper contains a mixture of oil and gas, some of the gas will emulsify in the fluid. Therefore the working fluid of the damper is actually the emulsified oil and not pure oil, meaning the bulk modulus of the emulsified oil is more useful in the model than the pure fluid. So two main issues needed to be worked around for the final testing: change in pressure over time with a constant displacement and use of emulsified oil instead of pure oil. The pure oil was emulsified in a damper and then added to the bulk modulus test container. The issue with this is that the oil and gas will separate over time. Therefore the test needed to be run soon after the oil is emulsified. Since the oil emulsification and the filling of the bulk modulus container take a significant amount of time, the test was changed to a quasi-static test instead of the discrete steps that are shown in Figure 3.4. The quasi-static test involved a slow ramp to the

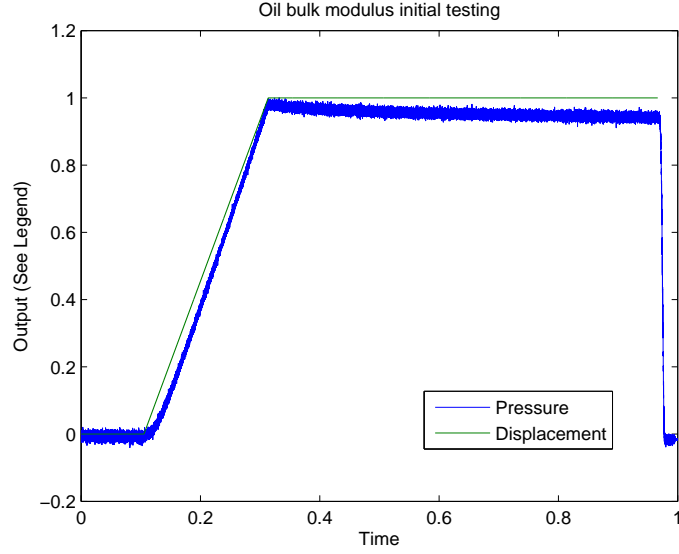


Figure 3.4: Oil bulk modulus initial test results.

maximum displacement and back down to 0 displacement. The resulting data was sampled to create as many discrete steps as needed, allowing for finer resolution than using a step function for each discrete point and running a new test each time.

The final quasi-static test results are shown in Figure 3.5, with the pressure and displacement shown on the same plot. The results were sampled to determine the bulk modulus of the fluid. The bulk modulus was calculated from one point to the next, so the change in volume was the same for each calculation and the initial volume changed. Figure 3.6 shows the resulting bulk modulus at each initial pressure and the curve fits applied to obtain the final value of the fluid bulk modulus. The final fluid bulk modulus was linearly dependent on the pressure based on the "Mean Trend" line shown in Figure 3.6. The resulting bulk modulus was written as,

$$\beta_o(P) = \beta_{om} * P + \beta_{ob}, \quad (3.4)$$

where  $\beta_o$  is the pressure dependent bulk modulus,  $\beta_{om}$  is the slope of the pressure dependent bulk modulus,  $\beta_{ob}$  is the intercept of the pressure dependent bulk modulus, and  $P$  is the pressure in the fluid.

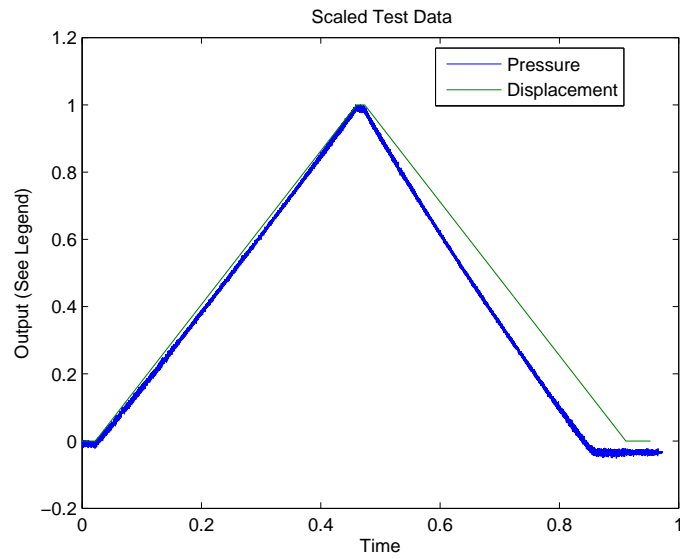


Figure 3.5: Oil bulk modulus test measurements.

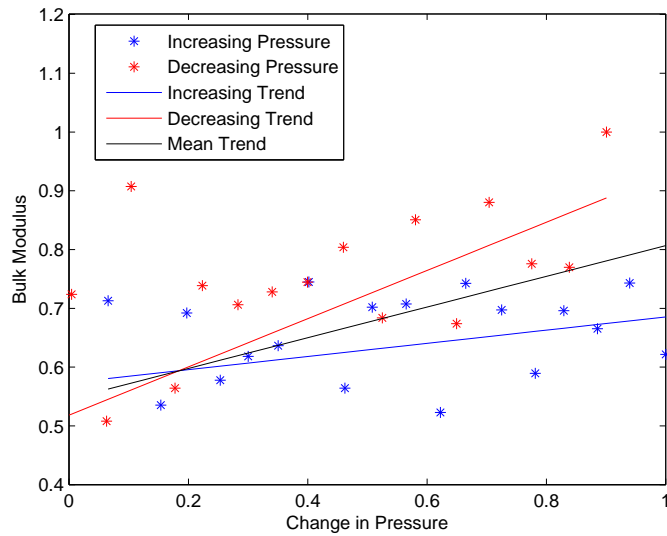


Figure 3.6: Oil bulk modulus test results.

### 3.3 Shim Stiffness

The piston and fixed valve each contain two check valves that control the flows between the chambers. The check valve flows are regulated by stacks of shims, which seal orifices in one direction and allow flow through in the other. Each valve has two check valves to allow flow

in each direction. The shims are thin pieces of metal that deflect when a pressure differential is created across the valve. There are two ways to model the response of the valves. The best would be to create a direct flow relation, where the flow is known for a given pressure differential. A more practical option is to determine a force vs. displacement relation, or stiffness, that controls the deflection of the shims, which can be used to determine the orifice area for the valve. The method used in this study is to determine a stiffness for the shims. There are three main methods for determining the stiffness of the shims: Finite Element Analysis (FEA), analytical equations, and experimental tests.

### 3.3.1 Initial Shim Stiffness Work

The three methods above were investigated to determine the shim stiffness. The FEA or analytical cases are the best options because they can be calculated without experiments on actual parts. Only dimensions would be needed for either of these setups to determine the resulting stiffness. The actual valves had complex loading areas, so a simplified case was used to compare the three methods. The FEA and analytical models became axisymmetric, since the load was the same for the whole revolution of the part. The axisymmetric setup became a simple cantilevered beam. Figure 3.7 shows the free body diagram of the ring load from the axisymmetric side view.

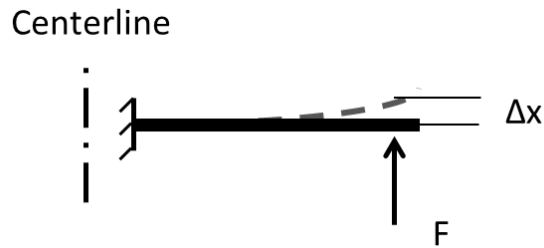


Figure 3.7: Diagram of a single shim subjected to ring load.

The FEA analysis was performed in COMSOL. The model was fixed at the inner diameter and loaded at the same diameter as the experimental parts. Figure 3.8 shows the FEA setup for the ring load case. The load was specified and the displacement was calculated by COMSOL, then the results were used to calculate a shim stiffness. The analytical case used equations from Roark's Formulas for Stress and Strain [1]. Roark contains equations for many specific loading conditions and chapter 11 of Roark contains setups specifically for flat plates. The general free body diagram from Roark for a circular plate subjected to a line load or ring load is shown in Figure 3.9. Case 11 on page 463 was used for this analysis and the free body diagram for this setup is shown in Figure 3.10. The equations are based on a general form, with a set of constants based on the loading location, inner diameter, and outer diameter of the plate. The resulting stiffness matched the FEA very well.

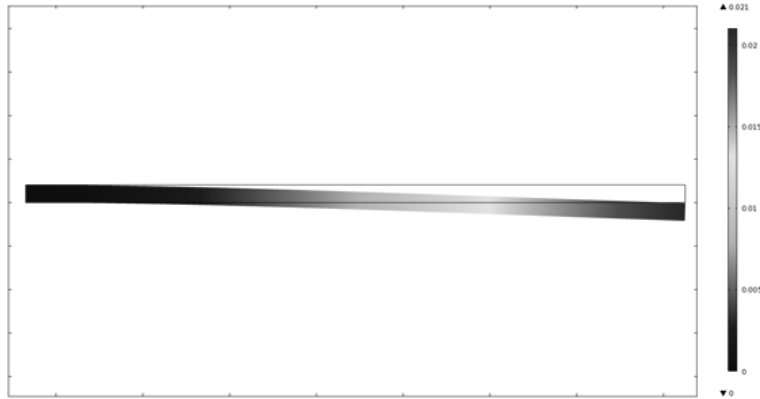


Figure 3.8: Single shim FEA setup.

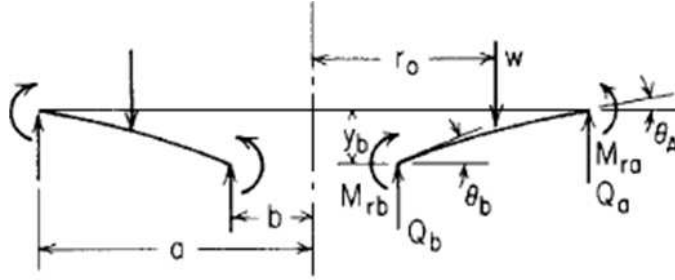


Figure 3.9: General flat plate FBD from Roark [1].

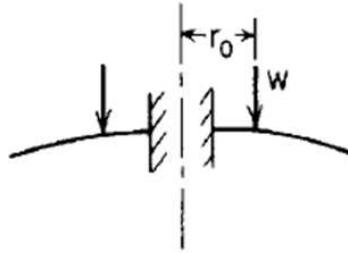


Figure 3.10: Single shim FBD from Roark [1].

The final method is experimental testing. The same shim that was used for the FEA and analytical results was subjected to a ring load. The ring load was applied by a fixture that was machined to only have a thin ring of material at the loading diameter. The shim was tested in a load frame that applied a set force and measured the displacement. The resulting stiffnesses for the three methods are given in Figure 3.11, which shows that the resulting stiffnesses are exactly the same. This makes sense, due to the simplified case that

is essentially a cantilevered beam.

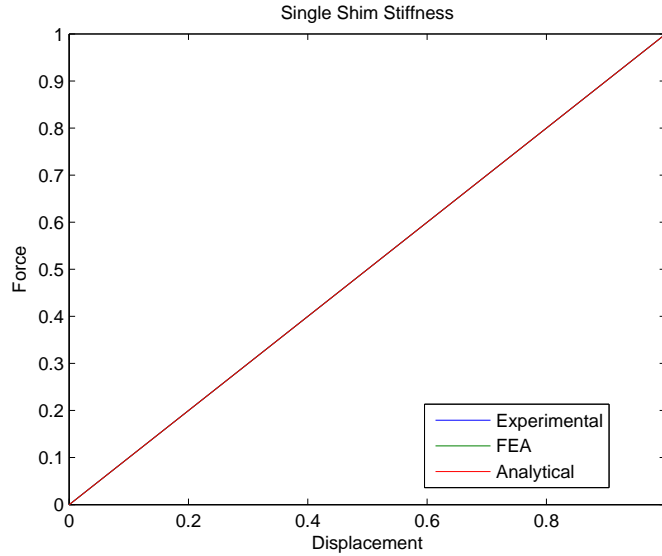


Figure 3.11: Single shim FBD from Roark.

### 3.3.2 Shim Stack Stiffness Work

The three methods match very well for a simple case, so the next step was to repeat the simple loading with multiple shims. The FEA was run with the shims modeled as a single solid part. This prevented any relative motion or other interactions between the shims. Figure 3.12 shows the setup in COMSOL. The experimental method was repeated with the stack of shims in the load frame. The same loading fixture was used. The results from the experiment were used to calculate the stiffness of the shim stack.

The analytical method needed to be adapted since Roark's analytical equations only work for a shim with constant thickness. Roark presented a method of breaking a plate with varied thicknesses into a set of equal thickness cantilevered beams, as shown in Figure 3.13. The connected beams would give the next beam an initial slope, displacement, and moment.

Talbott presented and used a method consisting of modeling each shim with a point force at the contact diameter, as shown in Figure 3.14. This method included interaction forces between the shims, which is necessary to obtain a good approximation of the actual results. The results of this method are shown in Figure 3.15. The lines on the plot are the deflections of the shims, which were compared as the interfaces between each set of shims. The shim 1 and shim 2 deflections were compared with the shim 1 line being the bottom face of shim 1 and the shim 2 line being the top face of shim 2. With this definition, shim 2 must always be below shim 1 in the plot, which Figure 3.15 shows is not the case. The shim 1 had the

largest deflection of the shims, so it would have pushed through the other shims based on this result.

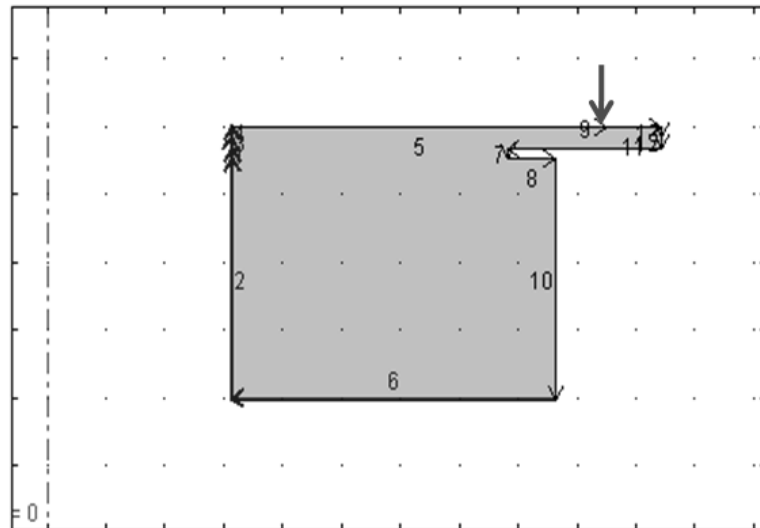


Figure 3.12: Initial FEA for the shim stack.

$$\begin{matrix} \text{[Redacted]} \\ \text{[Redacted]} \\ \text{[Redacted]} \end{matrix} = \begin{matrix} \text{[Redacted]} \\ \text{[Redacted]} \\ \text{[Redacted]} \end{matrix} + \begin{matrix} \text{[Redacted]} \\ \text{[Redacted]} \\ \text{[Redacted]} \end{matrix} + \begin{matrix} \text{[Redacted]} \\ \text{[Redacted]} \\ \text{[Redacted]} \end{matrix}$$

Figure 3.13: Shim stack analytical approach as found in [1].

The contact force option was replaced by a contact pressure case, as shown in Figure 3.16. The deflection of a shim due to a pressure loading from an inner radius to the edge of the shim is case 2l on page 467 in Roark. The issue with this case is that it does not allow a pressure to be applied from a small radius to a larger one, just from a small radius to the outer radius of the plate. Therefore two pressure loadings were needed to create the inner loading. Figure 3.17 shows the two pressure loadings, in gray and labeled c and d, needed to create the actual pressure loading on the shim, in black. The results from the contact pressure case are shown in Figure 3.18. This shows that the interfaces between shims 1 and 2 and shims 3 and 4 are not issues; however shim 2 would interfere with shim 3 in this case. Therefore the contact pressure is better than the contact force, but still not correct.

The results show that the stiffness from the FEA model was too large and the analytical stiffness was too small, when compared to experiments. Either of these options could have

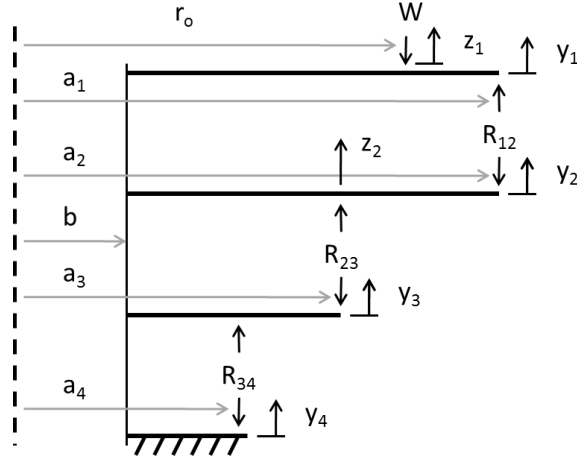


Figure 3.14: Analytical shim stack method with contact forces.

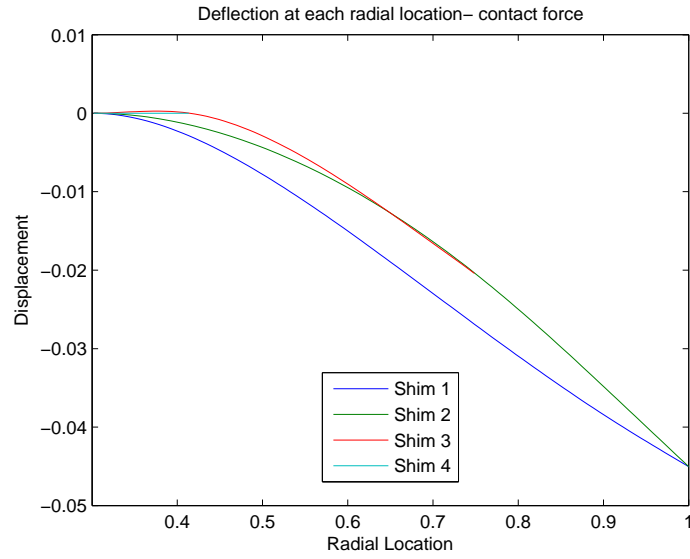


Figure 3.15: Results from analytical shim stack method with contact forces.

been refined to better match the experimental results. However the results here should have been closer since the loading was a simple ring load, the actual damper valves have more complex flow patterns. The source of the discrepancy is not known at this point and requires further investigation. Therefore the shim stiffnesses were determined by experiments.



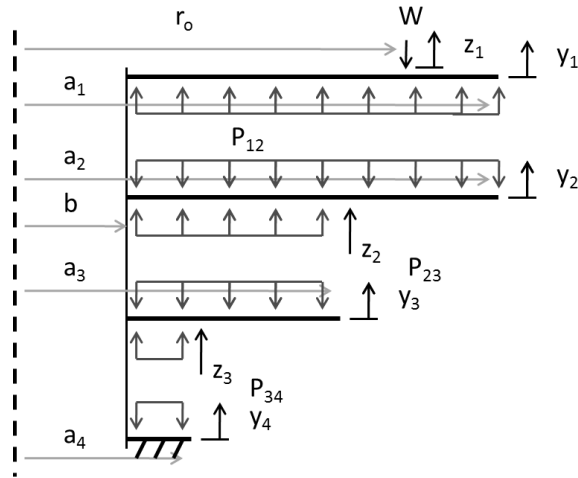


Figure 3.16: Analytical shim stack method with contact pressure.

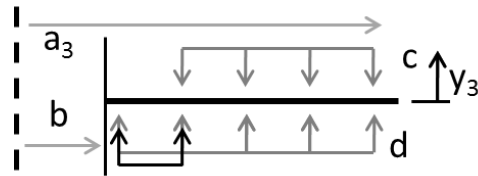


Figure 3.17: Effective contact pressure radius creation.

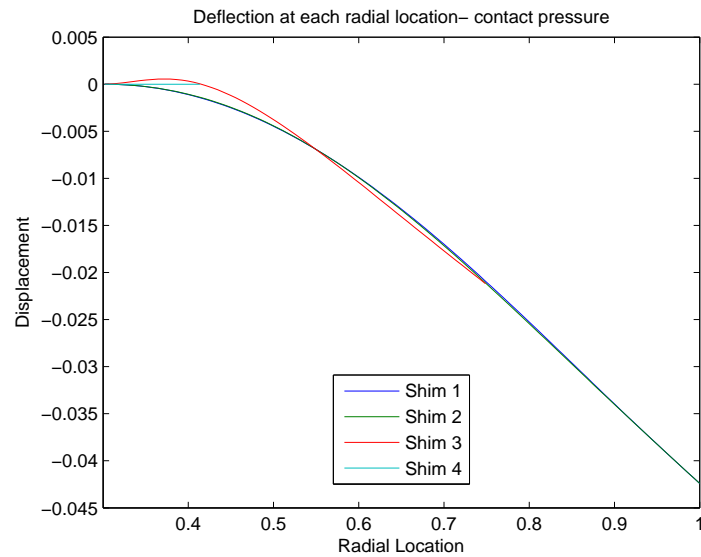


Figure 3.18: Results from analytical shim stack method with contact pressures.

### 3.3.3 Experimental Shim Stiffness Work

The experimental shim stiffness was the best option for the simple cases. The next step is upgrading the loading mechanism to approximate the actual flow areas. There are two types of orifices: slots and holes. The slots were approximated by a ring load fixture that has portions of the arc removed, so the remaining loading area is a line load in the same pattern as the slots. The holes were approximated by a ball bearing, which creates a point load at the location of the hole. These fixtures were used in the load frame to apply loads directly to the shims. The results from a shim test, shown in Figure 3.19, have three distinct sections that need to be identified: a line from 0 to 0.25 displacement, one from 0.25 to 0.5, and one from 0.5 to 0.7.

The first portion of the curve, 0 to 0.25 displacement, could be due to a slight misalignment in the fixtures. To test this hypothesis, the load frame was used to press the loading fixture into a flat rigid surface without the shims. The section from 0.25 to 0.5 displacement is likely the true shim stiffness. The section from 0.5 to 0.7 displacement is significantly stiffer than the section from 0.25 to 0.5 displacement. There are two possibilities for this stiffening: plastic deformation in the shim or the shim bottoming out against the washer on the nut holding the shims against the valve. If there was plastic deformation in the shims, then when the test was repeated, the shim stack would be stiffer the second time. The results are repeatable with no signs of stiffness change between tests. The shim bottoming out was adding a spacer with a smaller outer diameter than the backing washer to increase the distance between the shims and the backing washer.

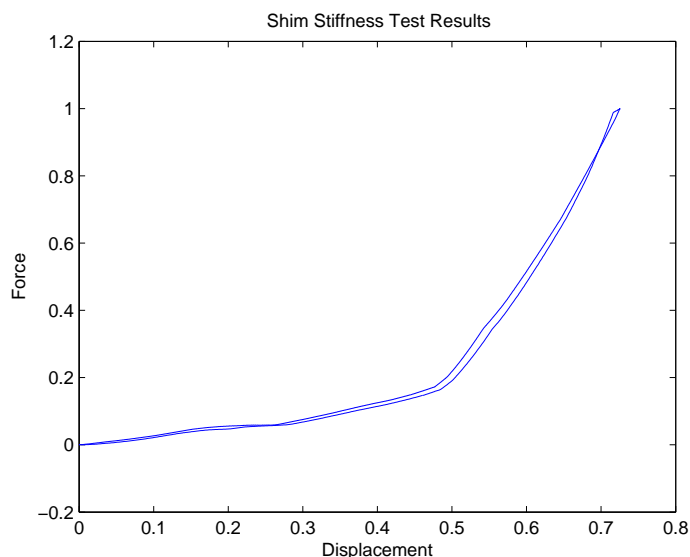


Figure 3.19: Results from a shim stiffness experiment.

Figure 3.20 shows the results of the shim test, the test with only the fixtures, and the test with the spacer. The test with only the fixtures shows that there is an initial portion of

the test where the loading fixture was not fully in contact with the mating surface. All three cases show the initial soft section before the loading fixture was fully engaged. The section of the fixtures only curve between 0.2 and 0.3 displacement is used as the fixture stiffness. The one spacer case moves the shims further from their hard stop. This extra room delayed the significant increase in the stiffness, therefore the range from 0.5 to 0.7 on the base test was due to the shims hitting a hard stop. So the section from 0.25 to 0.5 and the section from 0.5 to 0.7 displacement were used as a piecewise definition for the shim stiffness. The 0.5 to 0.7 displacement section of the curve was included since the shims could bottom out in operation if the fluid loading on the shims creates the necessary deflection.

The final step to determining the true shim stiffness is to calculate the actual stiffness from the effective stiffness in the 0.25 to 0.5 displacement section of the results and the fixture stiffness. The fixture stiffness and shim stiffness are in series, so the shim stiffness is defined as,

$$\frac{1}{k_{ef}} = \frac{1}{k_{fix}} + \frac{1}{k_{shim}}, \quad (3.5)$$

$$k_{shim} = \frac{1}{\frac{1}{k_{ef}} - \frac{1}{k_{fix}}}, \quad (3.6)$$

$$(3.7)$$

where  $k_{ef}$  is the effective shim stiffness from the measurement,  $k_{fix}$  is the fixture stiffness, and  $k_{shim}$  is the true shim stiffness that will be used in the model. Using the methods above and (3.7), the actual shim stiffness for each set of valves was calculated.

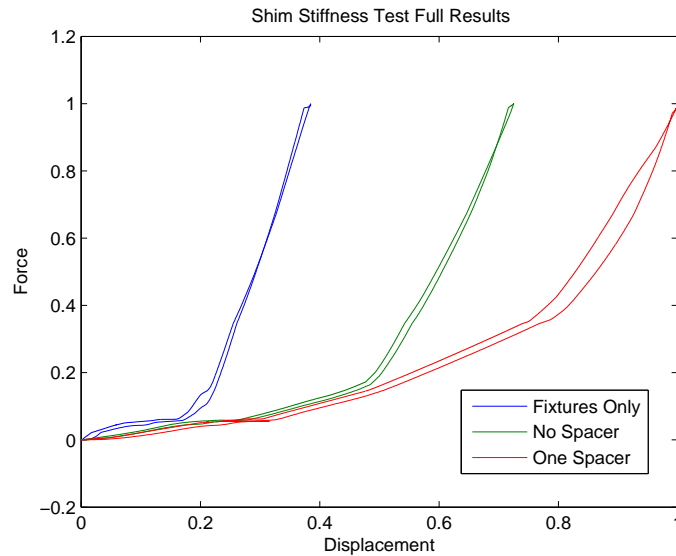


Figure 3.20: Results from each of the three shim stiffness experiment types.

### 3.4 Effective Mass

The mass of the damper sections cannot be simply measured on a scale. The damper has three main sections: the damper rod and piston, the damper body, and the fluid. The model only has two degrees of freedom, therefore there can only be two masses in the system. The fluid moves between chambers, but does not necessarily undergo the same motion as either the damper rod or damper body. Therefore the mass of the fluid was split up into effective masses for the damper rod and damper body. The effective mass of the damper body can be measured. In the dynamometer tests, the damper rod was fixed, so  $x = 0$  and  $\ddot{x} = 0$ , which allowed the damper rod equation to be solved for  $F_1$ , resulting in,

$$F_1 = -P_2 A_p + P_1 (A_p - A_r) - F_r \text{sgn}(\dot{z}). \quad (3.8)$$

So the only difference between the force on the damper rod,  $F_1$ , and the force on the damper body,  $F_2$  is the force due to the acceleration of the damper body. Figure 2.2 shows the free body diagram of the external forces on the damper. The summation of forces can be written as,

$$\Sigma F = m_{be} \ddot{y} = F_2 - P_2 A_p + P_1 (A_p - A_r) - F_r \text{sgn}(\dot{z}) = F_2 + F_1, \quad (3.9)$$

where  $m_{be}$  is the effective mass of the damper body,  $\ddot{y}$  is the acceleration of the damper body,  $F_2$  is the force on the damper body, and  $F_1$  is the force on the damper rod. This equation can be solved for the effective mass of the damper body, which yields,

$$m_{be} = \frac{F_2 + F_1}{\ddot{y}}. \quad (3.10)$$

The data needed to solve (3.10) was measured on the damper dynamometer. The only addition to the dynamometer was an extra loadcell between the actuator and the damper body to measure the force on the damper body,  $F_2$ . A couple tests were run with sinusoidal inputs and a high speed test, above 1 Hz, was used to calculate the effective mass. The effective mass was optimized based on the root mean square, RMS, error between the expressions in (3.9). The equation for the RMS error is,

$$E_{RMS} = RMS(m_{be} \ddot{y} - (F_2 + F_1)), \quad (3.11)$$

where  $E_{rms}$  is the RMS error between the effective mass and the measured forces. The optimized value was used for  $m_b$  in the model. The mass of the damper rod was measured on a scale. The mass of the damper rod was not used in the model since the damper rod was fixed. If the damper rod was moving, an effective damper rod mass would be needed.

### 3.5 Coulomb Friction

The damper has friction between the damper rod and the oil seals and between the piston and the damper walls. Figure 3.21 shows that around 0 velocity, there is a discrete shift in

the damper force, which is due to the friction. The ideal way to perform the friction test would be to remove all of the shims to prevent most of the viscous effects. However very low speed tests limit the viscous effects enough that the test can be run in the standard setup. The friction test used a triangle wave input displacement instead of a sinusoidal wave to provide constant velocity for the full cycle. The constant velocity eliminates inertial forces during the test.

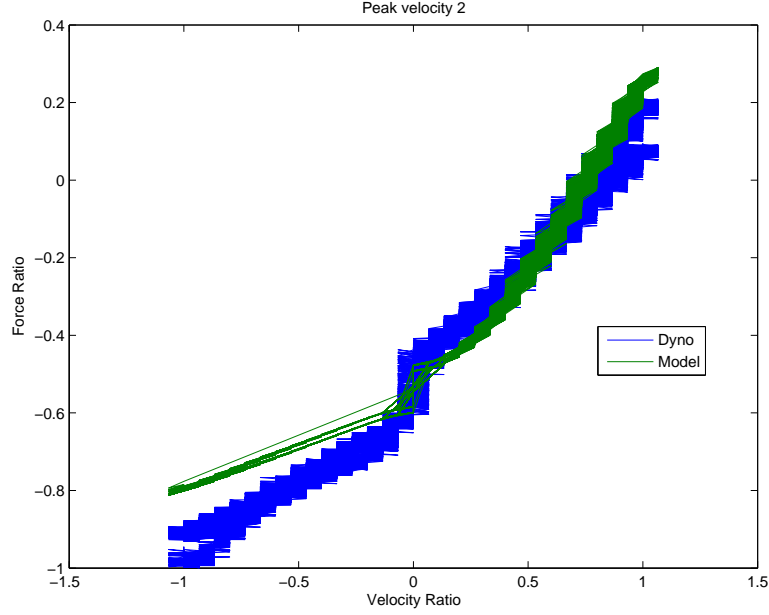


Figure 3.21: Low speed test to show coulomb friction.

The force vs. displacement plot in Figure 3.22 shows the response of the damper in these tests. The force was nearly constant for the full displacement stroke. The maximum and minimum force occur since the friction force changes direction when the damper motion changes. Therefore the resulting friction force is defined as,

$$F_r = \frac{F_{max} - F_{min}}{2}, \quad (3.12)$$

where  $F_r$  is the amplitude of the coulomb friction,  $F_{max}$  is the maximum damper force in a test, and  $F_{min}$  is the minimum damper force in a test. The damper had an initial preload due to the initial charge pressure in the damper, which caused the maximum and minimum force to have different magnitudes. This is the reason for taking the difference between the maximum and minimum forces. Figure 3.21 shows that the friction amplitude from this test matches the experimental value, based on the discrete shift in the model and dynamometer results at 0 velocity.

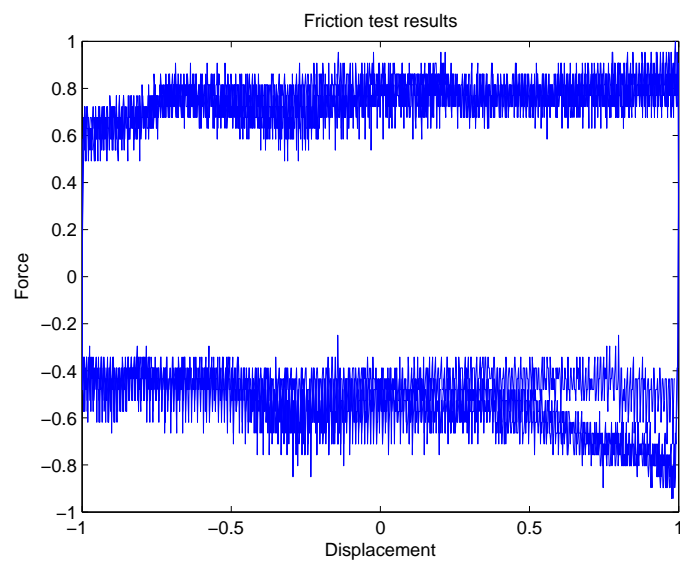


Figure 3.22: Coulomb friction force vs. displacement results.

# Chapter 4: Model Implementation

The equations defined in Chapter 2 are the basis for the model. Due to the differential equations that are part of the model, Simulink was chosen as the software to solve the set of equations. Simulink is a state space differential equation solver that is built into the MATLAB computing software.

The equations need to be organized so that they can be used to solve for the unknowns in the system. Then to help with the design analysis, the equations are setup to use dimensionless ratios instead of actual values. Once the equations are setup in this form, they can be created in Simulink.

## 4.1 Simulink Equations

The model equations are broken into 6 subsystems to allow for clean coding and an easy to follow model. This allows for a minimal number of line intersections, which helped during the building of the model and made the model less complex to someone trying to understand the model. The subsystem setup allows for variables to move between subsystems. The subsystems were chosen in a way to limit the number of variables present in a given subsystem, again for clarity of the model. The 6 subsystems are: the damper rod, the damper body, the bulk modulus, the rebound chamber, the compression chamber, and the reserve chamber.

The equations for the model were organized so that each equation solved for one of the 18 variables in the system. The damper rod subsystem consists of the equations that can be solved for the force on the damper rod,  $F_1$ , and the relative displacement between the damper rod and body,  $z$ . Equation (2.2) for the motion of the damper rod, was solved for  $F_1$  to give,

$$F_1 = m_r \ddot{x} - P_2 A_p + P_1 (A_p - A_r) + F_r \operatorname{sgn}(\dot{z}). \quad (4.1)$$

The relative displacement between the damper rod and body,  $z$ , is given in (2.4), which already is solved for  $z$ .

The damper body subsystem only includes the equation for the damper body motion, (2.5). This equation was solved for the force on the damper body,  $F_2$ , given as,

$$F_2 = m_b \ddot{y} + P_2 A_p - P_1 (A_p - A_r) - F_r \operatorname{sgn}(\dot{z}). \quad (4.2)$$

The bulk modulus subsystem consists of the equations for the bulk modulus flows of oil, which can be solved for the pressure in each chamber. The oil compressibility in the rebound chamber is given in (2.28), which was solved for  $\dot{P}_1$  to become,

$$\dot{P}_1 = \frac{q_{\beta_1} \beta_1}{(L_1 - z) (A_p - A_r)}. \quad (4.3)$$

Equation (2.30) is the equation for the compressibility of oil in the compression chamber and it was solved for  $\dot{P}_2$  with the result written as,

$$\dot{P}_2 = \frac{q_{\beta_2} \beta_2}{(L_2 + z) A_p}. \quad (4.4)$$

The reserve chamber has two options for fluid compressibility, either the oil or the gas. The compressibility of oil was chosen for consistency. Equation (2.32) was solved for  $\dot{P}_3$  and written as,

$$\dot{P}_3 = \frac{q_{\beta_{31}} \beta_{31}}{V_{31}}. \quad (4.5)$$

The rebound chamber subsystem consists of equations that solve for the flows through the damper piston and the compressibility of the oil in the rebound chamber. Equation (2.6) is the equation for the flow continuity of the rebound chamber and it was solved for the compressibility of the oil in the rebound chamber. The resulting equation is given as,

$$q_{\beta_1} = \dot{z} (A_p - A_r) - q_{11} - q_{12} - q_{22}. \quad (4.6)$$

The flow through the piston bleed orifice is given in (2.10), which is rewritten here,

$$q_{11} = n_{11} C_{d11} A_{11} \operatorname{sgn}(P_1 - P_2) \sqrt{\frac{2 |P_1 - P_2|}{\rho}}. \quad (4.7)$$

The flow through the piston check valve from the compression chamber to the rebound chamber is given in (2.16) and is rewritten as,

$$q_{12} = 0 \quad P_1 \geq P_2, \quad (4.8)$$

$$q_{12} = -C_{d12} \pi D_{v12} \frac{|P_1 - P_2| A_{f12} n_{12}}{K_1} \sqrt{\frac{2 |P_1 - P_2|}{\rho}} \quad P_1 < P_2. \quad (4.9)$$

The piston has a second check valve that allows flow from the rebound chamber to the compression chamber,  $q_{22}$ . This flow is defined in (2.18) and shown below as,

$$q_{22} = 0 \quad P_1 \leq P_2, \quad (4.10)$$

$$q_{22} = C_{d22} \pi D_{v22} \frac{|P_1 - P_2| A_{f22} n_{22}}{K_2} \sqrt{\frac{2 |P_1 - P_2|}{\rho}} \quad P_1 > P_2. \quad (4.11)$$

The compression chamber subsystem includes equations for the flows through the fixed valve and the compressibility of the oil in the compression chamber. Equation (2.7) is the flow continuity equation for the compression chamber and it can be solved for the compressibility of the oil in the compression chamber,  $q_{\beta_2}$ . The resulting equation is given as,

$$q_{\beta_2} = q_{11} + q_{12} + q_{22} - q_{31} - q_{32} - q_{42} - \dot{z} A_p. \quad (4.12)$$

The flow through the fixed valve bleed orifice is given by (2.11), which is given as,

$$q_{31} = n_{31} C_{d31} A_{31} \operatorname{sgn}(P_2 - P_3) \sqrt{\frac{2 |P_2 - P_3|}{\rho}}. \quad (4.13)$$



The flow through the fixed check valve from the compression chamber to the reserve chamber is given in (2.20) and is written as,

$$q_{32} = 0 \quad P_3 \geq P_2, \quad (4.14)$$

$$q_{32} = C_{d32} \pi D_{v32} \frac{|P_2 - P_3| A_{f32} n_{32}}{K_3} \sqrt{\frac{2 |P_2 - P_3|}{\rho}} \quad P_3 < P_2. \quad (4.15)$$

The flow through the fixed check valve from the reserve chamber to the compression chamber is given in (2.22) and is shown here as,

$$q_{42} = 0 \quad P_3 \leq P_2, \quad (4.16)$$

$$q_{42} = -C_{d42} \pi D_{v42} \frac{|P_2 - P_3| A_{f42} n_{42}}{K_4} \sqrt{\frac{2 |P_2 - P_3|}{\rho}} \quad P_3 > P_2. \quad (4.17)$$

The reserve chamber subsystem includes equations that solve for the compressibility of both gas and oil in the reserve chamber and the volumes of gas and oil in the reserve chamber. Equation (2.8) is the flow continuity equation for the reserve chamber and was used to solve for the compressibility of the oil in this chamber. The resulting equation is shown to be,

$$q_{\beta 31} = q_{31} + q_{32} + q_{42} - q_{\beta 32}. \quad (4.18)$$

The fluid compressibility equation for the gas in the reserve chamber is (2.33). This equation was solved for the flow due to the compressibility of gas,  $q_{\beta 32}$ , which results in,

$$q_{\beta 32} = \dot{P}_3 \frac{V_{32}}{\beta_{32}}. \quad (4.19)$$

The equation for the conservation of volume in the reserve chamber is (2.34) and was solved for the instantaneous volume of oil in the reserve chamber,  $V_{31}$ . This results in the expression written as,

$$V_{31} = V_3 - V_{32}. \quad (4.20)$$

Equation (2.37) is the bulk modulus equation written for the gas in the reserve chamber. This equation was solved to calculate the instantaneous volume of gas in the reserve chamber,  $V_{32}$ , which is written as,

$$V_{32} = V_{32o} \left( 1 - \frac{P_3 - P_{3o}}{\beta_{32}} \right). \quad (4.21)$$

These equations are setup so that each of the 18 variables is an expression of the other 17 variables and input parameters. This will allow for the equations to be entered into Simulink. One more step is required to increase the applications of this model, that step is to rewrite the equations in dimensionless form. This allows for the ratios of certain components and results to be analyzed in lieu of the actual values. This type of analysis gives both qualitative and quantitative results without disclosing the true output values.

## 4.2 Dimensionless Ratio Equations

There are two main reasons to use dimensionless variables. The first reason is to compare different design conditions. Ideally the value of the dimensionless conversion parameter used to create the dimensionless ratio does not affect the qualitative results of the system, only the ratio itself affects the results. This is true when the parameter is held constant for a number of different ratios. The second reason is to eliminate the actual values from the input parameters and the results. This allows for detailed results of a proprietary system without disclosing important information about the true system.

For this model, there are 13 parameters needed to convert inputs and outputs of the system to dimensionless values. Table 4.1 lists the type of parameter that is needed based on the physical concept, such as force and pressure. Also included is the symbol and expression for the parameter.

These parameters are used to convert variables to dimensionless quantities that are written as,

$$P_{1.r} = \frac{P_1}{P_o}, \quad (4.22)$$

where  $P_{1.r}$  is the dimensionless ratio used to describe the pressure in the rebound chamber,  $P_1$  is the pressure in the rebound chamber, and  $P_o$  is the dimensionless conversion parameter for pressure. A complete list of the dimensionless ratios is shown in Table 4.2.

The equations with the dimensionless ratios are the same as the equations given in Section 4.1. Tables 4.3-4.8 show the equations in dimensionless form for Simulink.

Table 4.1: Dimensionless conversion parameters.

Type	Par. name	Relation	Description
Acceleration ( $m/s^2$ )	$a_o$	$L_o f_o^2$	Char. length and damper freq.
Area ( $m^2$ )	$A_o$	$A_r$	Damper rod area
Density ( $kg/m^3$ )	$\rho_o$	$m_o/V_o$	Char. mass by char. volume
Diameter (m)	$d_o$	$d_r$	Rod diameter
Flow ( $m^3/s$ )	$q_o$	$Vel_o A_o$	Char. length and area
Force (N)	$F_o$	$F_{1max}$	Maximum damper force
Frequency (Hz)	$f_o$	$f$	Damper motion freq.
Length (m)	$L_o$	$d_p$	Piston diameter
Mass (kg)	$m_o$	$m_t$	Total damper mass
Pressure (Pa)	$P_o$	$P_o$	Initial damper pressure
Stiffness (N/m)	$k_o$	$F_o/L_o$	Char. force and length
Velocity (m/s)	$Vel_o$	$V_{max}$	Max. velocity for the run
Volume ( $m^3$ )	$V_o$	$L_o A_o$	Char. length and area

Table 4.2: Dimensionless ratios for model variables.

$F_{1.r} = \frac{F_1}{F_o}$	$m_{r.r} = \frac{m_r}{m_o}$	$\ddot{x}_{.r} = \frac{\ddot{x}}{a_o}$	$P_{2.r} = \frac{P_2}{P_o}$	$A_{p.r} = \frac{A_p}{A_o}$
$P_{1.r} = \frac{P_1}{P_o}$	$A_{r.r} = \frac{A_r}{A_o}$	$F_{r.r} = \frac{F_r}{F_o}$	$\dot{z}_{.r} = \frac{\dot{z}}{V_{el_o}}$	$m_{b.r} = \frac{m_b}{m_o}$
$\dot{P}_{1.r} = \frac{\dot{P}_1}{P_o f_o}$	$q_{\beta 1.r} = \frac{q_{\beta 1}}{q_o}$	$\beta_{1.r} = \frac{\beta_1}{P_o}$	$L_{1.r} = \frac{L_1}{L_o}$	$z_{.r} = \frac{z}{L_o}$
$\dot{P}_{2.r} = \frac{\dot{P}_2}{P_o f_o}$	$q_{\beta 2.r} = \frac{q_{\beta 2}}{q_o}$	$\beta_{2.r} = \frac{\beta_2}{P_o}$	$L_{2.r} = \frac{L_2}{L_o}$	$\dot{P}_{3.r} = \frac{\dot{P}_3}{P_o f_o}$
$q_{\beta 31.r} = \frac{q_{\beta 31}}{q_o}$	$\beta_{31.r} = \frac{\beta_{31}}{P_o}$	$V_{31.r} = \frac{V_{31}}{V_o}$	$q_{11.r} = \frac{q_{11}}{q_o}$	$q_{12.r} = \frac{q_{12}}{q_o}$
$q_{22.r} = \frac{q_{22}}{q_o}$	$A_{11.r} = \frac{A_{11}}{A_o}$	$\rho_{.r} = \frac{\rho}{\rho_o}$	$D_{v12.r} = \frac{D_{v12}}{d_o}$	$A_{f12.r} = \frac{A_{f12}}{A_o}$
$K_{1.r} = \frac{K_1}{K_o}$	$D_{v22.r} = \frac{D_{v22}}{d_o}$	$A_{f22.r} = \frac{A_{f22}}{A_o}$	$K_{2.r} = \frac{K_2}{K_o}$	$q_{31.r} = \frac{q_{31}}{q_o}$
$q_{32.r} = \frac{q_{32}}{q_o}$	$q_{42.r} = \frac{q_{42}}{q_o}$	$A_{31.r} = \frac{A_{31}}{A_o}$	$D_{v32.r} = \frac{D_{v32}}{d_o}$	$P_{3.r} = \frac{P_3}{P_o}$
$A_{f32.r} = \frac{A_{f32}}{A_o}$	$K_{3.r} = \frac{K_3}{K_o}$	$D_{v42.r} = \frac{D_{v42}}{d_o}$	$A_{f42.r} = \frac{A_{f42}}{A_o}$	$K_{4.r} = \frac{K_4}{K_o}$
$q_{\beta 32.r} = \frac{q_{\beta 32}}{q_o}$	$\beta_{32.r} = \frac{\beta_{32}}{P_o}$	$V_{32.r} = \frac{V_{32}}{V_o}$	$V_{32o.r} = \frac{V_{32o}}{V_o}$	$P_{3o.r} = \frac{P_{3o}}{P_o}$

Table 4.3: Dimensionless equations for the damper rod subsystem.

---


$$F_o F_{1-r} = m_o m_{r-r} a_o \ddot{x}_{-r} - P_o P_{2-r} A_o A_{p-r} + P_o P_{1-r} A_o (A_{p-r} - A_{r-r}) + F_o F_{r-r} \text{sgn}(Vel_o \dot{z}_{-r})$$

$$L_o z_{-r} = L_o x_{-r} - L_o y_{-r}$$


---

Table 4.4: Dimensionless equations for the damper body subsystem.

---


$$F_o F_{2-r} = m_o m_{b-r} a_o \ddot{y}_{-r} + P_o P_{2-r} A_o A_{p-r} - P_o P_{1-r} A_o (A_{p-r} - A_{r-r}) - F_o F_{r-r} \text{sgn}(Vel_o \dot{z}_{-r})$$


---

Table 4.5: Dimensionless equations for the bulk modulus subsystem.

---


$$P_o f_o \dot{P}_{1-r} = \frac{q_o q_{\beta_{1-r}} P_o \beta_{1-r}}{L_o (L_{1-r} - z_{-r}) A_o (A_{p-r} - A_{r-r})}$$

$$P_o f_o \dot{P}_{2-r} = \frac{q_o q_{\beta_{2-r}} P_o \beta_{2-r}}{L_o (L_{2-r} + z_{-r}) A_o A_{p-r}}$$

$$P_o f_o \dot{P}_{3-r} = \frac{q_o q_{\beta_{31-r}} P_o \beta_{31-r}}{V_o V_{31-r}}$$


---

Table 4.6: Dimensionless equations for the rebound chamber subsystem.

---


$$q_o q_{\beta_{1.r}} = Vel_o \dot{z}_{.r} A_o (A_{p.r} - A_{r.r}) - q_o q_{11.r} - q_o q_{12.r} - q_o q_{22.r}$$

$$q_o q_{11.r} = n_{11} C_{d11} A_o A_{11.r} \operatorname{sgn}(P_o(P_{1.r} - P_{2.r})) \sqrt{\frac{2 P_o |P_{1.r} - P_{2.r}|}{\rho_o \rho_{.r}}}$$

$$q_o q_{12.r} = -C_{d12} \pi d_o D_{v12.r} \frac{P_o |P_{1.r} - P_{2.r}| A_o A_{f12.r} n_{12}}{K_o K_{1.r}} \sqrt{\frac{2 P_o |P_{1.r} - P_{2.r}|}{\rho_o \rho_{.r}}} \quad P_{1.r} < P_{2.r}$$

$$q_o q_{22.r} = C_{d22} \pi d_o D_{v22.r} \frac{P_o |P_{1.r} - P_{2.r}| A_o A_{f22.r} n_{22}}{K_o K_{2.r}} \sqrt{\frac{2 |P_{1.r} - P_{2.r}|}{\rho_o \rho_{.r}}} \quad P_{1.r} > P_{2.r}$$


---

Table 4.7: Dimensionless equations for the compression chamber subsystem.

---


$$q_o q_{\beta_{2.r}} = q_o q_{11.r} + q_o q_{12.r} + q_o q_{22.r} - q_o q_{31.r} - q_o q_{32.r} - q_o q_{42.r} - Vel_o \dot{z}_{.r} A_o A_{p.r}$$

$$q_o q_{31.r} = n_{31} C_{d31} A_o A_{31.r} \operatorname{sgn}(P_o(P_{2.r} - P_{3.r})) \sqrt{\frac{2 P_o |P_{2.r} - P_{3.r}|}{\rho_o \rho_{.r}}}$$

$$q_o q_{32.r} = C_{d32} \pi d_o D_{v32.r} \frac{P_o |P_{2.r} - P_{3.r}| A_o A_{f32.r} n_{32}}{K_o K_{3.r}} \sqrt{\frac{2 P_o |P_{2.r} - P_{3.r}|}{\rho_o \rho_{.r}}} \quad P_{3.r} < P_{2.r}$$

$$q_o q_{42.r} = -C_{d42} \pi d_o D_{v42.r} \frac{P_o |P_{2.r} - P_{3.r}| A_o A_{f42.r} n_{42}}{K_o K_{4.r}} \sqrt{\frac{2 P_o |P_{2.r} - P_{3.r}|}{\rho_o \rho_{.r}}} \quad P_{3.r} > P_{2.r}$$


---

Table 4.8: Dimensionless equations for the reserve chamber subsystem.

---


$$q_o q_{\beta 31.r} = q_o q_{31.r} + q_o q_{32.r} + q_o q_{42.r} - q_o q_{\beta 32.r}$$

$$q_o q_{\beta 32.r} = P_o f_o \dot{P}_{3.r} \frac{V_o V_{32.r}}{P_o \beta_{32.r}}$$

$$V_o V_{31.r} = V_o V_{3.r} - V_o V_{32.r}$$

$$V_o V_{32.r} = V_o V_{32o.r} \left( 1 - \frac{P_o (P_{3.r} - P_{3o.r})}{P_o \beta_{32.r}} \right)$$


---

### 4.3 Simulink Model Setup

The previous two sections setup the equations for Simulink. This section will describe the Simulink diagram. As mentioned above, the model is broken into 6 subsystems. The 6 subsystems are: the damper rod equation, the damper body equation, the bulk modulus equations, the rebound chamber equations, the compression chamber equations, and the reserve chamber equations. Each subsystem contains one or more equation that is solved and a set of variables that are passed to the subsystems above and below. The top level of the Simulink just consists of the input displacement ratio and the output force ratio. The Simulink setup for the top level is shown in Figure 4.3.

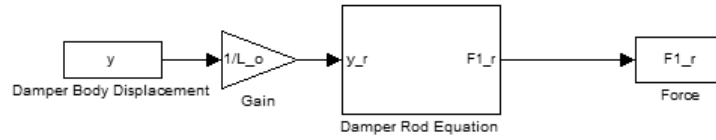


Figure 4.1: Simulink model top level.

#### 4.3.1 Damper Rod Equation

The first subsystem of the Simulink model is the equation for the damper rod motion and is shown in Figure 4.2. The equations for this subsystem are given in Table 4.3. This subsystem uses the damper rod and body displacement ratios,  $x_r$  and  $y_r$ , respectively, from the input data. The pressure ratio in the rebound chamber,  $P_{1,r}$ , and pressure ratio in the compression chamber,  $P_{2,r}$ , are determined in Section 4.3.3 and used to solve for the force ratio on the damper rod,  $F_{1,r}$ . This setup is fairly messy due to gain blocks used to convert values from dimensionless ratios to true values.

This subsystem passes the damper body displacement ratio,  $y_r$ , and the relative displacement between the damper rod and body,  $z_r$ , to the damper body equation subsystem, which is shown in Section 4.3.2. The pressure ratios in the rebound chamber,  $P_{1,r}$ , and ratio in the compression chamber,  $P_{2,r}$ , are sent up from the damper body equation subsystem.

#### 4.3.2 Damper Body Equation

The second subsystem is shown in Figure 4.3 and is for the damper body equation. This subsystem uses the equations shown in Table 4.4 to solve for the force ratio on the damper body,  $F_{2,r}$ . This subsystem uses the pressure ratios for the rebound chamber,  $P_{1,r}$ , and the compression chamber,  $P_{2,r}$ , along with the damper body acceleration ratio,  $\ddot{y}_r$ , and the relative displacement ratio between the damper rod and body,  $z_r$ .  $z_r$  is passed down to the





### 4.3.3 Bulk Modulus Equations

Figure 4.4 is third subsystem in the Simulink model and is used for the bulk modulus equations. This subsystem solves the equations in Table 4.5, to solve for the pressure in each of the 3 chambers. The equations are implemented in 3 individual subsystems within the bulk modulus equation subsystem. The bulk modulus equation subsystem passes the relative displacement,  $z_r$ , the pressure ratios in the rebound and compression chambers,  $P_{1,r}$  and  $P_{2,r}$  respectively, and the time derivative of the pressure ratio in the reserve chamber,  $\dot{P}_{3,r}$ , to the Chamber 1, rebound chamber, subsystem that is described in Section 4.3.4. The flow due to compressibility of oil in the rebound chamber,  $q_{\beta_{1,r}}$ , compression chamber,  $q_{\beta_{2,r}}$ , and reserve chamber,  $q_{\beta_{31,r}}$ , and the instantaneous volume of oil in the reserve chamber,  $V_{31,r}$ , are brought up from the Chamber 1 subsystem.

Figure 4.5 is the subsystem used to determine the pressure in the rebound chamber. The first equation in Table 4.5 is the equation for the time derivative of pressure in the rebound chamber. This result can be integrated to find the rebound chamber pressure ratio. The only thing needed in the integral is the initial pressure. This is determined from the initial charge pressure of the damper. The subsystem uses the relative displacement,  $z_r$ , and the flow due to compressibility of oil in the rebound chamber,  $q_{\beta_{1,r}}$  from the bulk modulus subsystem and sends the pressure ratio in the rebound chamber,  $P_{1,r}$ , up to the bulk modulus subsystem.

Figure 4.6 is the subsystem used to determine the pressure in the compression chamber. The second equation in Table 4.5 is the equation for the time derivative of pressure in the compression chamber. The integral of this result yields the compression chamber pressure ratio, with the initial pressure equal to the damper charge pressure. The subsystem uses the relative displacement,  $z_r$ , and the flow due to compressibility of oil in the compression chamber,  $q_{\beta_{2,r}}$  from the bulk modulus subsystem and sends the pressure ratio in the compression chamber,  $P_{2,r}$ , up to the bulk modulus subsystem.

Figure 4.7 is the subsystem used to determine the pressure in the reserve chamber. The third equation in Table 4.5 is used to find the time derivative of pressure in the reserve chamber. This result can be integrated to find the reserve chamber pressure ratio. As mentioned above, the initial pressure is the charge pressure of the damper. The subsystem uses the volume of oil in the reserve chamber,  $V_{31,r}$ , and the flow due to compressibility of oil in the reserve chamber,  $q_{\beta_{31,r}}$  from the bulk modulus subsystem and sends the time derivative of pressure in the reserve chamber,  $\dot{P}_{3,r}$ , up to the bulk modulus subsystem.

### 4.3.4 Rebound Chamber Equations

The rebound chamber subsystem is the fourth subsystem that is shown in Figure 4.8. The equations for this subsystem are shown in Table 4.6. The first equation in Table 4.6 is used to solve for the flow from the compressibility of oil in the rebound chamber,  $q_{\beta_{1,r}}$ . There are blocks for each of the 3 piston orifice flows within this subsystem. The rebound chamber equation subsystem sends the time derivative of the reserve chamber pressure,  $\dot{P}_{3,r}$ , the pressure in the compression chamber,  $P_{2,r}$ , the 3 orifice flows,  $q_{11,r}$ ,  $q_{12,r}$ , and  $q_{22,r}$ , and the relative displacement,  $z_r$ , to the compression chamber, which is described in Section 4.3.5.

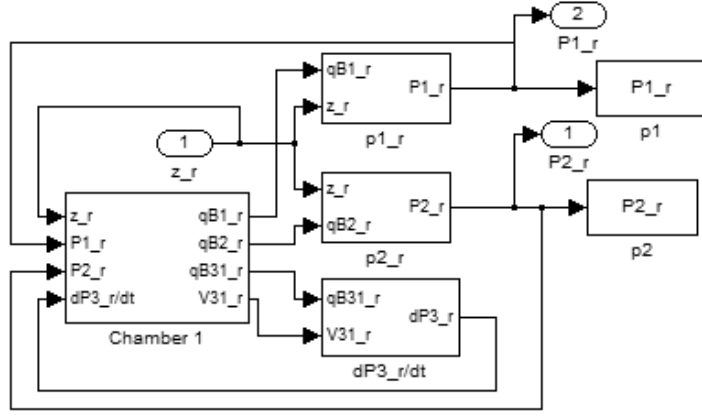


Figure 4.4: Simulink model bulk modulus equations.

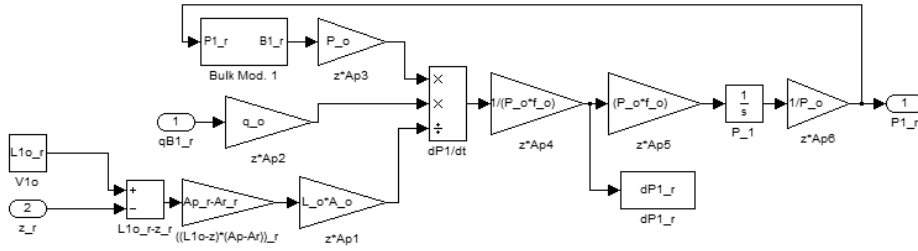


Figure 4.5: Simulink model rebound chamber pressure equation.

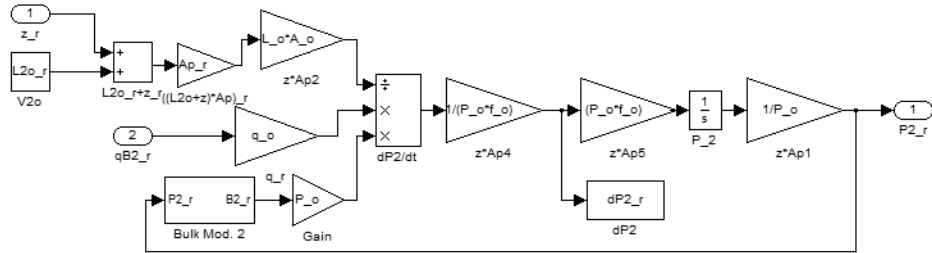


Figure 4.6: Simulink model compression chamber pressure equation.

This subsystem receives the flows due to compressibility for the compression chamber,  $q_{\beta 2_r}$ , and the reserve chamber,  $q_{\beta 31_r}$ , and the volume of oil in the reserve chamber,  $V_{31_r}$ , from the compression chamber subsystem.

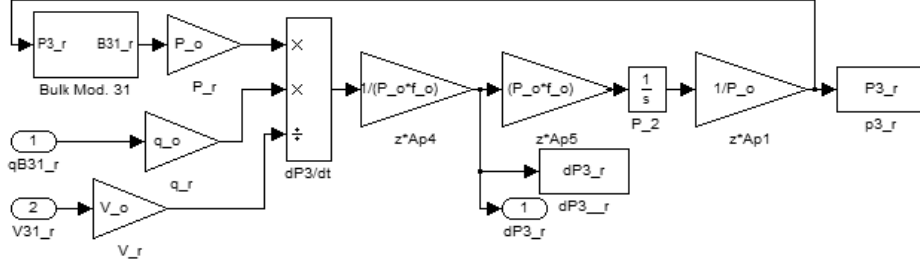


Figure 4.7: Simulink model reserve chamber pressure equation.

The subsystem for the piston bleed orifice flow,  $q_{11,r}$ , is shown in Figure 4.9. This subsystem is based on the second equation in Table 4.6. It uses this equation to determine the magnitude and direction of flow  $q_{11,r}$ . This subsystem uses the pressure ratio difference between the rebound and compression chambers,  $P_{1,r} - P_{2,r}$ , from the rebound chamber subsystem and sends the resulting piston bleed orifice flow up to the rebound chamber subsystem.

The subsystem for the piston check valve for flow to the rebound chamber is shown in Figure 4.10. This subsystem is based on the third equation in Table 4.6. It uses this equation to determine the magnitude of flow  $q_{12,r}$ . This subsystem uses the pressure ratio difference between the rebound and compression chambers,  $P_{1,r} - P_{2,r}$ , from the rebound chamber subsystem and sends the resulting flow,  $q_{12,r}$ , up to the rebound chamber subsystem.

Figure 4.11 shows the subsystem for the piston check valve for flow to the compression chamber. This subsystem is based on the fourth equation in Table 4.6. The magnitude of flow  $q_{22,r}$  is determined from this equation. This subsystem uses the pressure ratio difference between the rebound and compression chambers,  $P_{1,r} - P_{2,r}$ , from the rebound chamber subsystem and sends the resulting flow,  $q_{22,r}$ , up to the rebound chamber subsystem.

### 4.3.5 Compression Chamber Equations

The fifth subsystem is shown in Figure 4.12 for the compression chamber equations. The equations for this subsystem are listed in Table 4.7. The first equation is used to solve for the flow due to the compressibility of the oil in the compression chamber,  $q_{\beta_{2,r}}$ . This equation shown in Figure 4.12. This subsystem contains blocks for the 3 orifice flows in the fixed valve. The compression chamber subsystem sends the time derivative of the pressure in reserve chamber,  $\dot{P}_{3,r}$ , and the 3 fixed valve orifice flows,  $q_{31,r}$ ,  $q_{32,r}$ , and  $q_{42,r}$ , to the reserve chamber equation subsystem, which is described in Section 4.3.6. This subsection receives the flow due to compressibility for the reserve chamber,  $q_{\beta_{31,r}}$ , and the volume of oil in the reserve chamber,  $V_{31,r}$ , from the reserve chamber equations subsystem.

The subsystem for the fixed valve bleed orifice flow,  $q_{31,r}$ , is shown in Figure 4.13. This subsystem is based on the second equation in Table 4.7. It uses this equation to determine the magnitude and direction of flow  $q_{31,r}$ . This subsystem uses the pressure ratio difference

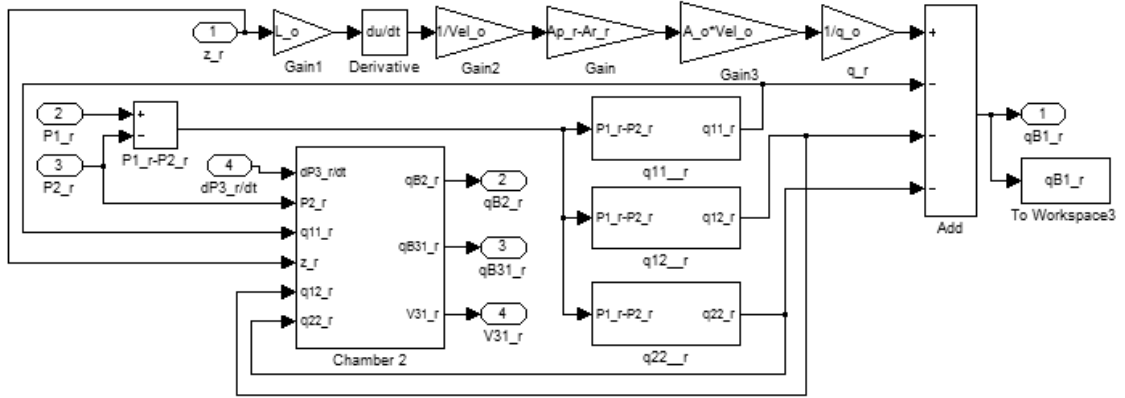


Figure 4.8: Simulink model rebound chamber equations.

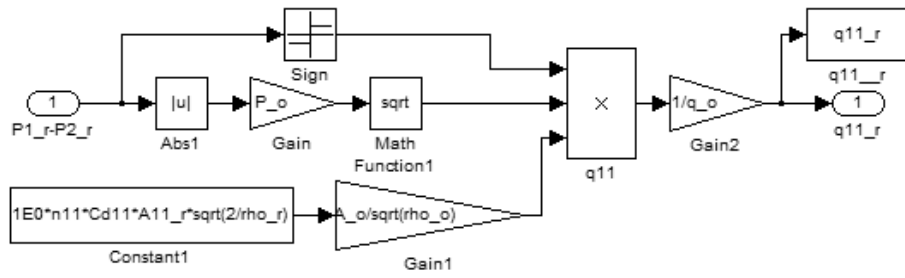


Figure 4.9: Simulink model piston bleed valve equation.

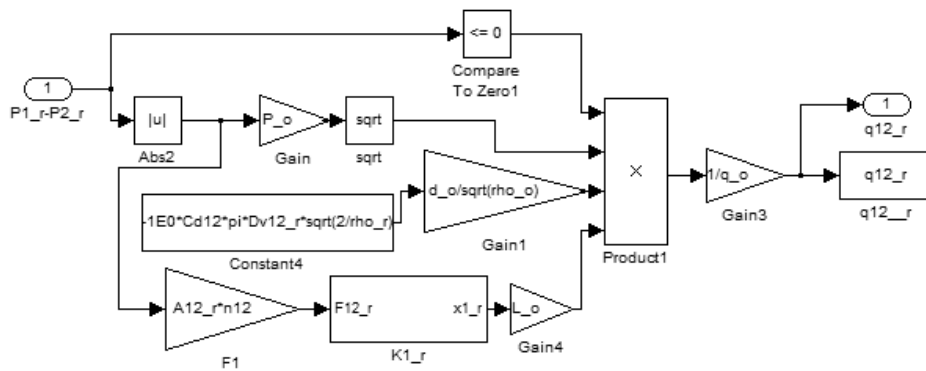


Figure 4.10: Simulink model equation for the piston check valve for flow  $q_{12}$ .

between the compression and reserve chambers,  $P_{2,r} - P_{3,r}$ , from the compression chamber subsystem and sends the resulting piston bleed orifice flow up to the compression chamber



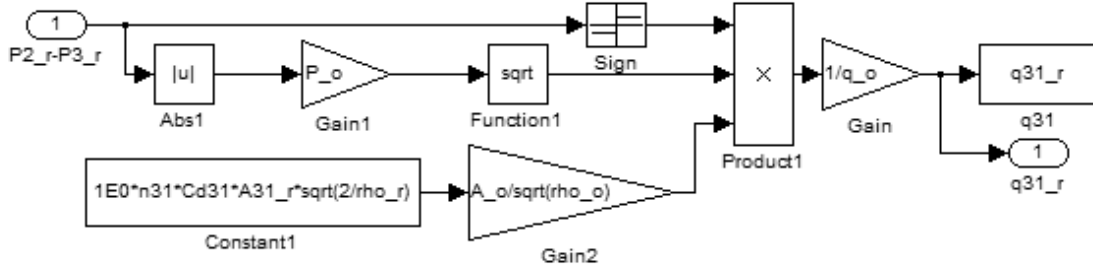


Figure 4.13: Simulink model fixed valve bleed orifice equation.

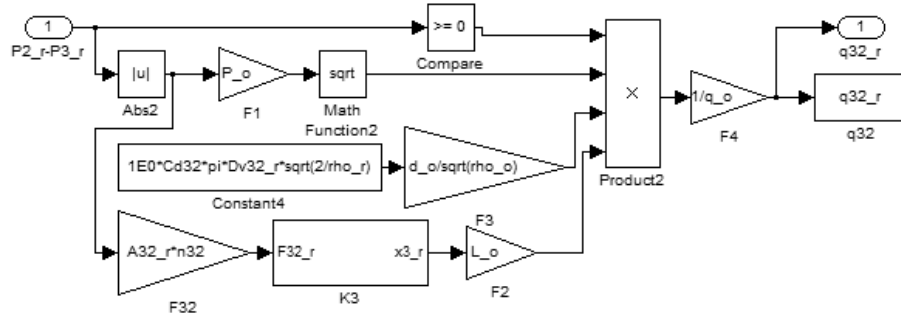


Figure 4.14: Simulink model equation for the fixed valve check valve for flow  $q_{32}$ .

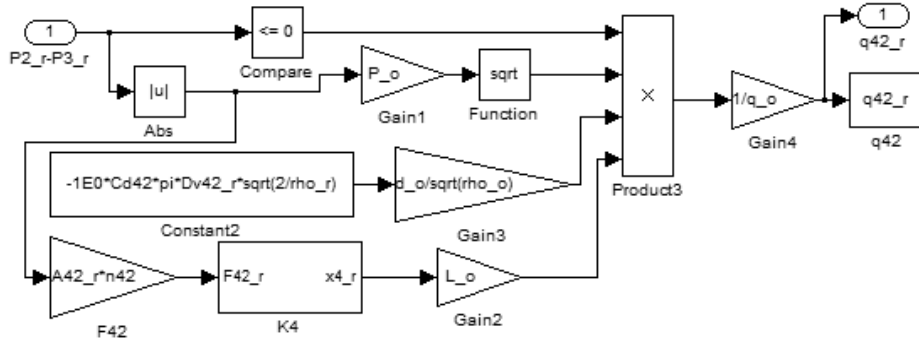


Figure 4.15: Simulink model equation for the fixed valve check valve for flow  $q_{42}$ .

### 4.3.6 Reserve Chamber Equations

The sixth and final subsystem is the reserve chamber equations subsystem and is shown in Figure 4.16. This subsystem uses the equations in Table 4.8. The first equation in Table 4.8

is used to solve for the flow due to compressibility of oil in the reserve chamber,  $q_{\beta_{31_r}}$ , using the other flows in the reserve chamber  $q_{31_r}$ ,  $q_{32_r}$ ,  $q_{42_r}$ , and  $q_{\beta_{32_r}}$ . The second equation is used to solve for the flow due to compressibility of gas in the reserve chamber,  $q_{\beta_{32_r}}$ , using the time derivative of the pressure in the reserve chamber,  $\dot{P}_{3_r}$ , and the volume of oil in the reserve chamber,  $V_{32_r}$ .

The volume of oil in the reserve chamber,  $V_{32_r}$ , is found using equation third equation in Table 4.8. This equation uses the total volume of chamber 3,  $V_{3_r}$ , and the volume of gas in the reserve chamber,  $V_{32_r}$ . The fourth equation in Table 4.8 is used to solve for the volume of gas in the reserve chamber,  $V_{32_r}$ . This equation is solved using the pressure ratio in the reserve chamber,  $P_{3_r}$ , the initial pressure in the reserve chamber,  $P_{3o_r}$ , the bulk modulus of gas in the reserve chamber,  $\beta_{32_r}$ , and the initial volume of gas in the reserve chamber,  $V_{32o_r}$ . As mentioned at the beginning of this section, this is the last subsystem in the Simulink model. Once the model is created, it needs to be verified with actual experimental data.

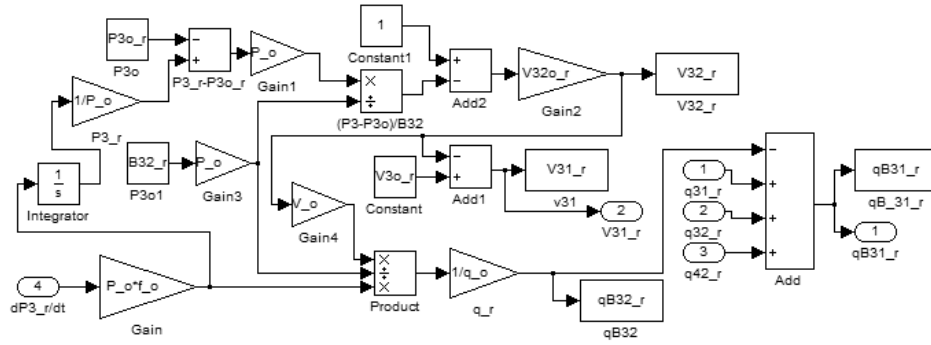


Figure 4.16: Simulink model reserve chamber equations.

# Chapter 5: Model Validation

The damper model created in this work models a stock twin tube damper. The advantage of using this stock part is that experiments can be performed on the part and compared to the model results. The experimental procedure was a traditional constant frequency, displacement controlled test performed on a damper dynamometer. The experiments were performed at 8 different frequencies. The results from the experiments were compared directly to model simulations with the same displacement profile.

## 5.1 Damper Experiments

A damper dynamometer is the traditional machine used to test dampers. The main reason for its use is that it is very good at producing desired dynamic displacement and velocity profiles. The experiments for this study were performed on a dynamometer at Honda R&D Americas Inc. in Raymond, Ohio. Figure 5.1 is a schematic of the dynamometer setup. The dynamometer uses an Electro-Magnetic (EM) linear actuator for motion. The damper body was attached to the actuator output, which has a female threaded attachment point. The load cell was attached to the top beam of the damper and contains female threads to mount the damper rod. The top beam can be adjusted to account for dampers of different lengths and slightly compress the damper initially.

There are two main output sensors on the dynamometer. The load cell at the top of the damper rod measured the force defined as  $F_1$  in Figure 2.2. There is a displacement sensor in the linear actuator that measured the displacement of the damper body, then the velocity was calculated from the measured displacement. The actual experimental setup simplifies parts of the model. The top beam was fixed, so the damper rod displacement,  $x$ , was fixed at 0 in the model. The actuator motion was the motion of the damper body,  $y$ .

The actuator provided the input motion of the damper. The dynamometer created a sinusoidal displacement profile that matches the user defined test parameters. For these experiments, the displacement amplitude was defined and the peak velocity of the cycle was also defined. These two parameters combine to determine the frequency of the experiment. The frequency can be derived as shown in,

$$y(t) = Y_o * \sin(2\pi ft), \quad (5.1)$$

$$\dot{y}(t) = Y_o 2\pi f * \cos(2\pi ft), \quad (5.2)$$

$$V_p = Y_o 2\pi f, \quad (5.3)$$

$$f = \frac{V_p}{Y_o 2\pi}, \quad (5.4)$$

where  $y(t)$  is the dynamometer displacement profile,  $Y_o$  is the displacement amplitude,  $f$  is the frequency of the sinusoidal motion,  $\dot{y}(t)$  is the dynamometer velocity profile,  $V_p$  is the peak velocity of the dynamometer, which is equal to the velocity amplitude. This shows the derivation of how to simply relate the input parameters to the frequency of the dynamometer oscillations.



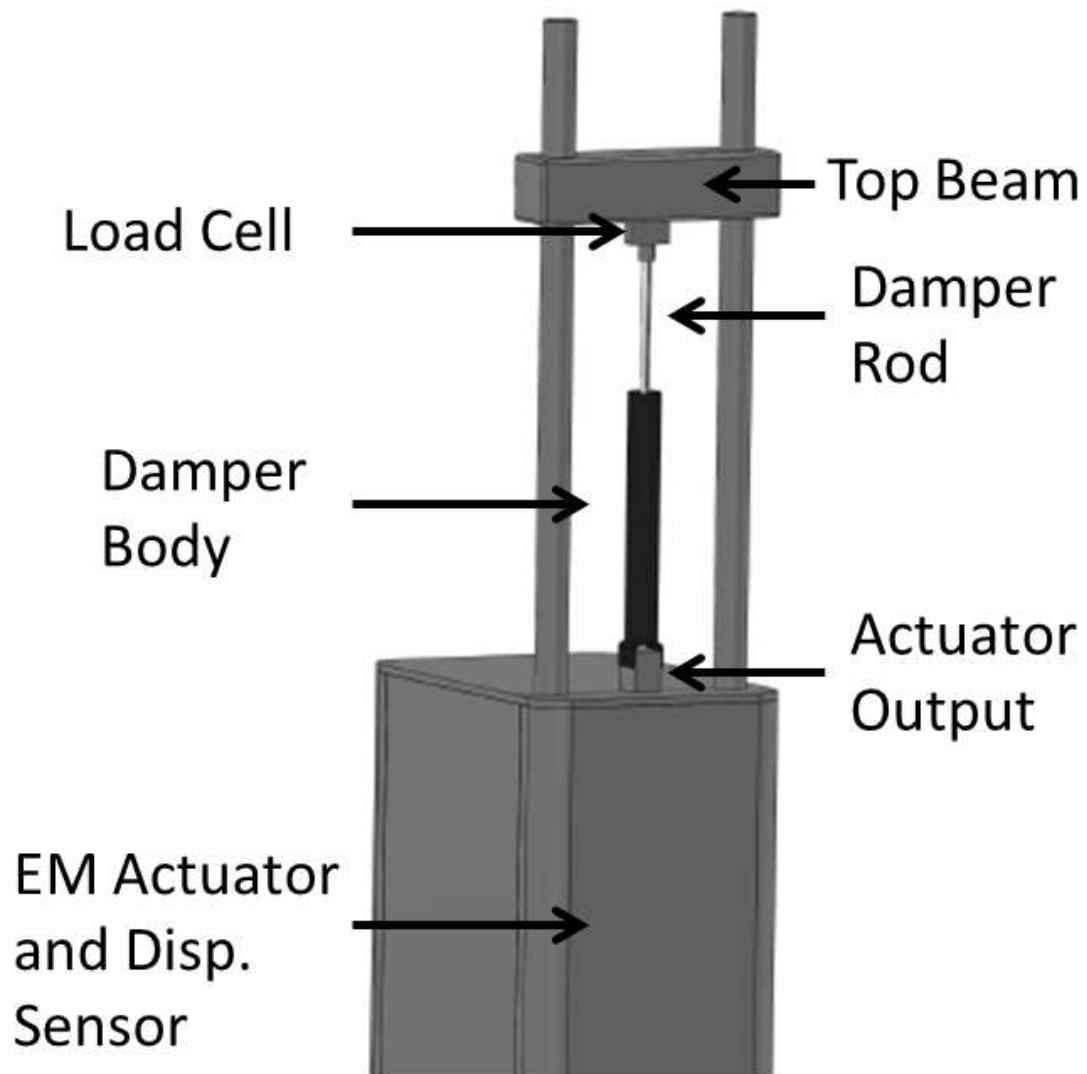


Figure 5.1: Damper dynamometer.

There are 3 main plots used to analyze the output data from these experiments: force vs. velocity plot, force vs. displacement plot, and peak force vs. peak velocity. The force vs. velocity plot is the characteristic plot for a damper. For simple spring mass damper systems, the damper force is modeled as a constant times the velocity. The result of that simple expression would be shown in a force vs. velocity plot. That is why this is the characteristic plot for the damper. Figure 5.2 shows an example of a typical force vs. velocity plot. This plot shows how the damper response is different in compression or negative force, and extension or positive force.

The force vs. displacement curve of the damper gives another way to look at the fit of the

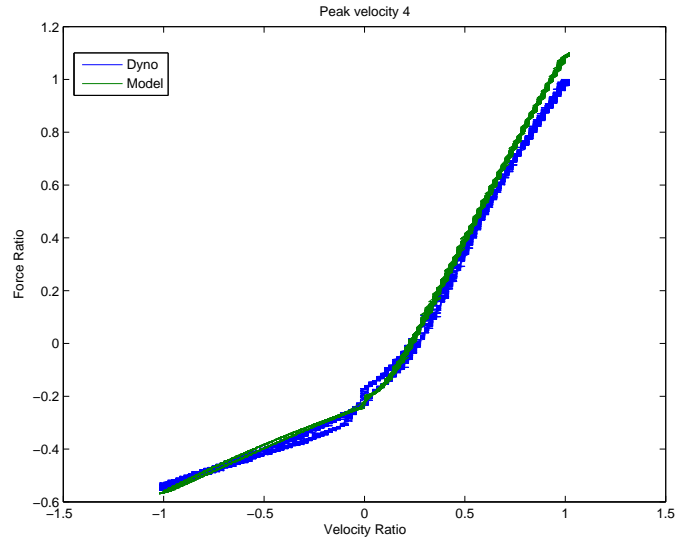


Figure 5.2: Example force vs. velocity plot.

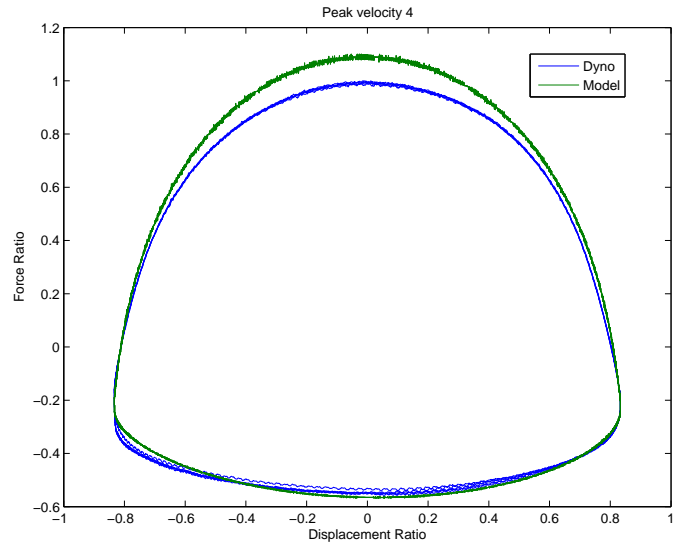


Figure 5.3: Example force vs. displacement plot.

data. Figure 5.3 is an example force vs. displacement plot. The force vs. velocity plots gives a good look at the low velocity, thus high displacement, results. The force vs. displacement plot gives an expanded view of the low displacement, thus high velocity, results. These two plots are useful in looking at the overall qualitative fit of the model.

The peak force vs. peak velocity plot is very useful for comparing the overall frequency dependent response of the damper. An example of the peak force vs. peak velocity plot is

shown in Figure 5.4. This shows the maximum damping force in compression and extension over a range of input frequencies.

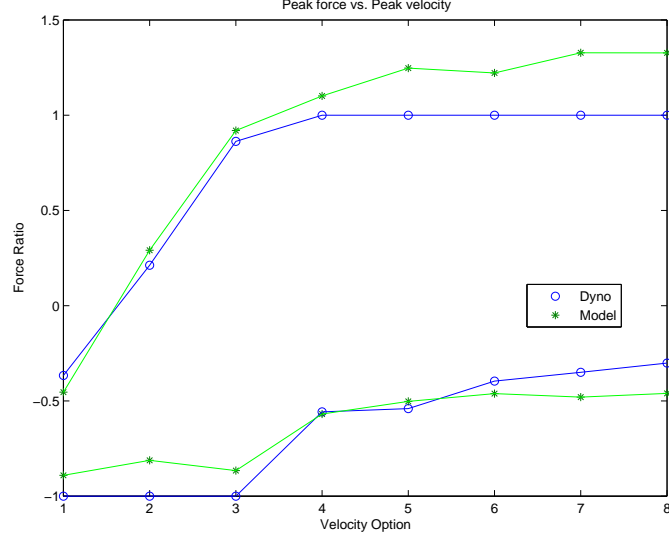


Figure 5.4: Peak force vs. peak velocity plot for the model validation.

## 5.2 Model and Experimental Results

The model is compared to the experiment in 4 main ways: the 3 plots listed in Section 5.1 and a root-mean-square (RMS) error. The plots are described in Section 5.1, so the RMS error will be explained here. The RMS error,  $E_{RMS}$ , is expressed as,

$$E_{RMS} = \sqrt{\frac{1}{N} \sum_{i=1}^N (F_{mi} - F_{di})^2}, \quad (5.5)$$

where  $N$  is the number of points used for the calculation,  $i$  is the incrementing variable for each point in the data sets,  $F_{mi}$  is the damper rod force,  $F_1$ , from the model at each time step, and  $F_{di}$  is the damper rod force from the dynamometer experiments. This is the quantitative measure used to fully validate the model.

This study was performed as part of a collaboration with Honda. The goal was a minimum of 80% accuracy, or a maximum of 20% error. This goal was based on the large range of frequencies used in the study. Table 5.1 is the RMS error between the experimental and the model results. This table shows that the maximum error is less than 20 percent. The model was validated over a range of frequencies on the order of 0.1 Hz to 10 Hz. This large range of input frequencies created a situation where a larger error can be accepted for a valid model. The results in Table 5.1 show that the model successfully predicts the response of the

damper. As mentioned above, plots are a useful way to analyze the results. Figures 5.5-5.12 show the force vs. velocity and force vs. displacement plots for each of the peak velocity options. These plots actually show the fit of the model in compression AND tension. The force vs. velocity plot in Figure 5.5 shows that the model predicts a force magnitude that is too low in compression and extension. The plot for each peak velocity can be analyzed.

These 8 sets of plots can become cumbersome. Therefore the peak force vs. peak velocity plot was used to summarize the damper response across a group of frequencies. Figure 5.13 gives the peak force vs. peak velocity plot with both the experimental data and the model results. This plot adds significant information that is not shown in Table 5.1. The peak force vs. peak velocity plots show which part of the damper response is causing the error shown in the RMS table. Looking at peak velocity option 5 in Figure 5.13, the model predicts the force magnitude too large in extension, but too small in compression. This type of analysis was used at all peak velocities.

Table 5.1: RMS error for the model validation.

Peak Velocity Option	RMS Error (%)
1	9.25
2	9.14
3	7.53
4	4.74
5	12.43
6	14.19
7	18.60
8	19.93

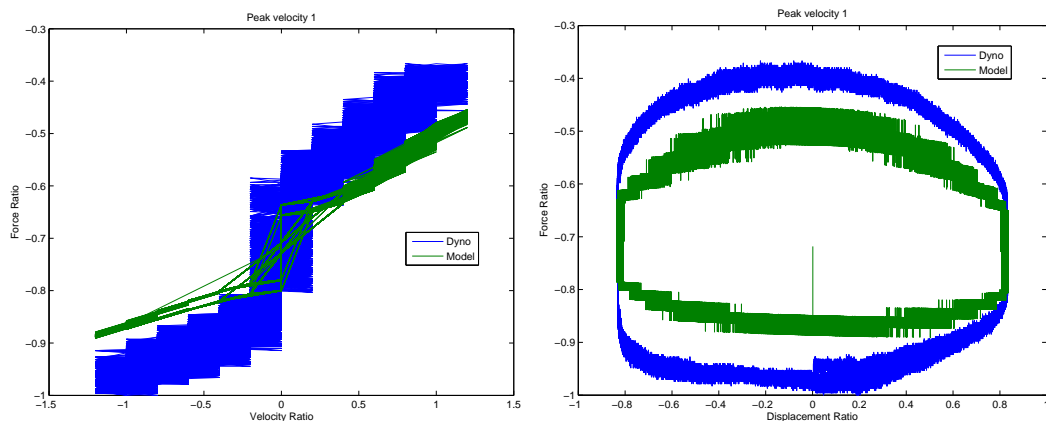


Figure 5.5: Damper response at peak velocity 1.

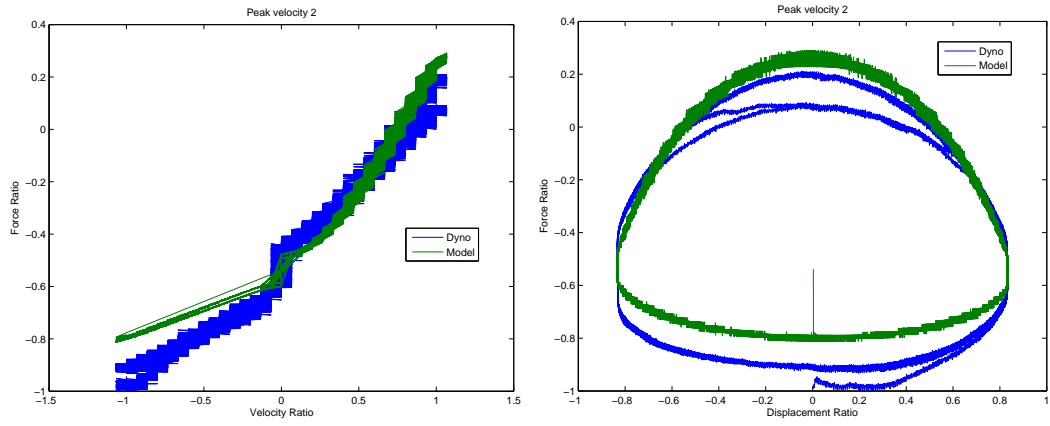


Figure 5.6: Damper response at peak velocity 2.

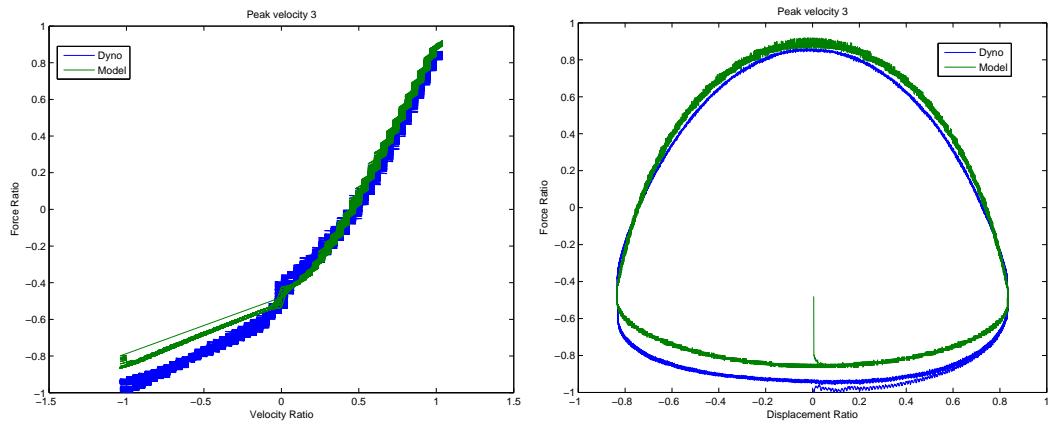


Figure 5.7: Damper response at peak velocity 3.

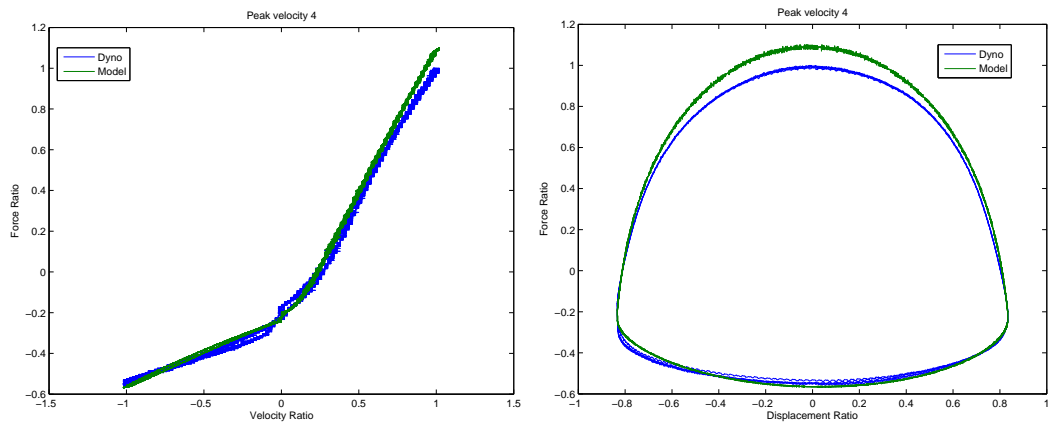


Figure 5.8: Damper response at peak velocity 4.

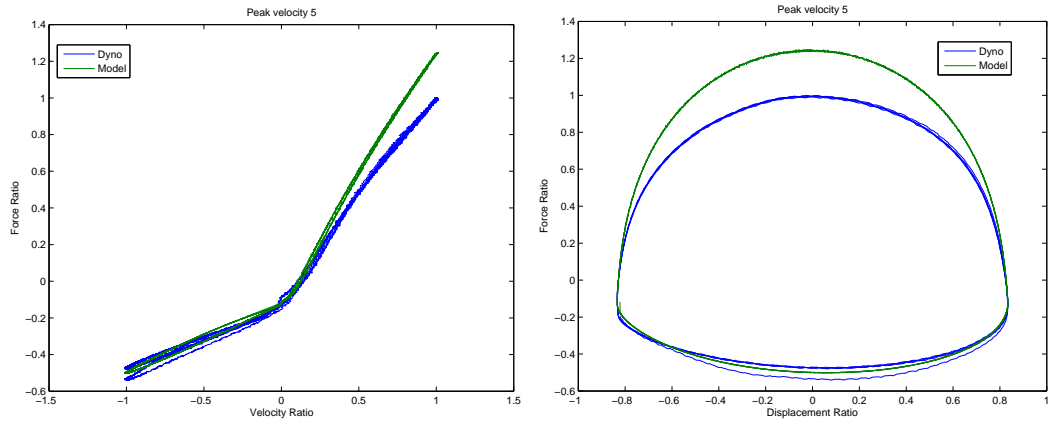


Figure 5.9: Damper response at peak velocity 5.

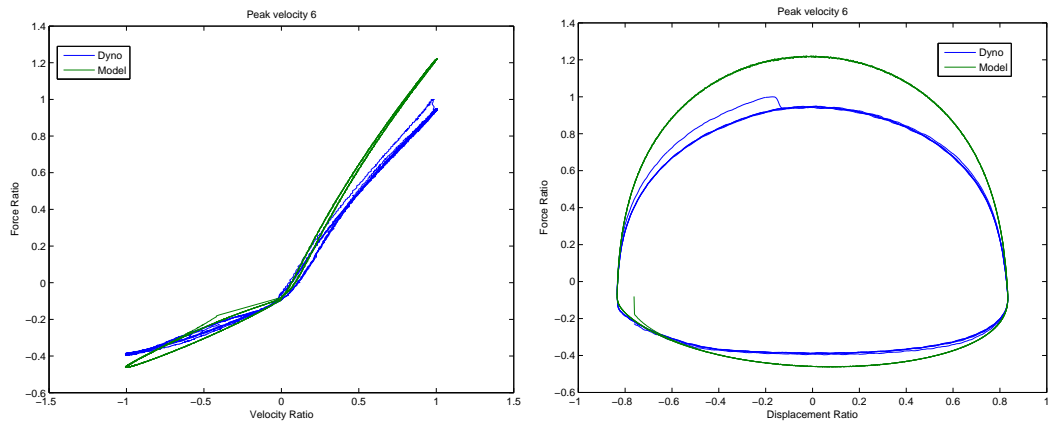


Figure 5.10: Damper response at peak velocity 6.

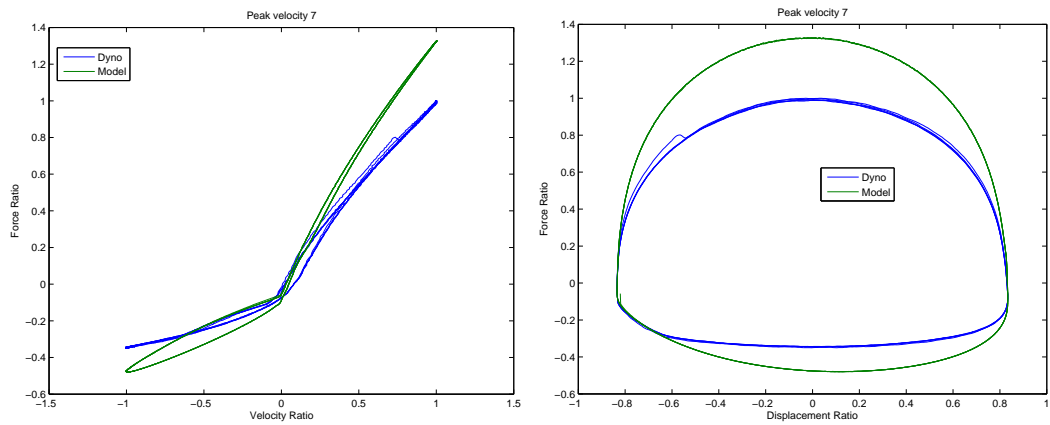


Figure 5.11: Damper response at peak velocity 7.

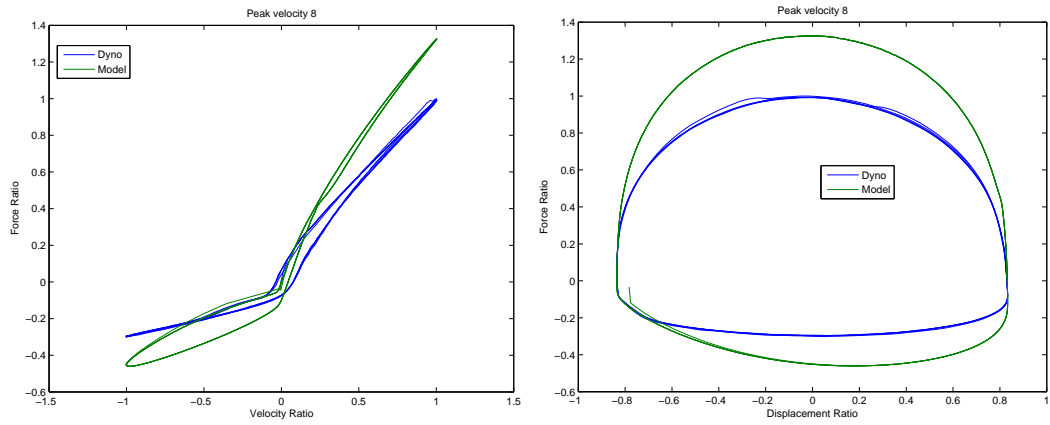


Figure 5.12: Damper response at peak velocity 8.

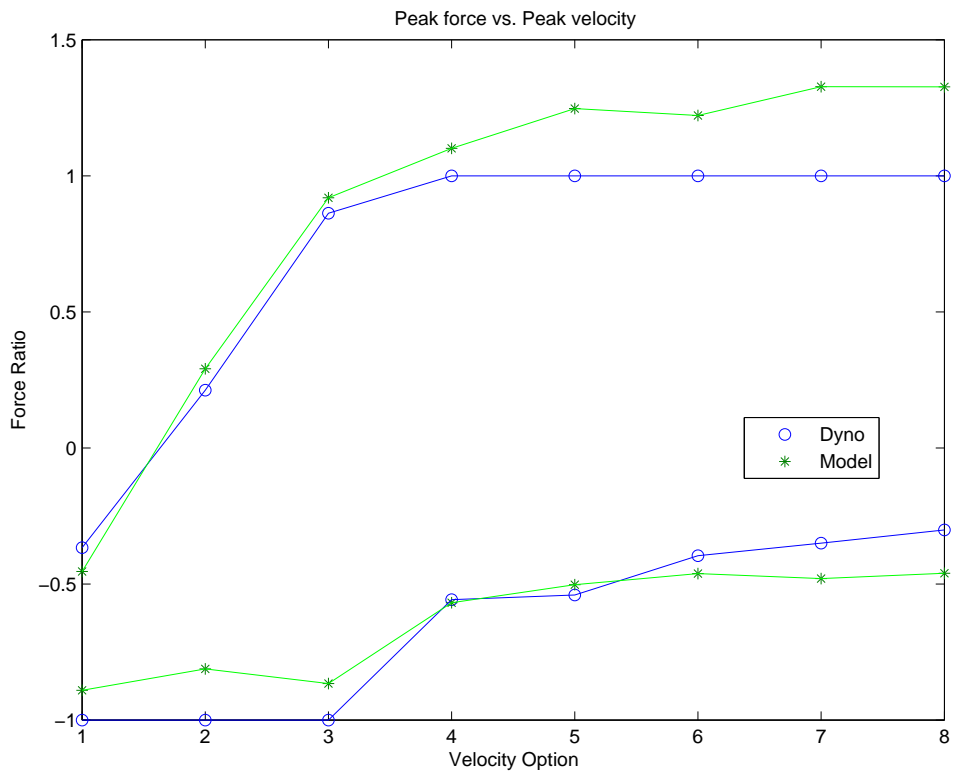


Figure 5.13: Peak force vs. peak velocity plot for the model validation.

## Chapter 6: Damper Model Sensitivity Study

The model was validated for a number of experiments, which showed that the model could adequately predict the response of the damper. The next step was to see what insight the model can give about variations of this damper. The input parameters for the model, described in Chapter 2, were measured or defined for a real damper. The parameters were chosen from the physical properties of the damper or fluids, and a full list of the parameters is shown in Table 6.1. The effects of the parameters are broken up based on the peak force in 4 cases: low speed extension, high speed extension, low speed compression, and high speed compression. For each of these cases, the top parameters are described with plots showing the changes and an explanation based on the equations and a practical analysis of the system. The low speeds are peak velocities 1 through 4 and the high speeds are peak velocities 5 through 8.

The sensitivity of the model to each parameter is defined as,

$$Sensitivity(X_o) = \left| \frac{DF_{X_o}(150\%) - DF_{X_o}(50\%)}{DF_{X_o}(100\%)} \right| * 100\%, \quad (6.1)$$

where  $Sensitivity(X_o)$  is the sensitivity of the model to a parameter  $X_o$ ,  $X_o$  is the parameter being varied,  $DF_{X_o}(150\%)$  is the peak force for the 150% case of parameter  $X_o$ ,  $DF_{X_o}(50\%)$  is the peak force for the 50% case of parameter  $X_o$ , and  $DF_{X_o}(100\%)$  is the peak force for the baseline model case.

### 6.1 Parameter Refinement

The parameters listed in Table 6.1 are the important parameters in the model that can be reasonably varied. The listed parameters have some overlap, where multiple parameters do roughly the same thing, so some of these parameters can be eliminated. There are 3 main sets of variables that overlap: check valve parameters, bleed orifice parameters, and discharge coefficients. The equation for the piston check valve for the compression chamber is written as,

$$q_{12} = 0 \quad P_1 \geq P_2 \quad (6.2)$$

$$q_{12} = -C_{d12} \pi D_{v12} \frac{|P_1 - P_2| A_{f12} n_{12}}{K_1} \sqrt{\frac{2 |P_1 - P_2|}{\rho}} \quad P_1 < P_2. \quad (6.3)$$

where  $C_{d12}$  is the discharge coefficient for flow  $q_{12}$ ,  $D_{v12}$  is the diameter of the orifices for flow  $q_{12}$  about the centerline of the damper,  $A_{f12}$  is the flow area of a single orifice for flow  $q_{12}$ ,  $n_{12}$  is the number of individual orifices for flow  $q_{12}$ ,  $K_1$  is the shim stiffness of the shim stack for flow  $q_{12}$  measured at a radius of  $D_{v12}/2$ . Of the parameters shown in (6.2) there are 4 parameters that have the same effect:  $D_{v12}$ ,  $A_{f12}$ ,  $n_{12}$ , and  $K_1$ .  $K_1$  has an inverse relationship with the other three, but they were summarized by just one variable since the resulting sensitivity has the same trend. This is true for the other 3 check valve equations



Table 6.1: Parameters varied for the sensitivity study.

Parameter	Description	Case 1	Baseline	Case 2
$m_{r,r}$	Mass of damper rod	$0.5 * m_{r,r}$	$m_{r,r}$	$1.5 * m_{r,r}$
$m_{b,r}$	Mass of damper body	$0.5 * m_{b,r}$	$m_{b,r}$	$1.5 * m_{b,r}$
$A_{p,r}$	Area of damper piston	$0.5 * A_{p,r}$	$A_{p,r}$	$1.5 * A_{p,r}$
$A_{r,r}$	Area of damper rod	$0.5 * A_{r,r}$	$A_{r,r}$	$1.5 * A_{r,r}$
$\beta_{1,r}, \beta_{2,r}, \beta_{31,r}$	Bulk modulus of oil	$0.5 * \beta_{1,r}$	$\beta_{1,r}$	$1.5 * \beta_{1,r}$
$\beta_{32,r}$	Bulk modulus of gas	$0.5 * \beta_{32,r}$	$\beta_{32,r}$	$1.5 * \beta_{32,r}$
$L_{1,r}$	Length of chamber 1	$0.5 * L_{1,r}$	$L_{1,r}$	$1.5 * L_{1,r}$
$L_{2,r}$	Length of chamber 2	$0.5 * L_{2,r}$	$L_{2,r}$	$1.5 * L_{2,r}$
$V_{32o,r}$	Initial volume of gas in chamber 3	$0.5 * V_{32o,r}$	$V_{32o,r}$	$1.5 * V_{32o,r}$
$V_{3o,r}$	Total volume in chamber 3	$0.5 * V_{3o,r}$	$V_{3o,r}$	$1.5 * V_{3o,r}$
$\rho_r$	Density of oil	$0.5 * \rho_r$	$\rho_r$	$1.5 * \rho_r$
$K_{1,r}$	Shim stiffness for flow q12	$0.5 * K_{1,r}$	$K_{1,r}$	$1.5 * K_{1,r}$
$K_{2,r}$	Shim stiffness for flow q22	$0.5 * K_{2,r}$	$K_{2,r}$	$1.5 * K_{2,r}$
$K_{3,r}$	Shim stiffness for flow q32	$0.5 * K_{3,r}$	$K_{3,r}$	$1.5 * K_{3,r}$
$K_{4,r}$	Shim stiffness for flow q42	$0.5 * K_{4,r}$	$K_{4,r}$	$1.5 * K_{4,r}$
$A_{11,r}$	Piston bleed orifice area	$0.5 * A_{11,r}$	$A_{11,r}$	$1.5 * A_{11,r}$
$A_{31,r}$	Fixed bleed orifice area	$0.5 * A_{31,r}$	$A_{31,r}$	$1.5 * A_{31,r}$
$A_{12,r}$	Orifice area for flow q12	$0.5 * A_{12,r}$	$A_{12,r}$	$1.5 * A_{12,r}$
$A_{22,r}$	Orifice area for flow q22	$0.5 * A_{22,r}$	$A_{22,r}$	$1.5 * A_{22,r}$
$A_{32,r}$	Orifice area for flow q32	$0.5 * A_{32,r}$	$A_{32,r}$	$1.5 * A_{32,r}$
$A_{42,r}$	Orifice area for flow q42	$0.5 * A_{42,r}$	$A_{42,r}$	$1.5 * A_{42,r}$
$D_{v12,r}$	Loading diameter for flow q12	$0.5 * D_{v12,r}$	$D_{v12,r}$	$1.5 * D_{v12,r}$
$D_{v22,r}$	Loading diameter for flow q22	$0.5 * D_{v22,r}$	$D_{v22,r}$	$1.5 * D_{v22,r}$
$D_{v32,r}$	Loading diameter for flow q32	$0.5 * D_{v32,r}$	$D_{v32,r}$	$1.5 * D_{v32,r}$
$D_{v42,r}$	Loading diameter for flow q42	$0.5 * D_{v42,r}$	$D_{v42,r}$	$1.5 * D_{v42,r}$
$F_{r,r}$	Coulomb Friction	$0.5 * F_{r,r}$	$F_{r,r}$	$1.5 * F_{r,r}$
$C_{d11}$	Discharge coefficient for flow q11	0.65	0.6	0.7
$C_{d31}$	Discharge coefficient for flow q31	0.65	0.6	0.7
$C_{d12}$	Discharge coefficient for flow q12	0.6	0.7	0.65
$C_{d22}$	Discharge coefficient for flow q22	0.6	0.7	0.65
$C_{d32}$	Discharge coefficient for flow q32	0.6	0.7	0.65
$C_{d42}$	Discharge coefficient for flow q42	0.6	0.7	0.65
$n_{11}$	Number of orifices for flow q11	$0.5 * n_{11}$	$n_{11}$	$1.5 * n_{11}$
$n_{31}$	Number of orifices for flow q31	$0.5 * n_{31}$	$n_{31}$	$1.5 * n_{31}$
$n_{12}$	Number of orifices for flow q12	$0.5 * n_{12}$	$n_{12}$	$1.5 * n_{12}$
$n_{22}$	Number of orifices for flow q22	$0.5 * n_{22}$	$n_{22}$	$1.5 * n_{22}$
$n_{32}$	Number of orifices for flow q32	$0.5 * n_{32}$	$n_{32}$	$1.5 * n_{32}$
$n_{42}$	Number of orifices for flow q42	$0.5 * n_{42}$	$n_{42}$	$1.5 * n_{42}$

also. Therefore  $K_1$ ,  $K_2$ ,  $K_3$ , and  $K_4$ , were used and  $D_{v12}$ ,  $A_{f12}$ ,  $n_{12}$ ,  $D_{v22}$ ,  $A_{f22}$ ,  $n_{22}$ ,  $D_{v32}$ ,  $A_{f32}$ ,  $n_{32}$ ,  $D_{v42}$ ,  $A_{f42}$ , and  $n_{42}$  were eliminated from the study.

The piston bleed valve flow is defined as,

$$q_{11} = C_{d11} A_{11} n_{11} \text{sgn}(P_1 - P_2) \sqrt{\frac{2|P_1 - P_2|}{\rho}}, \quad (6.4)$$

where  $C_{d11}$  is the discharge coefficient for the flow through the piston bleed orifice,  $A_{11}$  is the flow area for a single orifice in the piston bleed orifice,  $n_{11}$  is the number of individual orifices for flow  $q_{11}$ ,  $P_1$  and  $P_2$  are the pressures in the rebound and compression chambers respectively.  $A_{11}$  and  $n_{11}$  have the same effects on the equation. Therefore the model sensitivity is the same for each variable. The equation for the fixed bleed valve, (2.11), uses the same form. Therefore  $A_{11}$  and  $A_{31}$  were used and  $n_{11}$  and  $n_{31}$  were eliminated from the study. The discharge coefficients are shown in Equations 6.2 and 6.4. The full sensitivity study contained 6 total discharge coefficients, one for each valve. However, varying both bleed orifice valves together makes sense, due to the similar shape of the orifices. The check valve discharge coefficients were also varied together due to the similar shape and operation. Therefore,  $C_{d11}$  and  $C_{d12}$  were used and  $C_{d31}$ ,  $C_{d12}$ ,  $C_{d32}$ , and  $C_{d42}$  were eliminated from the study.

The relations listed above eliminated 18 of the 38 total parameters in the study, so the final results only have 20 parameters. The refined number of variables make the results much easier to present and analyze.

## 6.2 Sensitivity Study Results

Limiting the study to only 20 parameters allowed for the results from each case to be summarized in a simple plot. Figures 6.1-6.4 show the resulting sensitivity from the model for each case. These figures are used to rank the effect of each parameter for each case. The most important parameters for each case will be analyzed in Section 6.3 to Section 6.6.

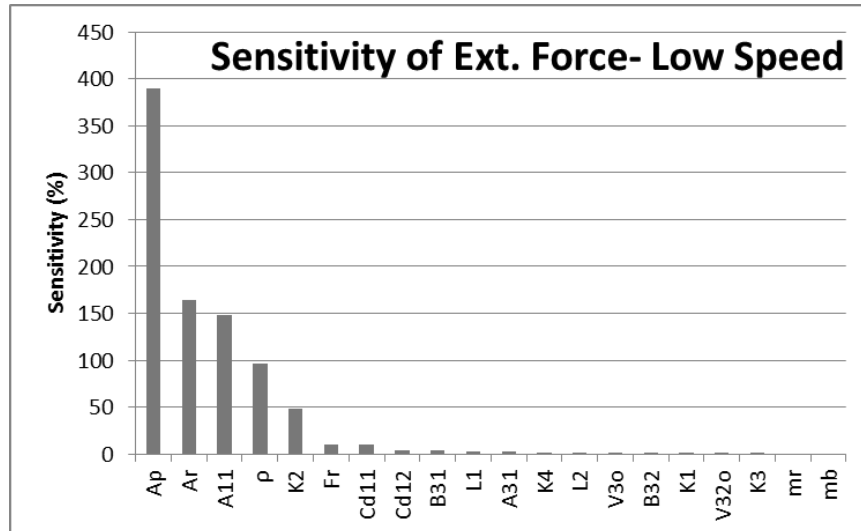


Figure 6.1: Sensitivity results for low speed extension.

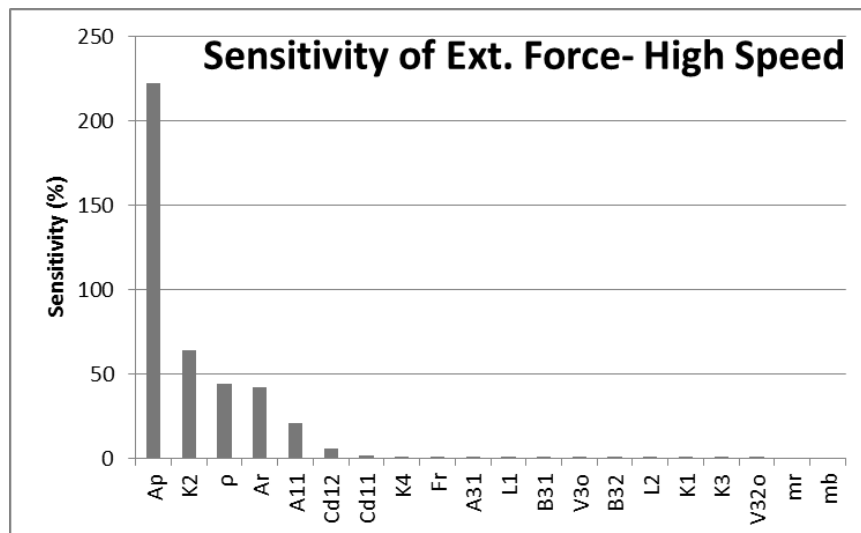


Figure 6.2: Sensitivity results for high speed extension.

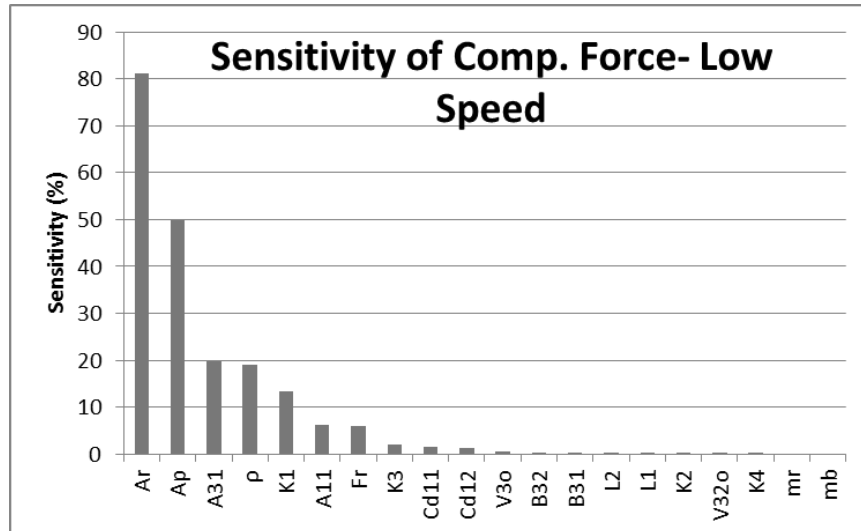


Figure 6.3: Sensitivity results for low speed compression.

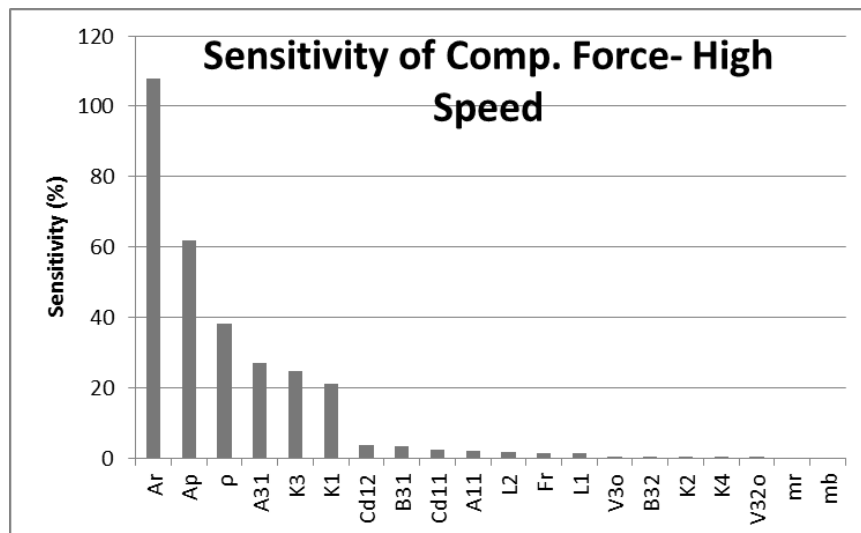


Figure 6.4: Sensitivity results for high speed compression.

## 6.3 Sensitivity Low Speed Extension Results

Figure 6.1 shows the sensitivity results ranked from largest effect to smallest. The top ten parameters are given in Table 6.2. The parameters in this table with a sensitivity greater than 10% were analyzed to show the model results and look at the equations to explain the model dependence on the parameter. The results were shown for the remaining parameters.

Table 6.2: Top ten parameters for low speed extension sensitivity.

Rank	Parameter	Sensitivity (%)
1	$A_p$	389.2
2	$A_r$	164.7
3	$A_{11}$	147.8
4	$\rho$	96.0
5	$K_2$	48.3
6	$F_r$	10.4
7	$C_{d11}$	10.0
8	$C_{d12}$	3.7
9	$B_{31}$	3.5
10	$L_1$	2.9

### 6.3.1 Piston Area Sensitivity

The piston area has the largest effect of the parameters. The resulting force vs. velocity plots for velocity options 3 and 8 are given in Figure 6.5. The peak force vs. peak velocity plot in Figure 6.6 shows that increasing the piston area increases the peak damper force in both extension and compression. The most relevant equation for  $A_p$  is the damper rod equation which is written as,

$$F_1 = m_r \ddot{x} - P_2 A_p + P_1 (A_p - A_r) + F_r \operatorname{sgn}(\dot{z}). \quad (6.5)$$

In this equation, if  $A_p$  is increased, the rebound chamber pressure,  $P_1$ , and the compression chamber pressure,  $P_2$ , will both be effectively increased. Since  $P_1$  is scaled by  $A_p - A_r$ , an increase in  $A_p$  has a larger effect on  $P_1$  than  $P_2$ , which is scaled by  $A_p$  only. Therefore, an increase in  $A_p$  will cause the force magnitude to be higher in extension and higher in compression (more negative). Since  $A_p$  has a larger effect on  $P_1$ , the extension force increases much more than the compression force magnitude does, as shown in the Figure 6.5. The flow continuity in the rebound is given as,

$$\dot{z}(A_p - A_r) = q_{11} + q_{12} + q_{22} + q_{\beta_1}. \quad (6.6)$$

$A_p$  has less of an effect here than in the damper rod force equation, but it does effect this portion of the damper. The piston displacement and velocity did not change, only  $A_p$  changed, which affects the flow due to the damper motion. Equation (6.6) is an example of where this effect occurs. An increase in the piston area creates a larger flow on the left-hand side of the equation, which creates a larger pressure in the rebound chamber,  $P_1$ , to allow the fluid compression and orifice flows to account for this extra flow. The same is true for the compression chamber flow continuity equation.

The effect of  $A_p$  in the equations makes sense practically since increasing  $A_p$  increases the loading area on the piston for both  $P_1$  and  $P_2$ . Also since the flow conservation equation shows an increase in flow for an increase in  $A_p$ , the pressures will be the same or greater than at the baseline  $A_p$ . Therefore, equal or greater pressures will occur and the area increases, so the force due to pressure will increase.

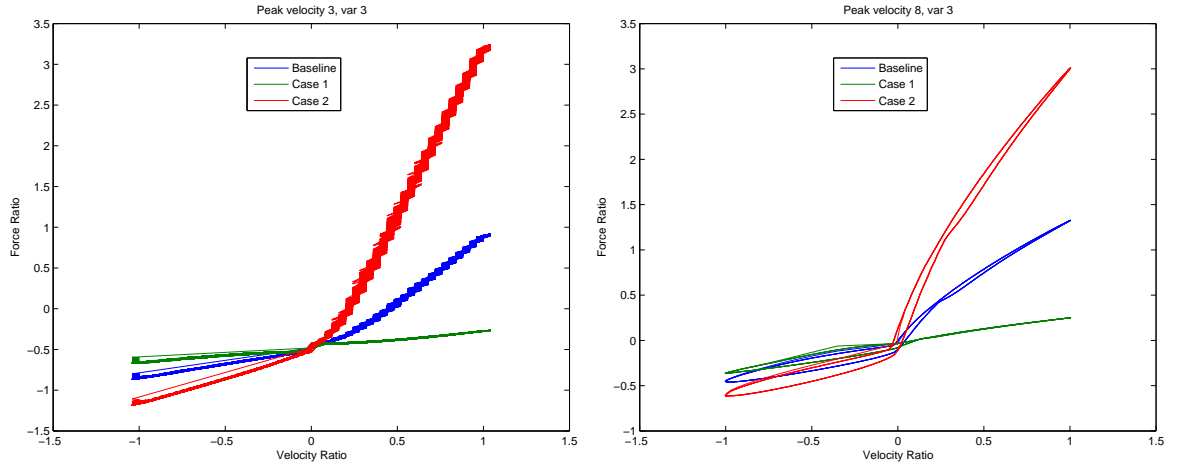


Figure 6.5: Force vs. velocity results for the model sensitivity to  $A_p$ .

### 6.3.2 Damper Rod Area Sensitivity

The damper rod area has the second largest effect of the parameters on low speed extension. The resulting force vs. velocity plots for velocity options 3 and 8 are given in Figure 6.7. The peak force vs. peak velocity plot in Figure 6.8 shows that increasing the damper rod area decreases the force magnitude in extension and increases the force magnitude in compression. The most relevant equation for  $A_r$  is the damper rod equation which is written as,

$$F_1 = m_r \ddot{x} - P_2 A_p + P_1 (A_p - A_r) + F_r \operatorname{sgn}(\dot{z}). \quad (6.7)$$

In this equation, if  $A_r$  is increased, then  $P_1$  will be effectively decreased since  $P_1$  is scaled by  $A_p - A_r$ . This will cause the force magnitude to be lower in extension and higher in compression (more negative), as shown in the Figure 6.7. The effect of  $A_r$  in the equations makes sense practically since an increase in  $A_r$  would decrease the area of the piston that is subjected to  $P_1$ . Thus decreasing the effect of  $P_1$  on the force on the damper rod.

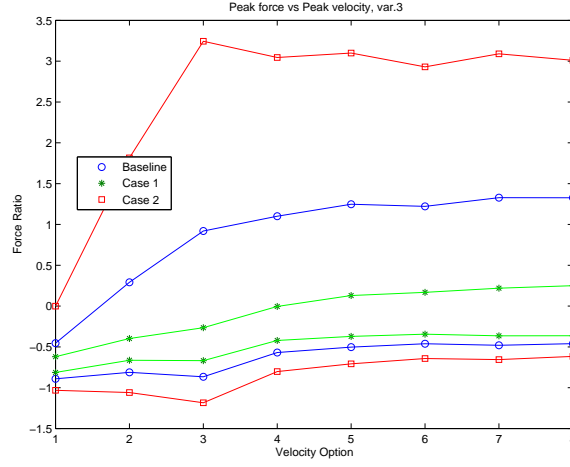


Figure 6.6: Peak force results for the model sensitivity to  $A_p$ .

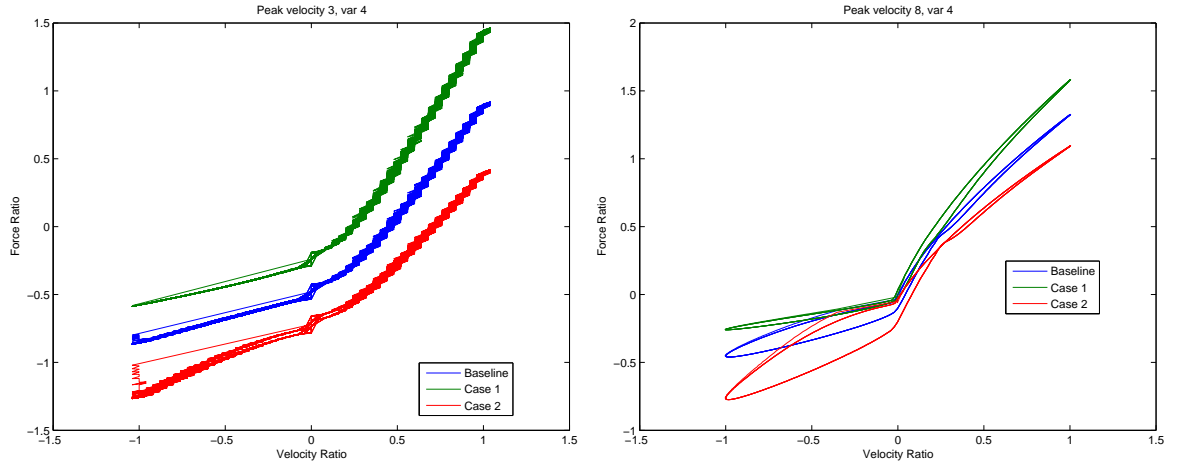


Figure 6.7: Force vs. velocity results for the model sensitivity to  $A_r$ .

### 6.3.3 Piston Bleed Orifice Area Sensitivity

The piston bleed orifice area has the third largest effect of the parameters on low speed extension. The resulting force vs. velocity plots for velocity options 3 and 8 are given in Figure 6.9. The peak force vs. peak velocity plot in Figure 6.10 shows that increasing the piston bleed orifice area decreases the peak damper force in extension and has almost no effect on the peak force in compression. The most relevant equation for  $A_{11}$  is the piston bleed orifice flow equation which is written as,

$$q_{11} = C_{d11} A_{11} n_{11} \text{sgn}(P_1 - P_2) \sqrt{\frac{2|P_1 - P_2|}{\rho}}. \quad (6.8)$$

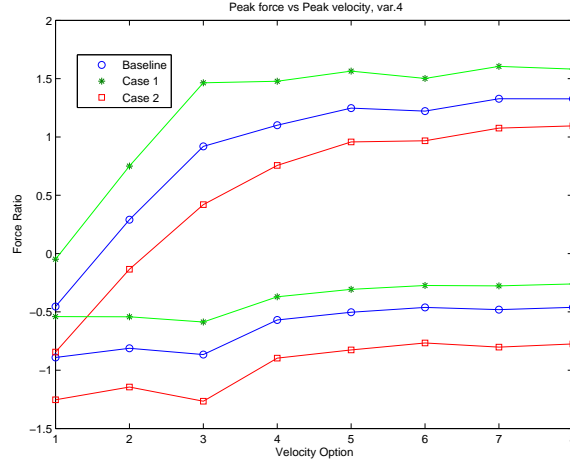


Figure 6.8: Peak force results for the model sensitivity to  $A_r$ .

The main effect of the piston bleed orifice area is on the flow caused by a given pressure differential. An increase in  $A_{11}$ , increases the flow caused by a given pressure differential. This will cause the force magnitude to be lower in extension and not change in compression, as shown in the Figure 6.9. The effect of  $A_{11}$  makes sense practically because an increase in the piston bleed orifice area decreases the pressure differential needed to cause the flow required to create an equilibrium between the rebound and compression chambers. The lower pressure differentials lead to lower forces based on the piston rod equation. The pressure differentials are lower at lower speeds, so the shim valves do not open much. This makes the bleed orifice most important at low speeds, which is why  $A_{11}$  has a larger effect than  $K_2$  for low speed extension.

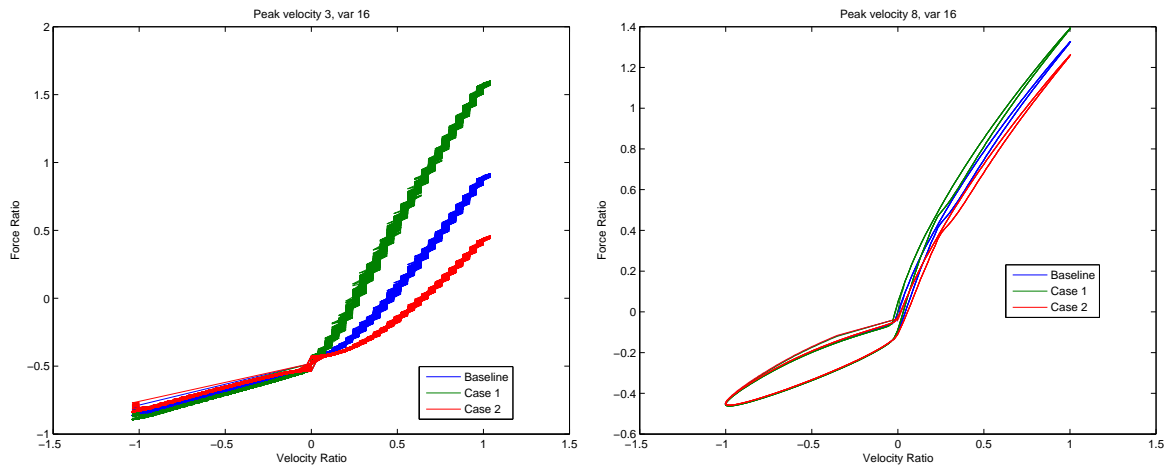


Figure 6.9: Force vs. velocity results for the model sensitivity to  $A_{11}$ .



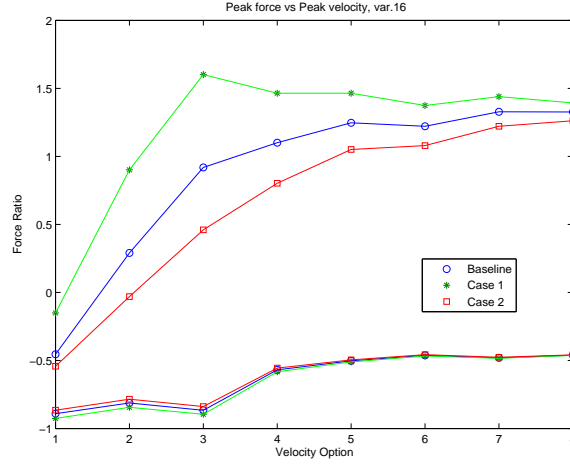


Figure 6.10: Peak force results for the model sensitivity to  $A_{11}$ .

### 6.3.4 Fluid Density Sensitivity

The fluid density area has the fourth largest effect of the parameters on low speed extension. The resulting force vs. velocity plots for velocity options 3 and 8 are given in Figure 6.11. The peak force vs. peak velocity plot in Figure 6.12 shows that increasing the fluid density increases the peak damper force in extension and increases the peak force in compression. The most relevant equation for  $\rho$  would be any of the flow equations. The piston bleed orifice flow equation is used as an example and is written as,

$$q_{11} = C_{d11} A_{11} n_{11} \text{sgn}(P_1 - P_2) \sqrt{\frac{2|P_1 - P_2|}{\rho}}, \quad (6.9)$$

The main effect of the fluid density is on the effective pressure differential seen by the orifice. An increase in fluid density decreases the pressure differential seen by an orifice. This will cause the force magnitude to be higher in extension and higher in compression (more negative), as shown in the Figure 6.11. The effect of  $\rho$  makes sense practically since an increase in fluid density would make it more difficult for the fluid to flow through the orifice. Thus increasing the pressure differential needed to create a flow compared to the baseline fluid density. The reason this effect is roughly constant for all speeds is that the fluid density affects all 6 flow equations equally, so it affects both the bleed orifice flows and shim valve flows.

### 6.3.5 Shim Stiffness for Flow $q_{22}$ Sensitivity

$K_2$ , the shim stiffness for flow  $q_{22}$ , has the fifth largest effect of the parameters on low speed extension. The resulting force vs. velocity plots for velocity options 3 and 8 are given in Figure 6.13. The peak force vs. peak velocity plot in Figure 6.14 shows that increasing  $K_2$

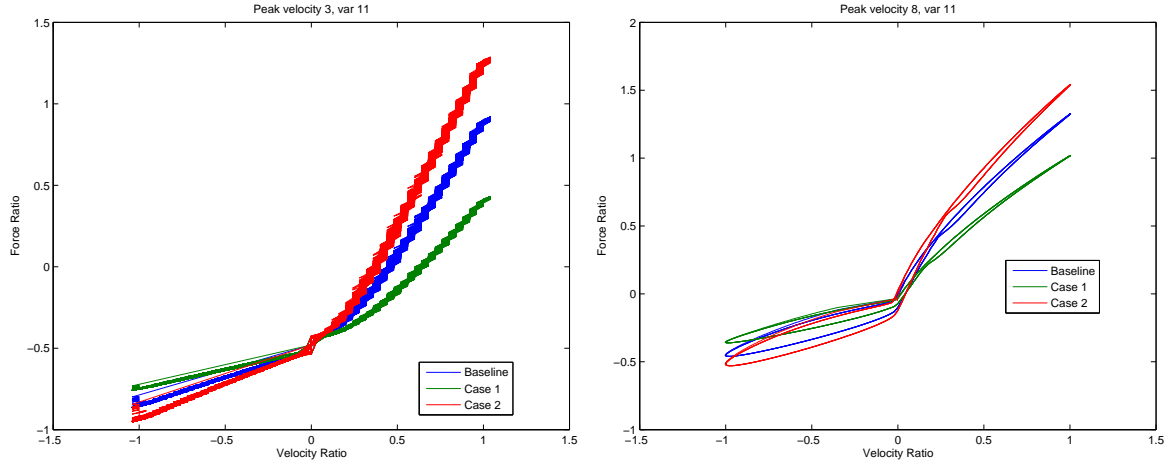


Figure 6.11: Force vs. velocity results for the model sensitivity to  $\rho$ .

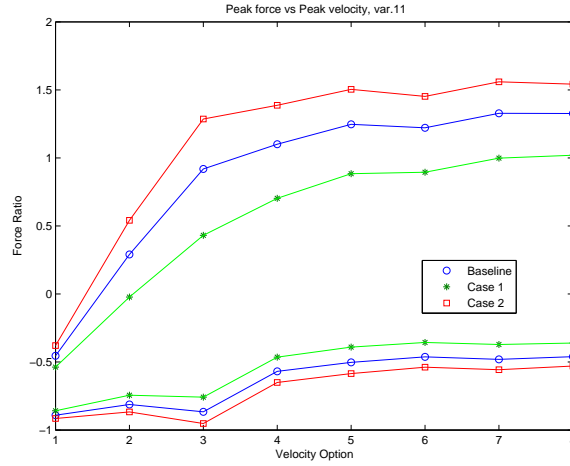


Figure 6.12: Peak force results for the model sensitivity to  $\rho$ .

increases the peak damper force in extension and has almost no effect on the peak force in compression. The most relevant equation for  $K_2$  is the piston check valve equation for flow  $q_{22}$ , which is written as,

$$q_{22} = 0 \quad P_1 \leq P_2 \quad (6.10)$$

$$q_{22} = C_{d22} \pi D_{v22} \frac{|P_1 - P_2| A_{f22} n_{22}}{K_2} \sqrt{\frac{2 |P_1 - P_2|}{\rho}} \quad P_1 > P_2, \quad (6.11)$$

where  $C_{d22}$  is the discharge coefficient for flow  $q_{22}$ ,  $D_{v22}$  is the diameter of the orifices for flow  $q_{22}$  about the centerline of the damper,  $A_{f22}$  is the flow area of a single orifice for flow  $q_{22}$ ,  $n_{22}$  is the number of individual orifices for flow  $q_{22}$ ,  $K_2$  is the shim stiffness of the shim

stack for flow  $q_{22}$  measured at a radius of  $D_{v22}/2$ .

The main effect of  $K_2$  is on the flow caused by a given pressure differential. An increase in  $K_2$  decreases the flow caused by a given pressure differential. This will cause the force magnitude to be higher in extension and not change in compression, as shown in the Figure 6.13. The effect of  $K_2$  makes sense practically because an increase in the piston rebound flow valve stiffness increases the pressure differential needed to cause the flow required to create an equilibrium between chambers 1 and 2. The higher pressure differentials lead to higher forces based on the piston rod equation. The pressure differentials are lower at low speeds, so the shim valves open less than the bleed valve flow areas. This makes the bleed orifice more important at low speeds, which is why  $K_2$  has a smaller effect than  $A_{11}$  for low speed extension.

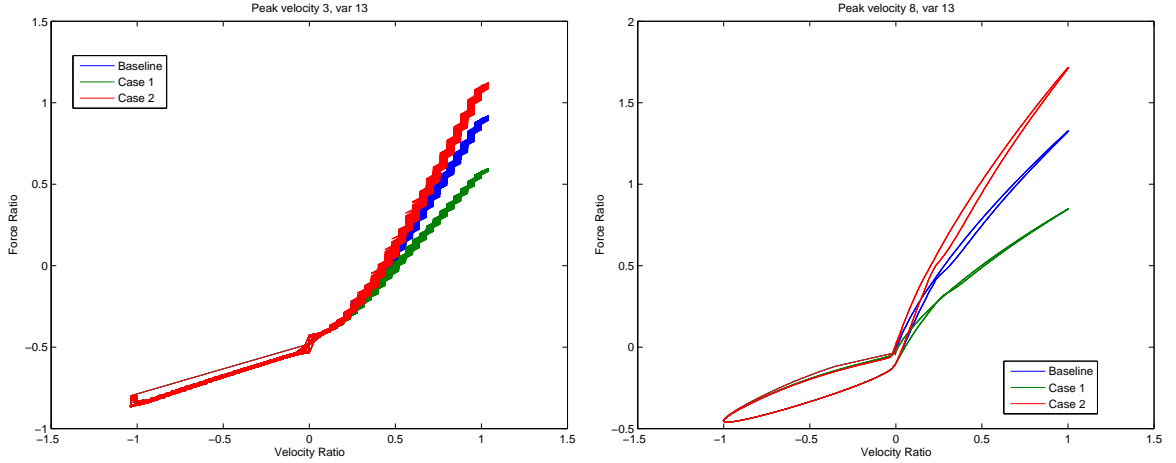


Figure 6.13: Force vs. velocity results for the model sensitivity to  $K_2$ .

### 6.3.6 Friction Force Amplitude Sensitivity

The amplitude of the friction force,  $F_r$ , has the sixth largest effect of the parameters on low speed extension. The resulting force vs. velocity plots for velocity options 3 and 8 are given in Figure 6.15. The peak force vs. peak velocity plot in Figure 6.16 shows that increasing the amplitude of the friction force increases the peak damper force in extension and increases the peak force in compression. The most relevant equation for  $F_r$  is the damper rod equation which is written as,

$$F_1 = m_r \ddot{x} - P_2 A_p + P_1 (A_p - A_r) + F_r \operatorname{sgn}(\dot{z}). \quad (6.12)$$

The main effect of the friction amplitude is directly on the damper forces. The friction is discretely added to the force if  $\dot{z}$  is positive, increasing the force magnitude in extension. The friction is discretely subtracted from the force if  $\dot{z}$  is negative, increasing the force magnitude in compression. Therefore an increase in  $F_r$ , increases force magnitude in extension and in

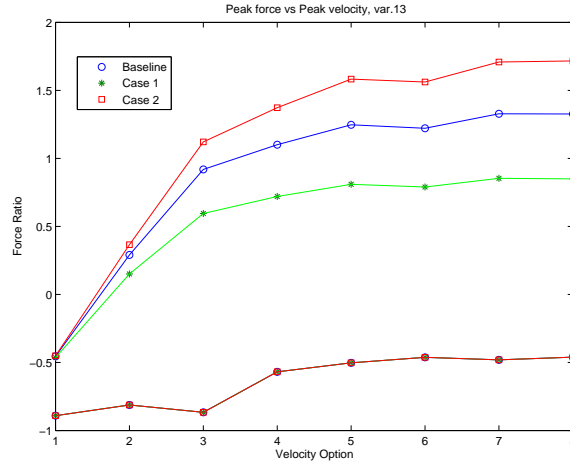


Figure 6.14: Peak force results for the model sensitivity to  $K_2$ .

compression, as shown in the Figure 6.15. The effect of  $F_r$  makes sense practically because the coulomb friction method used here is defined directly as a shift in damper force based on the direction of motion. This is the reason for the increase in both force amplitudes with an increase in  $F_r$ . The lower damper forces at low speeds is the reason that the friction has a larger relative effect at low speeds.

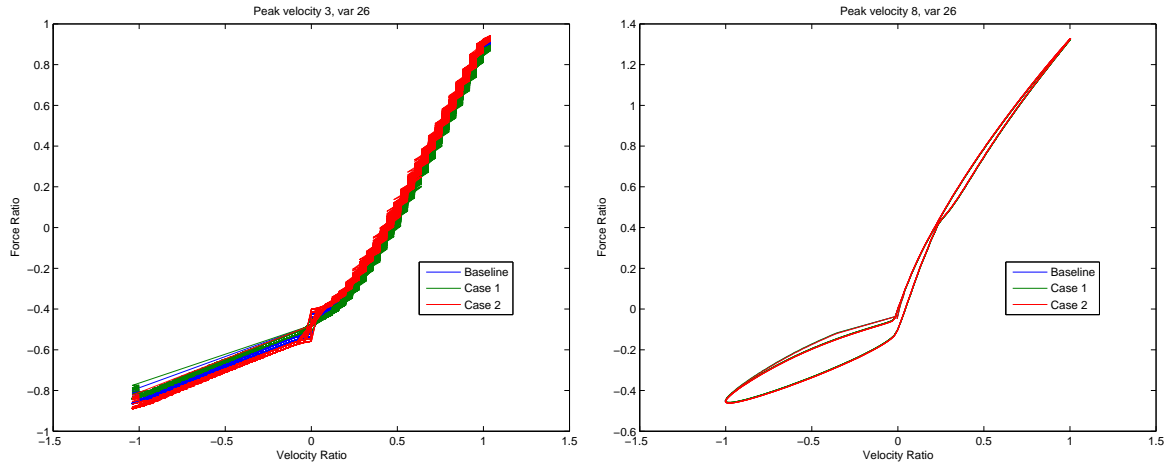


Figure 6.15: Force vs. velocity results for the model sensitivity to  $F_r$ .

### 6.3.7 Bleed Orifice Discharge Coefficient Sensitivity

The bleed orifice discharge coefficient has the seventh largest effect of the parameters on low speed extension. The resulting force vs. velocity plots for velocity options 3 and 8 are given

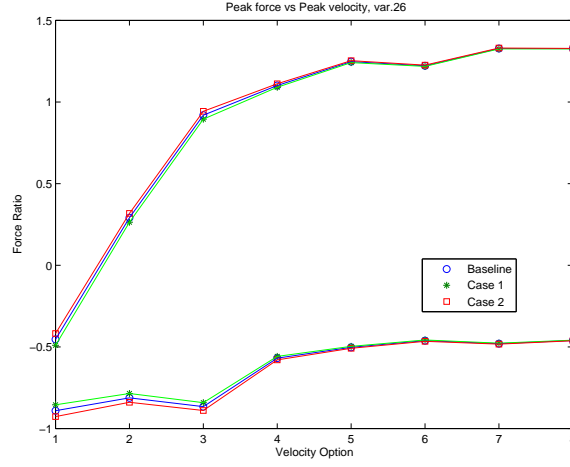


Figure 6.16: Peak force results for the model sensitivity to  $F_r$ .

in Figure 6.17. The peak force vs. peak velocity plot in Figure 6.18 shows that increasing the bleed orifice discharge coefficient decreases the peak damper force in extension and has almost no effect on the peak force in compression. The most relevant equation for  $C_{d11}$  is the piston bleed orifice flow equation which is written as,

$$q_{11} = C_{d11} A_{11} n_{11} \text{sgn}(P_1 - P_2) \sqrt{\frac{2|P_1 - P_2|}{\rho}}, \quad (6.13)$$

The main effect of the bleed orifice discharge coefficient is on the flow caused by a given pressure differential. An increase in  $C_{d11}$ , increases the flow caused by a given pressure differential. This will cause the force magnitude to be lower in extension and not change in compression, as shown in the Figure 6.17. The effect of  $C_{d11}$  makes sense practically because an increase in the piston bleed orifice decreases the pressure differential needed to cause the flow required to create an equilibrium between the rebound and compression chambers. The lower pressure differentials lead to lower forces based on the piston rod equation. The lower forces in compression limit the effects of  $C_{d11}$ .

### 6.3.8 Other Important Parameters

The rest of the top ten parameters for the low speed extension have less than a 10% sensitivity. Therefore they are not significant compared to the other options. The check valve discharge coefficient,  $C_{d12}$ , has the eighth largest effect of the parameters on low speed extension. The peak force vs. peak velocity plot in Figure 6.19 shows that increasing  $C_{d12}$  decreases the peak damper force in extension and has almost no effect on the peak force in compression. The fluid bulk modulus,  $\beta_{31}$ , has the ninth largest effect of the parameters on low speed extension. The peak force vs. peak velocity plot in Figure 6.20 shows that increasing  $\beta_{31}$  very slightly increases the peak damper force in extension and increases the

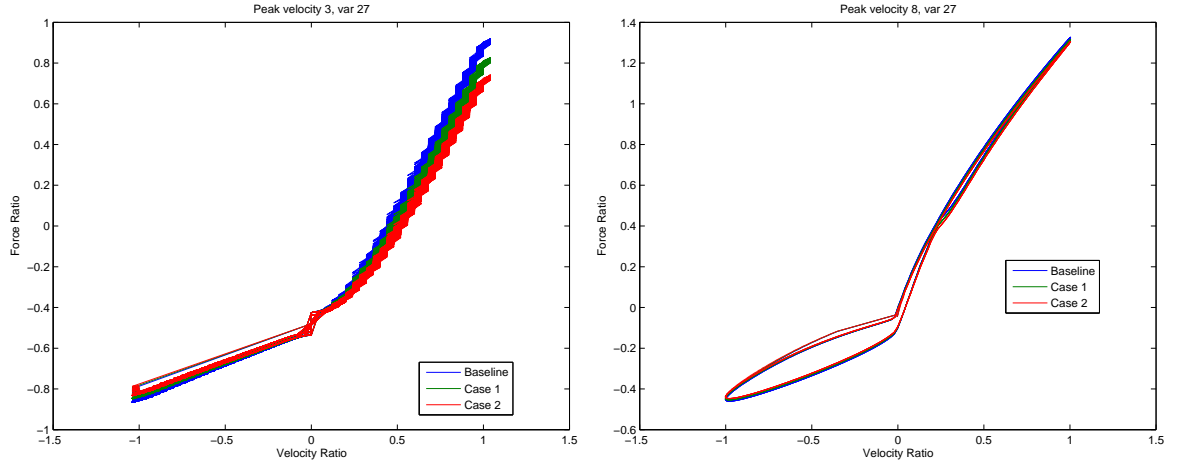


Figure 6.17: Force vs. velocity results for the model sensitivity to  $C_{d11}$ .

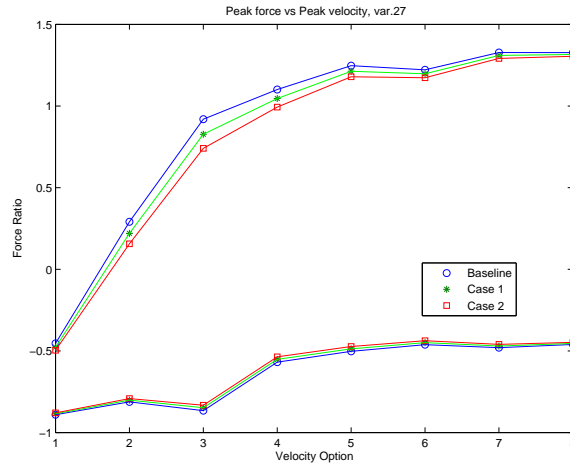


Figure 6.18: Peak force results for the model sensitivity to  $C_{d11}$ .

peak force magnitude in compression. The length of the reserve chamber,  $L_1$ , has the tenth largest effect of the parameters on low speed extension. The peak force vs. peak velocity plot in Figure 6.21 shows that increasing  $L_1$  very slightly decreases the peak damper force magnitude in both extension and compression.

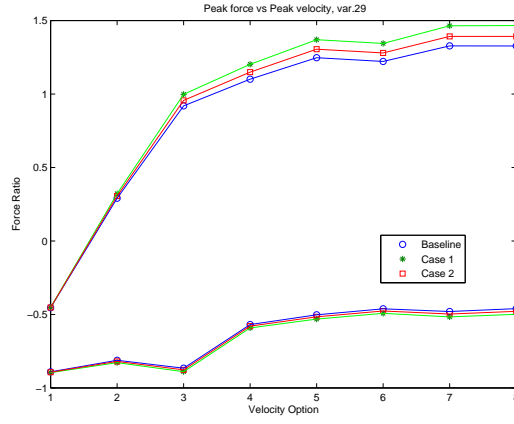


Figure 6.19: Peak force results for the model sensitivity to  $C_{d12}$ .

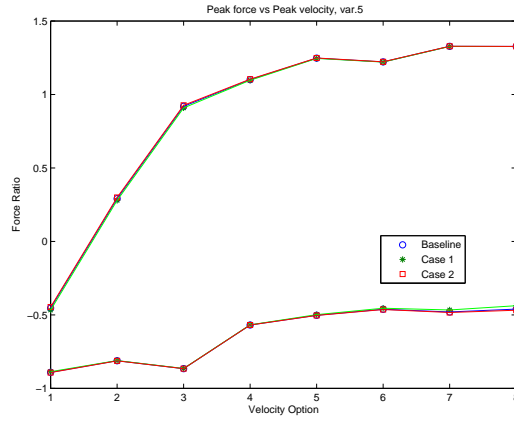


Figure 6.20: Peak force results for the model sensitivity to  $\beta_{31}$ .

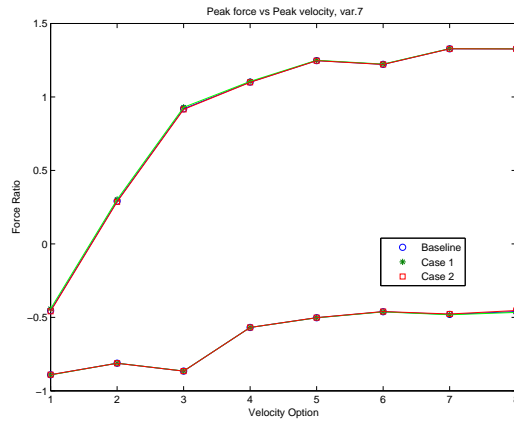


Figure 6.21: Peak force results for the model sensitivity to  $L_1$ .

## 6.4 Sensitivity High Speed Extension Results

Figure 6.2 shows the sensitivity results ranked from largest effect to smallest. The top ten parameters are given in Table 6.3. The parameters in this table with a sensitivity greater than 10% were analyzed to show the model results and look at the equations to explain the model dependence on the parameter. The results were shown for the remaining parameters.

Table 6.3: Top ten parameters for high speed extension sensitivity.

Rank	Parameter	Sensitivity (%)
1	$A_p$	222.1
2	$K_2$	63.7
3	$\rho$	44.2
4	$A_r$	42.3
5	$A_{11}$	20.9
6	$C_{d12}$	5.4
7	$C_{d11}$	1.7
8	$K_4$	1.1
9	$F_r$	0.6
10	$A_{31}$	0.2

### 6.4.1 Repeated Parameters With Significant Effects

Many of the parameters for high speed extension overlap with the variables in the low speed extension case.  $A_p$  has the largest effect on high speed extension and the effect is covered in Section 6.3.1.  $K_2$  has the second largest effect on high speed extension and the effect is covered in Section 6.3.5.  $\rho$  has the third largest effect on high speed extension and the effect is covered in Section 6.3.4.  $A_r$  has the fourth largest effect on high speed extension and the effect is covered in Section 6.3.2.  $A_{11}$  has the fifth largest effect on high speed extension and the effect is covered in Section 6.3.3.

### 6.4.2 Other Parameters

$C_{d12}$  has the sixth largest effect on high speed extension and the effect is shown in Figure 6.19.  $C_{d11}$  has the seventh largest effect on high speed extension and the effect is covered in Section 6.3.7.  $K_4$  has the eighth largest effect on high speed extension and the effect is shown in Figure 6.22.  $F_r$  has the ninth largest effect on high speed extension and the effect is covered in Section 6.3.6.  $A_{31}$  has the tenth largest effect on high speed extension and the effect is shown in Figure 6.23.



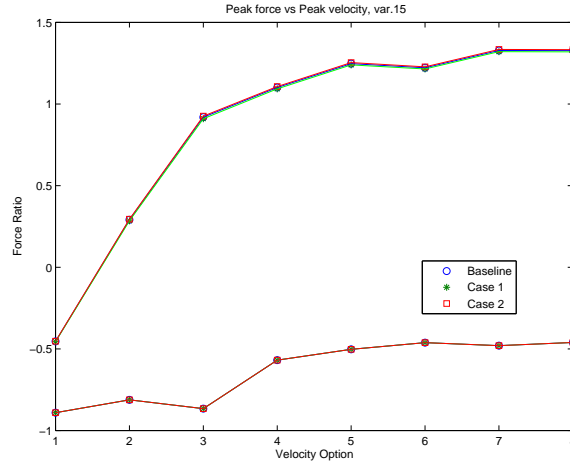


Figure 6.22: Peak force results for the model sensitivity to  $K_4$ .

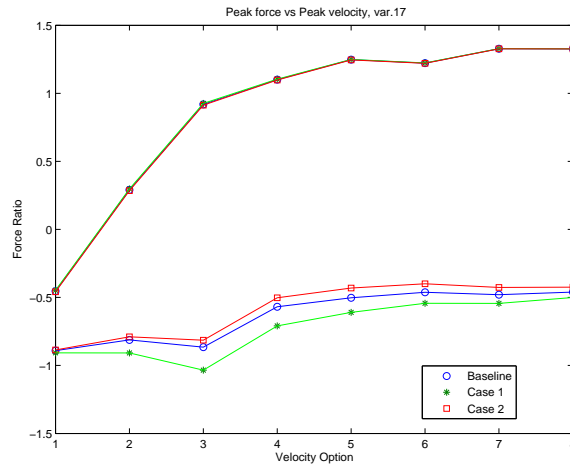


Figure 6.23: Peak force results for the model sensitivity to  $A_{31}$ .

## 6.5 Sensitivity Low Speed Compression Results

Figure 6.3 shows the sensitivity results ranked from largest effect to smallest. The top ten parameters are given in Table 6.4. The parameters in this table with a sensitivity greater than 10% were analyzed to show the model results and look at the equations to explain the model dependence on the parameter. The results were shown for the remaining parameters.

Table 6.4: Top ten parameters for low speed compression sensitivity.

Rank	Parameter	Sensitivity (%)
1	$A_r$	81.3
2	$A_p$	50.0
3	$A_{31}$	19.7
4	$\rho$	19.1
5	$K_1$	13.4
6	$A_{11}$	6.3
7	$F_r$	6.0
8	$K_3$	1.9
9	$C_{d11}$	1.6
10	$C_{d12}$	1.2

### 6.5.1 Repeated Parameters With Significant Effects

Many of the parameters for high speed extension overlap with the variables in the low speed extension case.  $A_r$  has the largest effect on high speed extension and the effect is covered in Section 6.3.2.  $A_p$  has the second largest effect on high speed extension and the effect is covered in Section 6.3.1.  $\rho$  has the fourth largest effect on high speed extension and the effect is covered in Section 6.3.4.

### 6.5.2 Fixed Valve Bleed Orifice Area Sensitivity

$A_{31}$ , the fixed valve bleed orifice area has the third largest effect of the parameters on low speed compression. The resulting force vs. velocity plots for velocity options 3 and 8 are given in Figure 6.24. The peak force vs. peak velocity plot in Figure 6.25 shows that increasing  $A_{31}$  has almost no effect on the peak damper force in extension and decreases the peak force magnitude in compression. The most relevant equation for  $A_{31}$  is the fixed valve bleed orifice equation, which is given as,

$$q_{31} = C_{d31} A_{31} n_{31} \text{sgn}(P_2 - P_3) \sqrt{\frac{2|P_2 - P_3|}{\rho}}. \quad (6.14)$$

The main effect of the fixed valve bleed orifice area is on the flow caused by a given pressure differential. An increase in  $A_{31}$ , increases the flow caused by a given pressure differential. This will cause the force magnitude to not change in extension and lower in compression (less negative), as shown in the Figure 6.24. The effect of  $A_{31}$  makes sense practically since an increase in the fixed valve bleed orifice area increases the flow to the reserve chamber from the rebound chamber for a given pressure differential. The pressure in the reserve chamber does not change much due to the volume of gas that compresses significantly more than the fluid. This helps limit the pressure in the compression chamber, which causes a lower

pressure differential between the rebound and compression chambers. The lower pressure differential the rebound and compression chambers leads to lower forces based on the piston rod equation. The pressure differentials are lower at lower speeds, so the shim valves do not open much. This makes the bleed orifice most important at low speeds, which is why  $A_{31}$  has a larger effect than  $K_1$  and  $K_3$  for low speed compression.

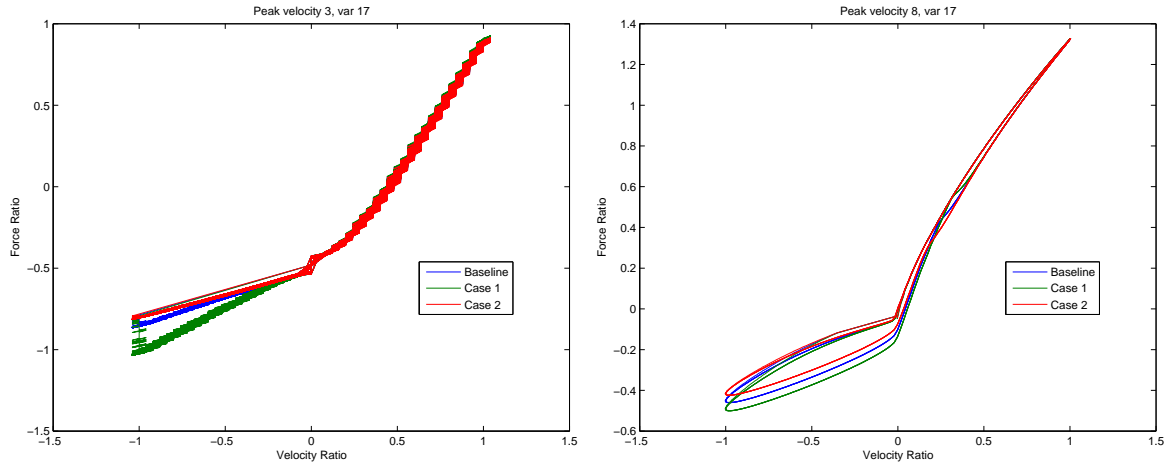


Figure 6.24: Force vs. velocity results for the model sensitivity to  $A_{31}$ .

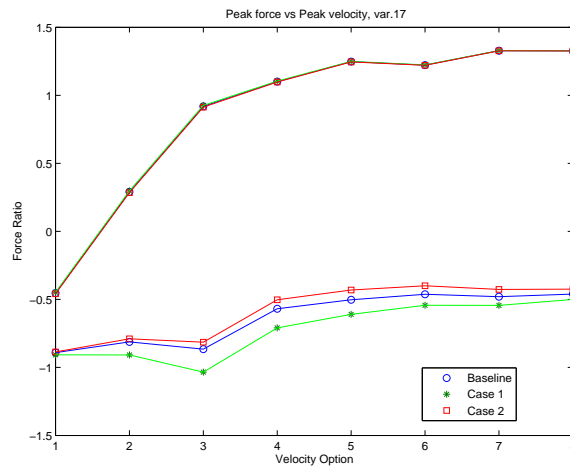


Figure 6.25: Peak force results for the model sensitivity to  $A_{31}$ .

### 6.5.3 Shim Stiffness for Flow $q_{12}$ Sensitivity

$K_1$ , the shim stiffness for flow  $q_{12}$ , has the fifth largest effect of the parameters on low speed extension. The resulting force vs. velocity plots for velocity options 3 and 8 are given in

Figure 6.26. The peak force vs. peak velocity plot in Figure 6.27 shows that increasing  $K_1$  has almost no effect on the peak damper force in extension and increases the peak force magnitude in compression. The most relevant equation for  $K_1$  is the piston check valve equation for flow  $q_{12}$ , which is written as,

$$q_{12} = 0 \quad P_1 \geq P_2 \quad (6.15)$$

$$q_{12} = C_{d12} \pi D_{v12} \frac{|P_1 - P_2| A_{f12} n_{12}}{K_1} \sqrt{\frac{2 |P_1 - P_2|}{\rho}} \quad P_1 < P_2, \quad (6.16)$$

where  $C_{d12}$  is the discharge coefficient for flow  $q_{12}$ ,  $D_{v12}$  is the diameter of the orifices for flow  $q_{12}$  about the centerline of the damper,  $A_{f12}$  is the flow area of a single orifice for flow  $q_{12}$ ,  $n_{12}$  is the number of individual orifices for flow  $q_{12}$ ,  $K_1$  is the shim stiffness of the shim stack for flow  $q_{12}$  measured at a radius of  $D_{v12}/2$ . The main effect of  $K_1$  is on the flow caused by a given pressure differential. An increase in  $K_1$ , decreases the flow caused by a given pressure differential. This will cause the force magnitude to not change in extension and be larger in compression (more negative), as shown in the Figure 6.26. The effect of  $K_1$  makes sense practically because an increase in the piston compression flow valve stiffness increases the pressure differential needed to cause the flow required to create an equilibrium between the rebound and compression chambers in compression. The higher pressure differentials lead to higher forces based on the piston rod equation. The pressure differentials are higher at higher speeds, so the shim valves open larger than the bleed valve flow areas. This makes the bleed orifice less important at high speeds, which is why  $K_1$  has a larger effect than  $A_{31}$  for high speed compression.

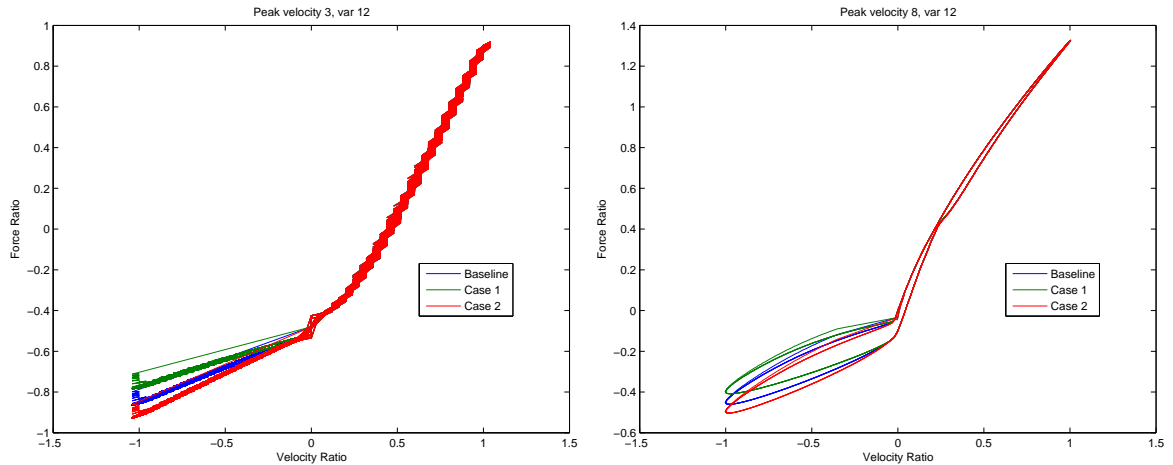


Figure 6.26: Force vs. velocity results for the model sensitivity to  $K_1$ .

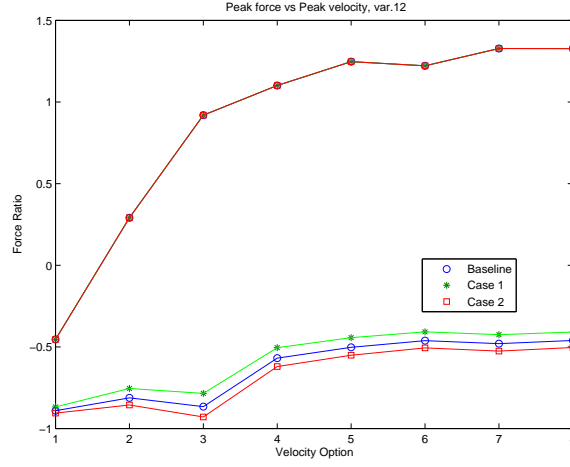


Figure 6.27: Peak force results for the model sensitivity to  $K_1$ .

#### 6.5.4 Other Parameters

$A_{11}$  has the sixth largest effect on low speed compression and the effect is covered in Section 6.3.3.  $F_r$  has the seventh largest effect on low speed compression and the effect is covered in Section 6.3.6.  $K_3$  has the eighth largest effect on low speed compression and the effect is shown in Figure 6.28.  $C_{d11}$  has the ninth largest effect on low speed compression and the effect is covered in Section 6.3.7.  $C_{d12}$  has the tenth largest effect on low speed compression and the effect is shown in Figure 6.19.

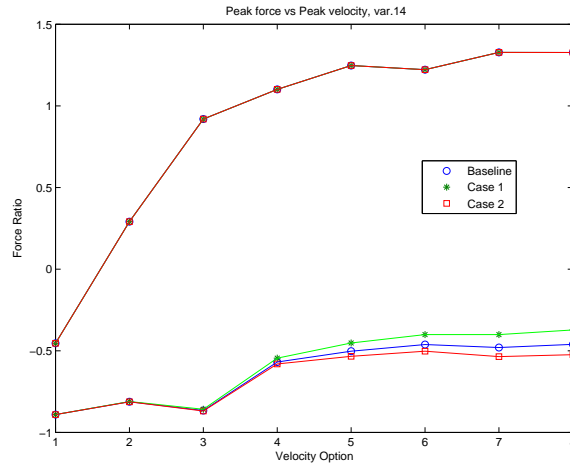


Figure 6.28: Peak force results for the model sensitivity to  $K_3$ .

## 6.6 Sensitivity High Speed Compression Results

Figure 6.4 shows the sensitivity results ranked from largest effect to smallest. The top ten parameters are given in Table 6.5. The parameters in this table with a sensitivity greater than 10% were analyzed to show the model results and look at the equations to explain the model dependence on the parameter. The results were shown for the remaining parameters.

Table 6.5: Top ten parameters for high speed compression sensitivity.

Rank	Parameter	Sensitivity (%)
1	$A_r$	107.7
2	$A_p$	61.7
3	$\rho$	38.3
4	$A_{31}$	26.9
5	$K_3$	24.8
6	$K_1$	21.1
7	$C_{d12}$	3.7
8	$B_{31}$	3.3
9	$C_{d11}$	2.2
10	$A_{11}$	1.9

### 6.6.1 Repeated Parameters With Significant Effects

Many of the parameters for high speed extension overlap with the variables in the low speed extension case.  $A_r$  has the largest effect on high speed extension and the effect is covered in Section 6.3.2.  $A_p$  has the second largest effect on high speed compression and the effect is covered in Section 6.3.1.  $\rho$  has the third largest effect on high speed compression and the effect is covered in Section 6.3.4.  $A_{31}$  has the fourth largest effect on high speed compression and the effect is covered in Section 6.5.2.  $K_1$  has the sixth largest effect on high speed compression and the effect is covered in Section 6.5.3.

### 6.6.2 Shim Stiffness for Flow q32 Sensitivity

$K_3$ , the shim stiffness for flow  $q_{32}$  has the fifth largest effect of the parameters on low speed compression. The resulting force vs. velocity plots for velocity options 3 and 8 are given in Figure 6.29. The peak force vs. peak velocity plot in Figure 6.30 shows that increasing  $K_3$  has almost no effect on the force magnitude in extension and increases the force magnitude in compression. The most relevant equation for  $K_3$  is the piston check valve equation for

flow  $q_{32}$ , which is defined as,

$$q_{32} = 0 \quad P_2 \leq P_3 \quad (6.17)$$

$$q_{32} = C_{d32} \pi D_{v32} \frac{|P_2 - P_3| A_{f32} n_{32}}{K_3} \sqrt{\frac{2 |P_2 - P_3|}{\rho}} \quad P_2 > P_3, \quad (6.18)$$

where  $C_{d32}$  is the discharge coefficient for flow  $q_{32}$ ,  $D_{v32}$  is the diameter of the orifices for flow  $q_{32}$  about the centerline of the damper,  $A_{f32}$  is the flow area of a single orifice for flow  $q_{32}$ ,  $n_{32}$  is the number of individual orifices for flow  $q_{32}$ ,  $K_3$  is the shim stiffness of the shim stack for flow  $q_{32}$  measured at a radius of  $D_{v32}/2$ . The main effect of  $K_3$  is on the flow caused by a given pressure differential. An increase in  $K_3$ , decreases the flow caused by a given pressure differential. This will cause the force magnitude to not change in extension and be larger in compression (more negative), as shown in the Figure 6.29. The effect of  $K_3$  makes sense practically because an increase in the fixed valve compression flow stiffness decreases the flow to chamber 3 from chamber 2 for a given pressure differential, which increases  $P_2$ . The increased  $P_2$  creates higher pressure differentials between chambers 1 and 2, which leads to higher forces based on the piston rod equation. The pressure differentials are higher at higher speeds, so the shim valves open larger than the bleed valve flow areas. This makes the bleed orifice less important at high speeds, which is why  $K_3$  has a larger effect than  $A_{31}$  for high speed compression.

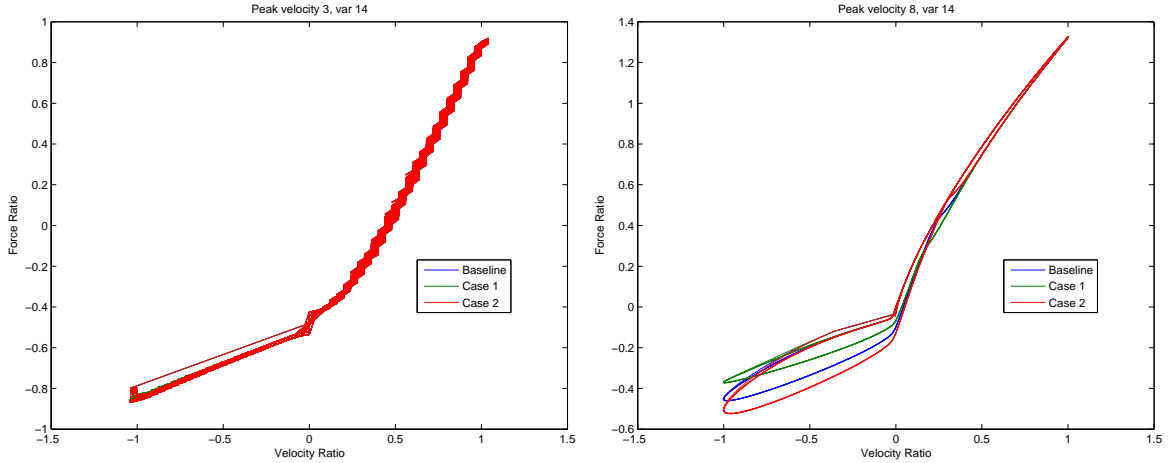


Figure 6.29: Force vs. velocity results for the model sensitivity to  $K_3$ .

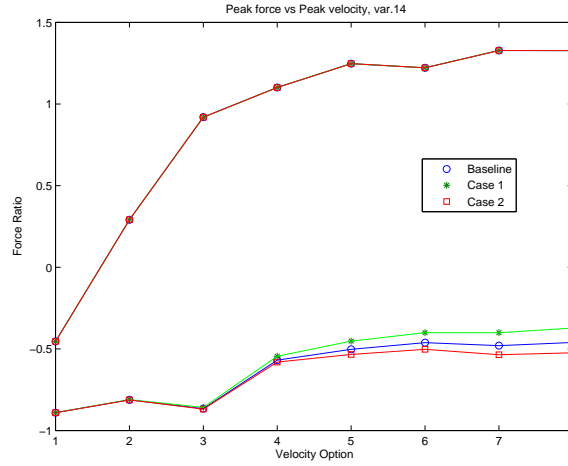


Figure 6.30: Peak force results for the model sensitivity to  $K_3$ .

### 6.6.3 Other Parameters

$C_{d12}$  has the seventh largest effect on high speed compression and the effect is shown in Figure 6.19.  $\beta_{31}$  has the eighth largest effect on low speed compression and the effect is shown in Figure 6.20.  $C_{d11}$  has the ninth largest effect on low speed compression and the effect is covered in Section 6.3.7.  $A_{11}$  has the tenth largest effect on low speed compression and the effect is covered in Section 6.3.3.

## 6.7 Sensitivity Study Conclusions

The sensitivity study shows that the four sections of the damper response have different effects. These results show that the damper can be tuned to desired settings for each section of the response. The parameters with a sensitivity of 10% or larger were analyzed to determine how to vary them physically from a current design and if that is feasible. There are 6 main types of parameters: bleed orifices, shim stiffnesses, damper container dimensions, friction, fluid density, and bleed orifice discharge coefficient. The damper container dimensions are the piston area,  $A_p$ , and damper rod area,  $A_r$ . They can be varied by building new parts, which may cause issues with the current piston or shims, which would also need to be replaced. These parameters require the most work to change. The bleed orifice discharge coefficient might be varied if the shape of the bleed orifice is changed. However, testing would be needed to check if the discharge coefficient was varied to the correct value, making this a difficult parameter to physically vary. Friction could be varied by changing the materials or contact area at the seal between the piston and the damper tube and between the damper rod and damper body. However changing either the materials or contact area could prevent proper sealing in the damper, so changing the friction is not an ideal option.

The fluid density can be changed by emptying the fluid from the damper and replacing



it with a hydraulic fluid with a lower density. The main issue with this is that the bulk modulus of the fluid could change with the different fluid, but the bulk modulus has less of an effect than the fluid density. The bleed orifice areas can be increased by machining the orifice areas in the current parts to be larger and they can be decreased by creating new parts with smaller areas. Increasing the area would be easier since it would involve modifying existing parts, while decreasing would require new parts to be made. The new parts could be created from the designs of the initial parts. The shim stiffnesses can be varied by adjusting the shims in the shim stacks. The damper will need to be taken apart to replace the shims and new shims will be needed. The shims are just flat pieces of metal so many options could be cheaply obtained and tested. The only issue with this setup is that the shim stiffness experiments are time intensive. So likely the options could be placed in a damper and run, then the best couple of options could be tested to determine the shim stiffnesses.

## Chapter 7: Conclusions

A lumped parameter model of twin tube automotive dampers was created in this study. The model was based on four main physical concepts: Newton's second law, conservation of flow, orifice flow and fluid compressibility. The equations for each of these concepts were derived in Chapter 2. The equations were then solved for the 18 unknowns in the system and converted to dimensionless form. The equations were then created in Simulink to create the full model. The model was then compared to experimental results in Chapter 5. The comparison showed that the model successfully achieved correlation over a large range of frequencies, two orders of magnitude. The model was valid for a low frequency range, from 0 to 10 Hz.

A sensitivity analysis was performed on the damper model for the 20 most important variables. The results of the study were organized based on 4 sections of the peak force vs. peak velocity curve in Sections 6.2-6.6. From these results, a method for designing or redesigning a damper was determined. The most effective parameters were ranked based on both the effect of the parameter and the resources required change each component. Based on these criteria, the four most efficient types of parameters are, in order: shim stiffnesses, fluid density, bleed orifices, and damper container dimensions. The shim stiffnesses and fluid density can be varied by simply replacing an internal part of the damper, shims and fluid, respectively. Both options require new parts and not adjustments to current parts. Varying the bleed orifices and damper container dimensions require more complex parts that need to be changed or completely rebuilt. These parameters can be varied to create a desired damper response.

# Bibliography

- [1] Warren C. Young and Richard G. Budynas. *Roark's Formulas for Stress and Strain*. McGraw-Hill, 7th edition, 2002.
- [2] Harold Harvey Lang. *A Study of the Characteristics of Automotive Hydraulic Dampers at High Stroking Frequencies*. PhD thesis, University of Michigan, 1977.
- [3] L. Segel and H. H. Lang. The Mechanics of Automotive Hydraulic Dampers at High Stroking Frequencies. *Vehicle System Dynamics*, 10, Issue 2:82–85, 1981.
- [4] Stefaan W. Duym, Randy Stiens, Gino V. Baron, and Koenraad G. Reybrouck. Physical Modleling of the Hysteretic Behaviour of Automotive Shock Absorbers. *SAE TECHNICAL PAPER SERIES*, 970101, 1997.
- [5] Stefaan W.R. Duym. Simulation Tools, Modelling and Identification, for an Automotive Shock Absorber in the Context of Vehicle Dynamics. *Vehicle System Dynamics*, 33:261285, 2000.
- [6] Michael S. Talbott. An experimentally validated physical model of a high-performance automotive monotube damper. Master's thesis, Purdue University, 2002.
- [7] Michael S. Talbott and John Starkey. An Experimentally Validated Physical Model of a High-Performance Mono-Tube Damper. *SAE TECHNICAL PAPER SERIES*, 2002-01-3337, 2002.
- [8] Kirk Shawn Rhoades. Development and Experimental Verification of a parametric model of an automotive damper. Master's thesis, Texas A&M University, 2006.
- [9] Kwangjin Lee. Numerical Modelling for the Hydraulic Performance Prediction of Automotive Monotube Dampers. *Vehicle System Dynamics*, 28:25–39, 1997.
- [10] R. Mollica and K. Youcef-Toumi. A Nonlinear Dynamic Model of a Monotube Shock Absorber. *Proceedings of the American Control Conference*, pages 704–708, 1997.
- [11] M. Alonso and Á. Comas. Modelling a twin tube cavitating shock absorber. *Proceedings Institution of Mechanical Engineers*, 220:1031–1040, 2006.
- [12] Yanqing Liu and Jianwu Zhang. Nonlinear dynamic responses of twin-tube hydraulic shock absorber. *Mechanics Research Communications*, 29:359365, 2009.
- [13] C. Surace, K. Worden, and G. R. Tomlinson. An Improved Nonlinear Model for an Automotive Shock Absorber. *Nonlinear Dynamics*, 3:413–429, 1992.
- [14] Koenraad Reybrouck. A Non Linear Parametric Model of an Automotive Shock Absorber. *SAE TECHNICAL PAPER SERIES*, 940869, 1994.

- [15] F. Herr, T. Mallin, J. Lane, and S. Roth. A Shock Absorber Model Using CFD Analysis and Easy5. *SAE TECHNICAL PAPER SERIES*, 1999-01-1322, 1999.
- [16] M. Shams, R. Ebrahimi, A. Raoufi, and B. J. Jafari. CFD-FEA Analysis of Hydraulic Shock Absorber Valve Behavior. *International Journal of Automotive Technology*, 8, No. 5:615–622, 2007.
- [17] Linda Tweedy Till and Glenn Wendel. Application of computational fluid dynamics analysis in improving valve design. *SAE TECHNICAL PAPER SERIES*, 2002-01-1397, 2002.
- [18] Jinghong Yu, Zhaoneng Chen, and Yuanzhang Lu. The Variation of Oil Effective Bulk Modulus With Pressure in Hydraulic Systems. *Transactions of the ASME*, 116:146–150, 1994.
- [19] Choon-Tae Lee and Byung-Young Moon. Simulation and experimental validation of vehicle dynamic characteristics for displacement-sensitive shock absorber using fluid-flow modelling. *Mechanical Systems and Signal Processing*, 20:373388, 2006.
- [20] E.O. Doebelin. *System Dynamics: Modeling, Analysis, Simulation, Design*. CRC, 1998.